# Numerical simulations of the space-time structure in the Lorentzian type IIB matrix model

**Toshihiro AOKI**[1]

*Department of Particle and Nuclear Physics, School of High Energy Accelerator Science, The Graduate University for Advanced Studies, SOKENDAI*

December 10, 2019

[1]E-mail address : toshaoki@post.kek.jp

# Abstract

The type IIB matrix model was proposed as a non-perturbative formulation of superstring theory in 1997. Monte Carlo simulation of its Lorentzian version showed that not only space but also time dynamically emerge. Furthermore, it suggested that a (3+1)D expanding space-time start to expand at some critical time. This numerical result implies that the expanding (3+1)D space-time naturally appears from (9+1)D space-time, where superstring theory is defined. The expanding behavior was examined carefully by simulating simplified versions of the model, which showed that the expansion is exponential at the beginning, and it turns into a power law at later times. This intriguing property is reminiscent of the inflation and the FRW universe, respectively.

In our work, we investigated the space-time structure of the matrix configurations generated by the Monte Carlo simulation, where we found that the expanding 3D space is described substantially by the Pauli matrices. We have attributed this problem to an approximation used to avoid the sign problem in this simulation. In order to overcome the sign problem instead of using the approximation, we have been exploiting the Complex Langevin simulation, which was invented to make simulations of models with complex action feasible. Here we have been mainly investigating a more uncomplicated, (5+1)D bosonic model in its Lorentzian version to avoid time-consuming. Our results show a transition from the Pauli-matrix structure to a smooth space-time structure.

# Acknowledgements

The author would like to thank his adviser J. Nishimura for continuing support and encouragement, M. Hirasawa, Y. Ito for valuable discussions at the KEK Theory Center. As for the research based on Monte Carlo simulation, the author would like to thank his collaborators, M. Hirasawa, Y. Ito, J. Nishimura and A. Tsuchiya. As for the research based on Complex Langevin simulation, the author would like to thank his collaborators, K. N. Anagnostopoulos, T. Azuma, M. Hirasawa, Y. Ito, J. Nishimura, S. K. Papadoudis and A. Tsuchiya.

These researches used computational resources of the K computer of the HPCI system provided by the AICS through the HPCI System Research Project "Quest for the ultimate laws and the birth of the universe" (Project ID: hp170229, hp180178). Computation was also carried out on PC clusters, KEKCC at KEK. The supercomputer FX10 at University of Tokyo was used in developing our Monte Carlo code for parallel computing. The research based on Complex Langevin simulations was also supported by computational time granted by the Greek Research & Technology Network (GRNET) in the National HPC facility - ARIS - under project ID LIKKT and IIB10D.

# Contents

# Chapter 1

# Introduction

Anticipation that the superstring theory is a fundamental theory has motivated intense researches into exploring how the inflation emerges naturally from the string theory, but there are significant obstacles to deriving the inflation from the string theory.

The superstring theories require 9 dimensions of space and 1 dimension of time, although we only experience 3 spatial dimensions and 1 temporal dimension in our universe. So far, it has been believed that extra 6 dimensions are compactified to a very small size. There are, however, many ways to compactify the (9+1)D superstring theories into the (3+1)D theories as far as perturbative string theories are concerned, and thus we suffer from the infinite vacua. It means that the superstring theory has no ability to predict our (3+1)D universe, and we cannot tell whether the superstring theory dynamically generates the inflation. It is, therefore, required to respect the superstring theory non-perturbatively.

In 1997, N. Ishibashi, H. Kawai, Y. Kitazawa and A. Tsuchiya presented the type IIB matrix model as a non-perturbative formulation of superstring theory, which is called Ishibashi-Kawai-Kitazawa-Tsuchiya(IKKT) model [1]. It is defined by the following action:

$$S = S_{\mathrm{b}} + S_{\mathrm{f}}\,, \tag{1.1}$$

$$S_{\mathrm{b}} = -\frac{1}{4g^2}\,\mathrm{Tr}\left(\left[A_\mu, A_v\right]\left[A^\mu, A^v\right]\right)\,, \tag{1.2}$$

$$S_{\mathrm{f}} = -\frac{1}{2g^2}\,\mathrm{Tr}\left(\Psi_\alpha\left(\mathcal{C}\Gamma^\mu\right)_{\alpha\beta}\left[A_\mu, \Psi_\beta\right]\right)\,, \tag{1.3}$$

where $A_\mu(\mu = 0, 1, \ldots, 9)$ and $\Psi_\alpha(\alpha = 1, \ldots, 16)$ are bosonic and fermionic $N \times N$ traceless Hermitian matrices. This model is derived by dimensionally reducing 10D

$\mathcal{N} = 1$ super Yang-Mills action to zero dimension. It is a simple model of matrices in zero dimension. We can also obtain this model from the matrix regularization of the Green-Schwarz action of the type IIB superstring theory in the Schild gauge, which tells us that correspondence between the IKKT matrix model and the type IIB superstring theory exists. There is also prominent evidence that the Schwinger-Dyson equation for a Wilson loop produces light-cone string field theory for the type IIB superstring, which means that the model can reproduce the perturbation theory of the type IIB superstring theory [2].

There are some essential features of the model to be stressed. The type IIB matrix model has no free parameters. Moreover, space-time does not exist a priori, and it is expected to emerge dynamically from the eigenvalue distribution of the 10 bosonic matrices $A_\mu$ ($\mu = 0, \dots, 9$). This model, therefore, has the potential to clarify a possible non-perturbative mechanism for dynamical compactification in superstring theory.

For a long time, it had been typical to address the issue of how we can predict the space-time dimensionality in the Euclidean type IIB matrix model, where we replace the Hermitian matrix $A_0$ in the temporal direction by a "Wick rotation", $A_0 = iA_{10}$. The Euclidean model obtained in this way has manifest SO(10) symmetry and has a positive semi-definite action for the bosonic part. Its partition function was proven to be finite for arbitrary matrix size [3].

Monte Carlo studies of the Euclidean model is, however, difficult due to the sign problem because the Pfaffian that appears from integrating out the fermionic matrices is complex in general. For this reason, the Gaussian expansion method was proposed as an alternative approach to this issue [4]. Ref. [5] showed that SO(10) rotational symmetry of the model is broken down to SO(3), which may be interpreted that the emergent space-time in the Euclidean type IIB matrix model does not seem to be 4D space-time. While this result reveals the exciting property of the Euclidean model, the connection to our real space-time is unclear. In the first place, while quantum field theory in flat space-time commonly uses such Euclidean space-time, it is known to be subtle, whether it can be used in quantum gravity.

To tackle this issue, S.-W. Kim, J. Nishimura, and A. Tsuchiya studied the type IIB matrix model without making the Wick rotation [6]. This model is called the "Lorentzian" type IIB matrix model based on the partition function

$$Z = \int dA d\Psi e^{iS} = \int dA e^{iS_b} \operatorname{Pf} \mathcal{M}(A) \,, \tag{1.4}$$

where the Pfaffian $\mathrm{Pf}\,\mathcal{M}(A)$ that appears from integrating out fermionic matrices $\Psi_\alpha$. The "$i$" in front of the action is motivated from the fact that we use inverse Wick rotation on the worldsheet as well as on the target space to derive the Lorentzian model from the Euclidean model . The action has SO(9,1) symmetry instead of SO(10). Compared to the Euclidean type IIB matrix model, in Minkowski signature, there is a difference between space and time, and thus its Lorentzian model is more suitable for studying the real-time dynamics. The Lorentzian type IIB matrix model is, however, not well-defined as it is. Unlike the Euclidean version, the bosonic action $S_\mathrm{b}$ is indefinite. Thus it seems at first sight that the model is unstable. Note also that, unlike the Euclidean model, the matrix integral is divergent because $e^{iS_\mathrm{b}}$ is a pure phase factor in the integrand of the partition function, and the Pfaffian is a polynomial in $A_\mu$. One, therefore, has to put two "infrared" cutoffs for the spatial and temporal directions, respectively, to make the partition function finite.

Moreover, another critical problem in the model to emphasize is that $e^{iS_\mathrm{b}}$ is a pure phase, therefore its Monte Carlo simulation is faced with a sign problem. To make the Lorentzian matrix model accessible by Monte Carlo simulation, one can integrate out the scale factor of the bosonic matrices $A_\mu$ first and using an approximation, which essentially converts the phase factor $e^{iS_\mathrm{b}}$ into a constraint $S_\mathrm{b} \simeq 0$. On the other hand, the Pfaffian is real, unlike in the Euclidean case [7], as the simulation confirmed. It follows from what has been said thus far that the model one obtains in this way does not have the sign problem.

Along this line of thinking, the authors performed the Monte Carlo simulation of the Lorentzian type IIB matrix model for the first time. They achieved intriguing results, where the matrix configurations generated by simulating the Lorentzian model have a non-trivial structure. By making the SU($N$) transformation that diagonalizes the temporal matrix $A_0$, the 9D spatial matrices represented by $A_i\,(i = 1, \ldots, 9)$ have a band-diagonal structure, which enabled the extraction of the real-time evolution. In this way, it turned out that only 3 out of 9 directions start to expand at some critical time (See Figure 1.1), which implies that the rotational SO(9) symmetry in the spatial directions is spontaneously broken down to SO(3) at the critical time. In other words, the model may predict the emergence of a (3+1)D expanding space-time from superstring theory in (9+1)D.

To see what happens at later times in this model, one needs to increase the matrix size, however, which makes the Monte Carlo simulation much more time-consuming. Therefore, since then, the expanding behavior of the eigenvalue distribution had been studied in

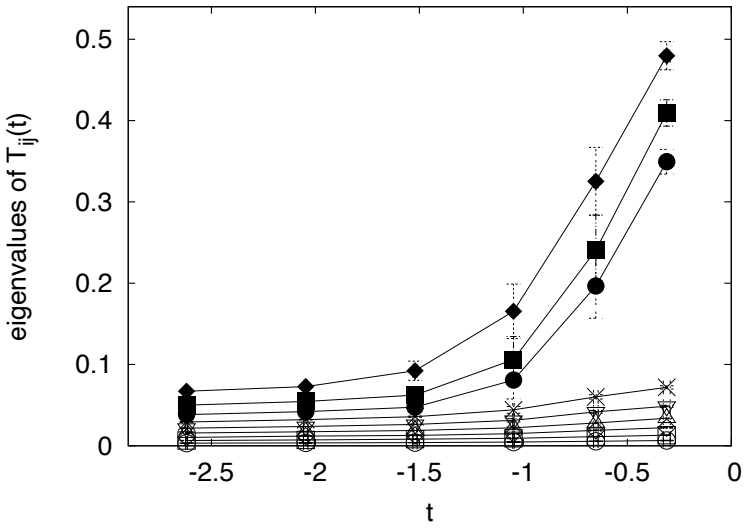


**Figure 1.1:** After a critical time, it is suggested SO(9) symmetry is spontaneously broken down to SO(3) [6].

various simplified versions of this model. One simplified model of them describes the early time behaviors of the original model [8] with smaller than or equal to $N = 64$. It was observed that an apparent exponentially expanding behavior, which is reminiscent of the inflation. Monte Carlo studies of the original model with $N = 24$ yielded results consistent with this observation although the matrix size used was not large enough to confirm the long-time behavior [9].

In [10], the authors studied a bosonic model, which can be obtained by merely omitting the fermionic matrices. This simplification and the usage of a large-scale parallel computer enable us to perform Monte Carlo simulation with the matrix size up to $N = 512$. In this large-scale computation, the large-N scaling behavior is clearly observed. The expanding behavior of the spatial extent can be fitted by an exponential function $e^{\Lambda t}$ with respect to time $t$ only for a rather short period, and after that, it becomes a power-law $t^{1/2}$. The latter behavior coincides with the expanding behavior of the Friedmann-Robertson-Walker universe in the radiation dominated era (See Figure 1.2). The obtained results suggest a scenario for the full model that its expansion is exponential at early times, and turns into a power law at later times.

In our work [11], we investigated the space-time structure of the matrix configurations generated by Monte Carlo simulation of the Lorentzian type IIB matrix model and the simplified models. In particular, we calculated the eigenvalues of the submatrices of the spatial matrices $A_i$ corresponding to each time slice and found that only two eigenvalues

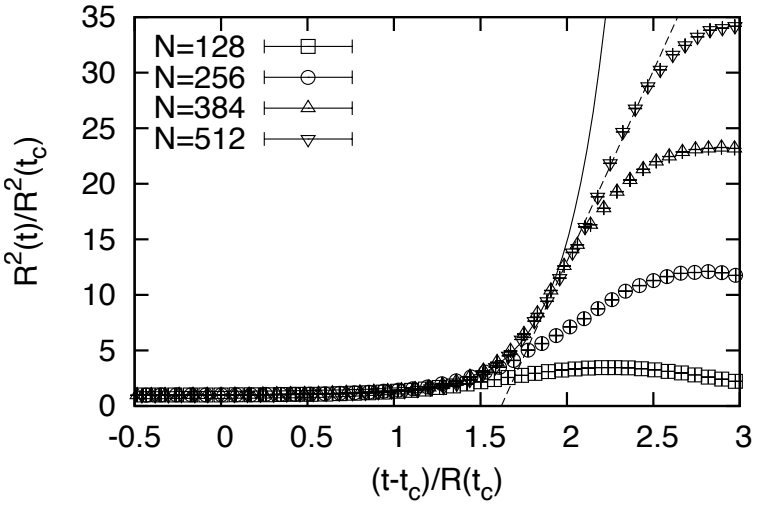


**Figure 1.2:** The exponential expansion analogous to the inflation occurs at early times, and then the expansion behavior changes into a power-law analogous to that of the Friedmann-Robertson-Walker universe in the radiation dominated era [10].

grow in magnitude after the critical time (See Figure 1.3). A more detailed analysis showed that the expanding 3D space is described essentially by the Pauli matrices. Namely, the space is actually more like a fuzzy sphere, although it has been called "3D" in the sense that it has three extended directions. While we keep on using the word 3D in this sense, we refer to the space with the Pauli-matrix structure as a "singular 3D space" for the explanation of our observation. We also observed that the situation remains unaltered even at late times or in the continuum limit for the simplified models, and it is shared by the original model with maximal supersymmetry as well, and even in the presence of the fermionic matrices. These results raise the most pressing problem: whether this model can generate a 3D space with continuum geometry, which we refer to as a "regular 3D space".

At the heart of this problem is the phase factor $e^{iS_{\mathrm{b}}}$ in the partition function. As previously mentioned, Monte Carlo simulation of the Lorentzian type IIB matrix model is not straightforward due to it. The importance sampling is not applicable as it is, and one has to face the sign problem if one uses reweighting for this factor. In this work, as well as in the previous studies, this problem had been avoided by integrating out the scale factor of the bosonic matrices $A_\mu$ first and using an approximation. Here we have pointed out a subtlety in this approximation, and have argued that it actually amounts to replacing the phase factor $e^{iS_{\mathrm{b}}}$ by a positive weight $e^{cS_{\mathrm{b}}}(c > 0)$. This new interpretation of the simulations naturally explains not only the emergence of the band-diagonal structure in

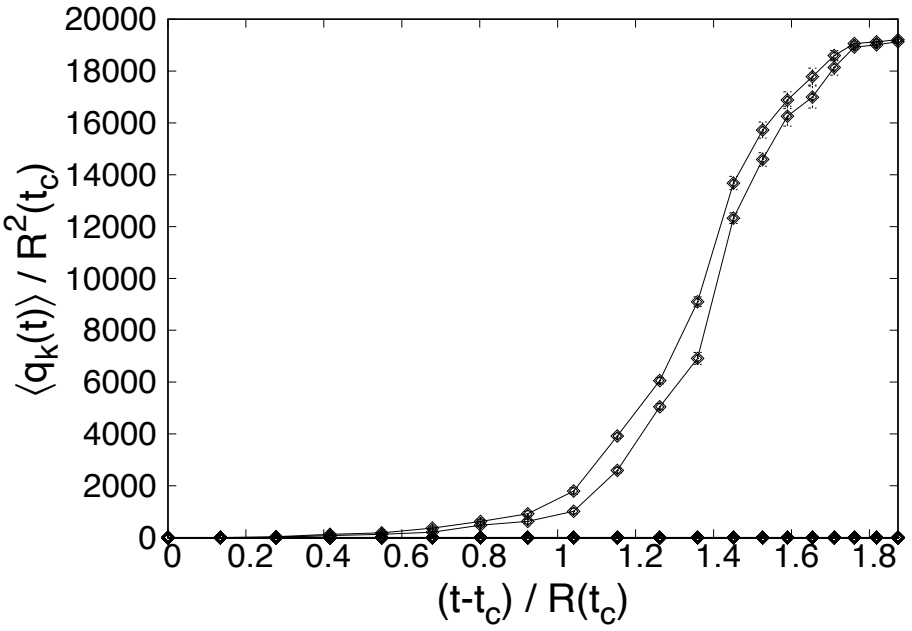


**Figure 1.3:** Space-time structure of the matrix configurations generated by Monte Carlo simulation of the simplified models. We have found that it's essentially the Pauli-matrix structure.

the spatial matrices $A_i$, which is crucial in extracting the real-time evolution but also the (3+1)D expanding behavior with the Pauli-matrix structure.

To overcome this issue, we have been performing the Complex Langevin method, which was invented to make simulations of models with complex action feasible. In recent years there has been major progress in evading the sign problem. Among others, it does not entail longer computation times, which enables its application to much larger system size. Preliminarily results of this simulation open the door to the possibility of obtaining a regular space-time [12].

It is hostile to directly handle the phase factor $e^{iS_{\rm b}}$. In this simulation, therefore, it is useful to introduce two deformation parameters $(s, k)$ in the action, which correspond to the Wick rotations on the worldsheet and in the target space, respectively.More specifically, firstly, we introduce $\tilde{S} = -iS_{\rm b}$ so that the partition function (1.4) is rewritten as

$$Z = \int dA \ \mathrm{Pf}\mathcal{M}(A) \ e^{-\tilde{S}} \, . \tag{1.5}$$

Secondly, we introduce $s$ $(-1 \leq s \leq 1)$ corresponding to the Wick rotation on the worldsheet as

$$S_{\mathrm{b}} \mapsto \mathrm{e}^{is\pi/2} S_{\mathrm{b}} \ . \tag{1.6}$$

Lastly, $k$ $(0 \leq k \leq 1)$ corresponding to the Wick rotation in the target space can be introduced by the replacement

$$A_0 \mapsto \mathrm{e}^{-ik\pi/2} A_0 \ . \tag{1.7}$$

The action becomes

$$\tilde{S} = -iN\beta \mathrm{e}^{is\pi/2} \left\{ -\frac{1}{2} \mathrm{e}^{-ik\pi} \operatorname{Tr} \left(F_{0i}\right)^2 + \frac{1}{4} \operatorname{Tr} \left(F_{ij}\right)^2 \right\} \ , \tag{1.8}$$

and the $\mathrm{Pf}\mathcal{M}\left(A\right)$ in should be replaced by $\mathrm{Pf}\,\mathcal{M}\left(\mathrm{e}^{-ik\pi/2} A_0, A_i\right)$. The Lorentzian model is retrieved at $(s,k) = (0,0)$, whereas the Euclidean model can be obtained at $(s,k) = (1,1)$. Thus, these parameters enable us to interpolate between the Lorentzian version $(s,k) = (0,0)$ and the Euclidean version $(s,k) = (1,1)$.

Note that the Lorentzian type IIB matrix model needs to be regularized in some way or another because the phase factor $e^{iS_{\mathrm{b}}}$ in the partition function cannot suppress the contribution from the bosonic matrices with arbitrary large elements as discussed above. Here we improve the treatment of infrared cutoffs on both the spatial and temporal matrices. This improvement enables us to investigate a much larger range of deformation parameters, and then approach our target, namely the original model.

First, we focus on $(s,k) = (-1,0)$ in the deformation parameter space, where we do not have the sign problem. This case corresponds to the approximate model investigated in our Monte Carlo studies. In fact, we here observe the emergence of (3+1)D expanding space-time with the Pauli-matrix structure (See Figure 1.4(Left)). Then we tune the worldsheet deformation parameter $s$ and the target space deformation parameter $k$ to the region for the Lorentzian model $(s,k) = (0,0)$. There, we find it possible to obtain a smoother space-time structure(See Figure 1.4(Right)). We have been considering that the two deformation parameters $s$ and $k$ should be tuned eventually to $(s,k) = (0,0)$ in the large-$N$ limit. Whether a smooth space-time picture appears in that limit at sufficiently late time is an important open question, which can be answered along the line of this research.

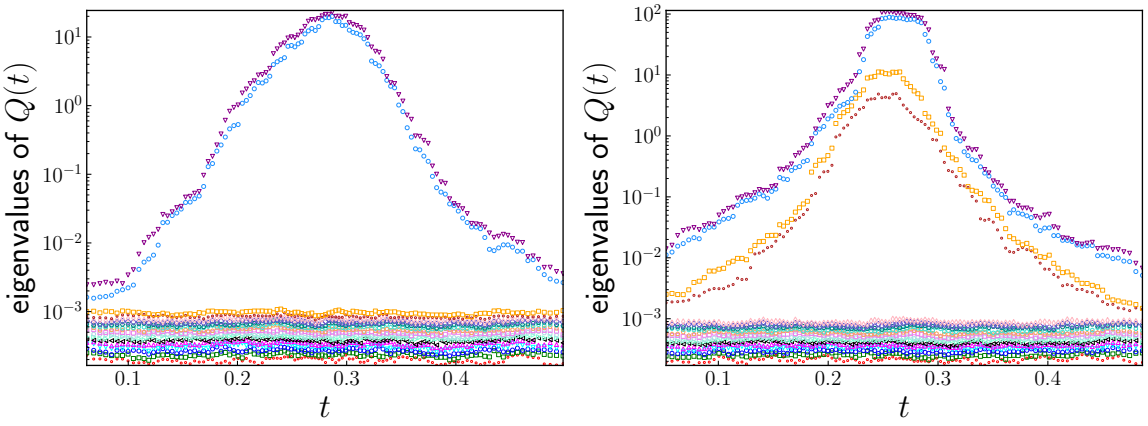


**Figure 1.4:** (Left) The Pauli-matrix structure in the Complex Langevin method with $(s, k) = (-1, 0)$, which corresponds to the approximate model investigated in our Monte Carlo studies. (Right) The departure from the Pauli-matrix structure in the Complex Langevin method with $(s, k) = (-0.8, 0)$.

## 1.1 Organization of the thesis

The rest of this thesis is organized as follows.

The material presented in Chapter 2 is based on the collaborative project on the Monte Carlo simulation cooperation with M. Hirasawa, Y. Ito, J. Nishimura and A. Tsuchiya [11]. In Chapter 2, the research of the Monte Carlo simulation is organized as follows. In Section 2.1 we briefly review the Lorentzian type IIB matrix model. In Section 2.2 we discuss the space-time structure of the matrix configurations obtained by Monte Carlo simulation, and show that they are essentially described by the Pauli matrices. In Section 2.4 we provide theoretical understanding of the obtained results, and discuss the possibility of obtaining a regular space-time with the (3+1)D expanding behavior if the sign problem is treated correctly. Section 2.5 is devoted to a summary and discussions in the Monte Carlo simulation.

The material presented in Chapter 3 is based on the collaborative project on the Complex Langevin simulation cooperation with K. N. Anagnostopoulos, T. Azuma, M. Hirasawa, Y. Ito, J. Nishimura, S. K. Papadoudis and A. Tsuchiya. In this thesis, only numerical results the author obtained are presented. In Chapter 3, the research of the Complex Langevin simulation is organized as follows. In Section 3.1 we briefly review the Complex Langevin method. In Section 3.2 we deform the Lorentzian type IIB matrix model defined in Section 2.1 by introducing the two deformation parameters $s$ and $k$. In Section 3.3 we discuss how we apply the Complex Langevin method to the

Lorentzian type IIB matrix model. In Section 3.4 we focus on $(s, k) = (-1, 0)$ in the deformation parameter space, which corresponds to the approximate model investigated in Chapter 2. Indeed we observe the emergence of (3+1)D expanding space-time with the Pauli-matrix structure. In Section 3.5 we show our results for the worldsheet deformation parameter $s$ and the target space deformation parameter $k$ close to that for the Lorentzian model $(s, k) = (0, 0)$. We observe a clear departure from the Pauli-matrix structure. In Section 3.6 the behavior of the space-time structure generated by this simulation is summarized. Section 3.7 is devoted to a summary and discussions in the Complex Langevin simulations.

We conclude with summary, discussions and its outlook for further research in Chapter 4.

# Chapter 2

# Monte Carlo simulations of the space-time structure

The material presented in Chapter 2 is based on the collaborative project on the Monte Carlo simulation cooperation with M. Hirasawa, Y. Ito, J. Nishimura and A. Tsuchiya [11].

## 2.1 Brief review of the Lorentzian type IIB matrix model

We start with defining the Lorentzian type IIB matrix model and its simplified versions, and review some results obtained by Monte Carlo simulations

### 2.1.1 Definition of the Lorentzian type IIB matrix model

The action of the type IIB matrix model is given as [1]

$$S = S_{\mathrm{b}} + S_{\mathrm{f}}\,, \tag{2.1}$$

$$S_{\mathrm{b}} = -\frac{1}{4g^2}\,\mathrm{Tr}\left(\left[A_\mu, A_v\right]\left[A^\mu, A^v\right]\right)\,, \tag{2.2}$$

$$S_{\mathrm{f}} = -\frac{1}{2g^2}\,\mathrm{Tr}\left(\Psi_\alpha\left(\mathcal{C}\Gamma^\mu\right)_{\alpha\beta}\left[A_\mu, \Psi_\beta\right]\right)\,, \tag{2.3}$$

where $A_\mu$ $(\mu = 0, 1, \cdots, 9)$ and $\Psi_\alpha$ $(\alpha = 1, \cdots, 16)$ are bosonic and fermionic $N \times N$ traceless Hermitian matrices. The indices $\mu$ and $\nu$ are contracted with the Lorentzian

metric $\eta_{\mu\nu} = \mathrm{diag}(-1, 1, \ldots, 1)$. The $16 \times 16$ matrices $\Gamma^\mu$ and $\mathcal{C}$ are the 10-dimensional gamma matrices and the charge conjugation matrix, respectively, obtained after the Weyl projection. The action (2.1) has a manifest SO(9,1) Lorentz symmetry, under which $A_\mu$ and $\Psi_\alpha$ transform as a Lorentz vector and a Majorana-Weyl spinor, respectively. The "coupling constant" $g$ is merely a scale parameter, which can be absorbed by an appropriate rescaling of $A_\mu$ and $\Psi_\alpha$. The Euclidean version can be obtained by making a "Wick rotation" $A_0 = iA_{10}$, where $A_{10}$ is supposed to be Hermitian.

Formally, the action of the model can be obtained by dimensional reduction of the 10D $\mathcal{N} = 1$ SU($N$) SYM theory,

$$S_{\mathrm{SYM}} = -\frac{1}{g^2} \int d^{10}x \ \mathrm{Tr} \left\{ \frac{1}{4} \left[ D_\mu(x), D_\nu(x) \right]^2 + \frac{i}{2} \bar{\Psi}(x) \not{D}(x) \Psi(x) \right\} \ , \tag{2.4}$$

where $D_\mu(x) = \partial_\mu + iA_\mu(x)$ to a point, and takeing the $N \to \infty$ limit. After this projection, its matrix elements are independent of space and time coordinates.

In addition to the SO(9,1) Lorentz symmetry, the large-N reduced model of super Yang-Mills theory is invariant under the following symmetries:

$$\begin{aligned} \delta_\epsilon^{(1)} A_\mu &= i\bar{\epsilon}\Gamma_\mu \Psi \ , \\ \delta_\epsilon^{(1)} \Psi &= \frac{i}{2} \Gamma^{\mu\nu} \left[ A_\mu, A_\nu \right] \epsilon \ , \end{aligned} \tag{2.5}$$

$$\begin{aligned} \delta_\xi^{(2)} A_\mu &= 0 \ , \\ \delta_\xi^{(2)} \Psi &= \xi \mathbf{1}_N \ , \end{aligned} \tag{2.6}$$

$$\begin{aligned} \delta_T A_\mu &= c_\mu \mathbf{1}_N \ , \\ \delta_T \Psi &= 0 \ , \end{aligned} \tag{2.7}$$

$$\begin{aligned} \delta_G A_\mu &= i \left[ \lambda, A_\mu \right] \ , \\ \delta_G \Psi &= i[\lambda, \Psi] \ , \end{aligned} \tag{2.8}$$

where $\epsilon$, $\xi$ are 10D Majorana-Weyl spinor as Grassmann odd parameters, $c_\mu$ is a 10D constant vector, $\lambda$ is a $N \times N$ Hermitian matrix. Here it is obvious that the symmetry (2.5) is the zero volume limit of $\mathcal{N} = 1$ supersymmetry of the super Yang-Mills theory.

Then the sysmmetry (2.8) is the zero volume version of the 10D SU($N$) gauge symmetry in the infinitesimal form.

The space-time does not exist a priori in this model but as we will see below, it is expected to emerge dynamically from the eigenvalue distribution of the 10 bosonic matrices $A_\mu$. Up to the gauge symmetry (2.8) and the equation of motion for $\Psi$,

$$\Gamma^\mu \left[A_\mu, \Psi\right] = 0 \ ,$$

we have the following commutation relations:

$$\begin{aligned} &[\delta^{(1)}_{\epsilon^1}, \delta^{(1)}_{\epsilon^2}]A_\mu = 0 \ , \\ &[\delta^{(1)}_{\epsilon^1}, \delta^{(1)}_{\epsilon^2}]\Psi = 0 \ , \end{aligned} \tag{2.9}$$

$$\begin{aligned} &[\delta^{(2)}_{\xi^1}, \delta^{(2)}_{\xi^2}]A_\mu = 0 \ , \\ &[\delta^{(2)}_{\xi^1}, \delta^{(2)}_{\xi^2}]\Psi = 0 \ , \end{aligned} \tag{2.10}$$

$$\begin{aligned} &[\delta^{(1)}_{\epsilon}, \delta^{(2)}_{\xi}]A_\mu = -i\bar{\epsilon}\Gamma_\mu\xi \ , \\ &[\delta^{(1)}_{\epsilon}, \delta^{(2)}_{\xi}]\Psi = 0 \ , \end{aligned} \tag{2.11}$$

When we consider a linear combination of $\delta^{(1)}$ and $\delta^{(2)}$ as,

$$\begin{aligned} \tilde{\delta}^{(1)} &\equiv \delta^{(1)} + \delta^{(2)} \ , \\ \tilde{\delta}^{(2)} &\equiv i\left(\delta^{(1)} - \delta^{(2)}\right) \ , \end{aligned} \tag{2.12}$$

these commutation relations are written as

$$\begin{aligned} &\left[\tilde{\delta}^{(i)}_{\epsilon}, \tilde{\delta}^{(j)}_{\xi}\right] A_\mu = -2i\delta^{ij}\bar{\epsilon}\Gamma_\mu\xi \ , \\ &\left[\tilde{\delta}^{(i)}_{\epsilon}, \tilde{\delta}^{(j)}_{\xi}\right] \Psi = 0 \ , \end{aligned} \tag{2.13}$$

where $i$, $j$ runs over 1,2 respectively. The important thing about this result (2.13) is that (2.13) is 10D $\mathcal{N} = 2$ on-shell supersymmetry algebra when $A_\mu$ are regarded as degrees of freedom which expresses 10D space-time. From this point of view, (2.7) can be identified with the translation symmetry and the eigenvalues of the bosonic matrices $A_\mu$ can be interpreted as the 10D space-time coordinates.

This action of the type IIB matrix model can also be related to the Green-Schwarz action of superstring [13] by using the matrix regularization:

$$A_\mu^{IJ} \to X_\mu\left(\sigma_0, \sigma_1\right) \tag{2.14}$$

$$\Psi_\alpha^{IJ} \to \Psi_\alpha\left(\sigma_0, \sigma_1\right) \tag{2.15}$$

$$-i[\ ,\ ] \to \frac{1}{N}\{\ ,\ \}\ , \tag{2.16}$$

$$\mathrm{Tr} \to N \int d^2\sigma \sqrt{g}\ . \tag{2.17}$$

In fact (2.3) reduces to the Green-Schwarz action in the Schild gauge [14] as

$$S_{\text{Schild}} = \int d^2\sigma \left[\sqrt{g}\alpha\left(\frac{1}{4}\left\{X^\mu, X^\nu\right\}^2 - \frac{i}{2}\bar{\Psi}\Gamma^\mu\left\{X^\mu, \Psi\right\}\right) + \beta\sqrt{g}\right]\ . \tag{2.18}$$

In this sense, 10D $\mathcal{N} = 2$ supersymmetry (2.13) of the type IIB matrix model is related to that of the Green-Schwarz action of superstring. Through this correspondence, the eigenvalues of $A_\mu$ matrices can also be identified with the $N$ points in the target space-time, which are expected to represent the continuum space-time in the large-$N$ limit.

The partition function of the Lorentzian type IIB matrix model is defined as [6]

$$Z = \int dA\, d\Psi\, e^{iS[A,\Psi]} = \int dA\, \mathrm{Pf}\mathcal{M}(A)\, e^{iS_{\mathrm{b}}}\ , \tag{2.19}$$

where the "$i$" in front of the action is motivated from the fact that the string worldsheet metric has a Lorentzian signature. Note that the bosonic action $S_{\mathrm{b}}$ can be written as

$$S_{\mathrm{b}} = \frac{1}{4}\mathrm{Tr}\left(F_{\mu\nu}F^{\mu\nu}\right) = \frac{1}{4}\left\{-2\mathrm{Tr}\left(F_{0i}\right)^2 + \mathrm{Tr}\left(F_{ij}\right)^2\right\}\ , \tag{2.20}$$

where we have introduced the Hermitian matrices $F_{\mu\nu} = i\left[A_\mu, A_\nu\right]$. Hence $S_{\mathrm{b}}$ is not positive semi-definite unlike in the Euclidean case. Note also that, unlike in the Euclidean version [3, 15], the matrix integral in (2.19) is divergent because $e^{iS_{\mathrm{b}}}$ is a pure phase factor and the Pfaffian $\mathrm{Pf}\mathcal{M}(A)$ obtained by integrating out the fermionic matrices is a polynomial in $A_\mu$.

In order to make the partition function (2.19) finite, we need to introduce the IR cutoffs both in the temporal and spatial directions, for instance, as

$$\frac{1}{N}\mathrm{Tr}\left\{(A_0)^2\right\}^p \leq \kappa^p \frac{1}{N}\mathrm{Tr}\left\{(A_i)^2\right\}^p \ , \tag{2.21}$$

$$\frac{1}{N}\mathrm{Tr}\left\{(A_i)^2\right\}^p \leq L^{2p} \ . \tag{2.22}$$

The power $p$ is a parameter, which can be used to test how much the obtained results depend on the way the IR cutoff is introduced [16]. While $p = 1$ would be a natural choice, it was proposed that $p$ should be chosen to be a slightly larger value in order to make the results almost independent of $p$. Too large values of $p$ lead to pathological behaviors, however.

The Pfaffian $\mathrm{Pf}\mathcal{M}(A)$ in (2.19) is real in the Lorentzian version unlike in the Euclidean version, where it becomes complex due to the replacement $A_0 = iA_{10}$. However, the phase factor $e^{iS_\mathrm{b}}$ causes the sign problem when one tries to investigate the Lorentzian model by Monte Carlo methods. Here, we avoid this problem[1] following previous work [6, 8, 10] by rewriting the partition function (2.19) as

$$Z = \int dA\, \mathrm{Pf}\mathcal{M}(A)\, \delta\Big(\frac{1}{N}\mathrm{Tr}F_{\mu\nu}F^{\mu\nu} - C\Big)\, \delta\Big(\frac{1}{N}\mathrm{Tr}\{(A_i)^2\}^p - 1\Big)\, \theta\Big(\kappa^p - \frac{1}{N}\mathrm{Tr}\{(A_0)^2\}^p\Big) \ , \tag{2.23}$$

where $\theta(x)$ is the Heaviside step function. This can be obtained by integrating out the overall scale factor of the bosonic matrices $A_\mu$ first and using certain approximation as discussed in Section 2.4. The parameter $C$ should be set to zero according to the "derivation", but we generalize the model by choosing $C \neq 0$, which allows us to obtain results for larger matrices in the original $C = 0$ model by using smaller matrices [8, 17]. In the next subsection we shall consider our numerical algorithm, which can be performed without the sign problem.

[1] Strictly speaking, the model (2.23) is not completely free of sign-problem because the Pfaffian is real but not positive semi-definite. However, configurations with positive Pfaffian dominates the path integral (2.23) at large $N$, and therefore one can safely replace the Pfaffian by its absolute value in the simulation.

### 2.1.2 Hybrid Monte Carlo algorithm

A convenient algorithm to simulate the partition function in (2.23) is the Hybrid Monte Carlo. Monte Carlo simulation of this model is explained below based on Appendix B of [8, 10], where for simplicity we omit $\mathrm{Pf}\mathcal{M}(A)$ and $p$ is set to 1.

As a first step, the delta functions are replaced by Gaussian potentials

$$V_{\mathrm{pot}} = \frac{1}{2}\gamma_C \left(\frac{1}{N}\mathrm{Tr}\left(F_{\mu\nu}F^{\mu\nu}\right)\right)^2 + \frac{1}{2}\gamma_L \left(\frac{1}{N}\mathrm{Tr}\left(A_i\right)^2 - 1\right)^2 \tag{2.24}$$

where the coefficients $\gamma_C$ and $\gamma_L$ are taken large enough to fix $\frac{1}{N}\mathrm{Tr}\left(F_{\mu\nu}F^{\mu\nu}\right)$ and $\frac{1}{N}\mathrm{Tr}\left(A_i\right)^2$ to the specified value.

In our algorism, we have to take care of the spontaneous breaking of the shift symmetry $A_0 \mapsto A_0 + \alpha\mathbf{1}$. Here we consider it by introducing a potential

$$V_{\mathrm{sym}} = \frac{1}{2}\gamma_{\mathrm{sym}}\ \Xi^2\,, \tag{2.25}$$

$$\Xi = \frac{1}{N}\left[\mathrm{Tr}\left(A_i\right)^2\right]_{\mathrm{L}} - \frac{1}{N}\left[\mathrm{Tr}\left(A_i\right)^2\right]_{\mathrm{R}}\,, \tag{2.26}$$

$$\left[\mathrm{Tr}\left(A_i\right)^2\right]_{\mathrm{L}} = \sum_{i=1}^{D-1}\sum_{a+b<N+1}\left(A_i\right)_{ab}\left(A_i\right)_{ba}\,, \tag{2.27}$$

$$\left[\mathrm{Tr}\left(A_i\right)^2\right]_{\mathrm{R}} = \sum_{i=1}^{D-1}\sum_{a+b>N+1}\left(A_i\right)_{ab}\left(A_i\right)_{ba}\,, \tag{2.28}$$

where the values of the coefficient $\gamma_{\mathrm{sym}}$ should be chosen large.

To summarize, the model we study by Monte Carlo simulation is given by

$$Z = \int \prod_{a=1}^{N} d\alpha_a \prod_{i=1}^{D-1} dA_i\ e^{-S_{\mathrm{eff}}}\,, \tag{2.29}$$

$$S_{\mathrm{eff}} = -2\log\Delta(\alpha) + V_{\mathrm{pot}} + V_{\mathrm{sym}}\,, \tag{2.30}$$

where as we will see in the next subsection, $A_0$ is diagonalized. The simulation of the model (2.30) can be performed by using the Hybrid Monte Carlo method. First we rewrite the model by introducing auxiliary variables $p_a$ and $(X_i)_{ab}$ $(a, b = 1, \ldots, N)$ with the action

$$S_{\text{HMC}} = \frac{1}{2}\sum_a (p_a)^2 + \frac{1}{2}\,\text{Tr}\,(X_i)^2 + S_{\text{eff}}[\alpha, A]\ , \tag{2.31}$$

where $p_a$ are real variables which are regarded as the conjugate momenta of $\alpha_a$, whereas $X_i$ are traceless Hermitian matrices which are regarded as the conjugate momenta of $A_i$. Then we regard $S_{\text{HMC}}$ as the Hamiltonian $H$.

The basic idea of the HMC algorithm is to generate the distribution in $p_a$, $\alpha_a$, $X_i$ and $A_i$ by first extracting values of $p_a$ and $X_i$ according to their Gaussian distribution and then performing molecular dynamics evolutions of $p_a$, $\alpha_a$, $X_i$ and $A_i$ which keep the total energy unchanged, obtaining updated values of $\alpha_a$ and $A_i$ as a final result.

The HMC algorithm as applied to our system can be described as follows.

1. Generate random initial configurations of $p_a(0)$, $X_i(0)$ with Gaussian distribution $\propto e^{-\frac{1}{2}\sum_a (p_a)^2}$ and $e^{-\frac{1}{2}\,\text{Tr}(X_i)^2}$, respectively.

2. Starting from the previous configuration at $\tau = 0$, a new configuration at $\tau = \tau_f$ is generated by numerically solving the Hamilton equations, *i.e.*

$$\begin{aligned} \frac{d\alpha_a}{d\tau} &= \frac{\partial H}{\partial p_a} = p_a, \quad & \frac{dp_a}{d\tau} &= -\frac{\partial H}{\partial \alpha_a} = -\frac{\partial S_{\text{eff}}}{\partial \alpha_a}\ , \\ \frac{dA_i}{d\tau} &= \frac{\partial H}{\partial X_i} = X_i^*, \quad & \frac{dX_i}{d\tau} &= -\frac{\partial H}{\partial A_i} = -\frac{\partial S_{\text{eff}}}{\partial A_i}\ , \end{aligned} \tag{2.32}$$

   for some fictitious time $\tau$. This part of the algorithm is called the molecular dynamics. In order to solve the Hamilton equations numerically, we discretize them using the so-called leap-frog discretization, which maintains reversibility with respect to $\tau$.

3. The new configuration at $\tau = \tau_f$ is accepted with probability $\min\left(1, \exp\left(-\Delta S_{\text{HMC}}\right)\right)$, where $\Delta H \equiv H\left(\tau_{\text{f}}\right) - H(0)$, following the idea of the Metropolis algorithm to satisfy the detailed balance. The important point here is that $H$ is preserved in the classical dynamics if the Hamilton equations are solved exactly. $H$ becomes, however, non-zero due to the discretization, but it is guaranteed to be a small quantity of the order of $(\Delta\tau)^2$.

In this way we can obtain the sequence of the configurations which is distributed with the correct $e^{-S_{\text{eff}}[\alpha,A]}$ probability.

### 2.1.3 SSB of rotational SO(9) symmetry

Next we discuss how one can extract the time-evolution from a given matrix configuration generated by Monte Carlo simulation [6]. Since the eigenvalues of the temporal matrix $A_0$ represents time, we work in an SU($N$) basis which diagonalizes $A_0$ as

$$A_0 = \text{diag}(\alpha_1, \dots, \alpha_N) \ , \ \text{where } \alpha_1 < \cdots < \alpha_N \ . \tag{2.33}$$

In this basis, the spatial matrices $A_i$ turn out to have an approximate band-diagonal structure. By this, we mean that there exists[2] some integer $n$ such that the elements of the spatial matrices $(A_i)_{ab}$ for $|a-b| > n$ are much smaller than those for $|a-b| < n$. Thanks to this structure, we can naturally consider the $n \times n$ submatrices $\bar{A}_i$

$$\left(\bar{A}_i\right)_{IJ}(t) \equiv (A_i)_{\nu+I,\nu+J} \tag{2.34}$$

representing the state at time $t$ defined by

$$t \equiv \frac{1}{n}\sum_{I=1}^{n} \alpha_{\nu+I} \ , \tag{2.35}$$

where $I, J = 1, \dots, n$ and $\nu = 0, 1, \dots, N-n$. For example, we can define the extent of the 9D space at time $t$ using $\bar{A}_i(t)$ as

$$R^2(t) = \left\langle \sum_{i=1}^{9} \frac{1}{n} \text{tr}\left(\bar{A}_i(t)\right)^2 \right\rangle \ , \tag{2.36}$$

where the symbol "tr" represents a trace over the $n \times n$ submatrix. We can also define the "moment of inertia tensor"

$$T_{ij}(t) = \frac{1}{n} \text{tr}\left(\bar{A}_i(t)\bar{A}_j(t)\right) \ , \tag{2.37}$$

[2] In practice, the integer $n$ can be determined by observing the scaling behavior for $\sum_i |(A_i)_{ab}|^2$ with $(a+b)/2$ fixed to different values corresponding to different time slices. See section 5 of [10] for the details.

which is a $9 \times 9$ real symmetric tensor. The eigenvalues of $T_{ij}(t)$ represent the spatial extent in each of the nine directions at time $t$, and we denote them by $\lambda_i(t)$ with the ordering

$$\lambda_1(t) > \lambda_2(t) > \cdots > \lambda_9(t) \ . \tag{2.38}$$

Note that $R^2(t)$ and $\lambda_i(t)$ are related as

$$R^2(t) = \langle T \rangle = \sum_{i=1}^{9} \langle \lambda_i(t) \rangle \ . \tag{2.39}$$

The expectation values $\langle \lambda_i(t) \rangle$ can be used as the order parameters for the spontaneous breaking of the rotational SO(9) symmetry of the model. If the nine eigenvalues do not approach a common value in the large-$N$ limit, we conclude that the SO(9) symmetry is spontaneously broken. From the Monte Carlo simulations of the model (2.23), it was found [6] that the three eigenvalues $\langle \lambda_i(t) \rangle$ $(i = 1, 2, 3)$ start to grow with $t$ after a critical time $t_{\rm c}$, which implies that the SO(9) symmetry is spontaneously broken down to SO(3) for $t > t_{\rm c}$. (See [8, 10] for a precise definition of the critical time $t_{\rm c}$, which we use in this work.)

### 2.1.4 Expanding behaviors in the simplified models

It is interesting to investigate how the 3D space expands with time. For that, one clearly needs to increase the matrix size, which is very time-consuming due to the existence of the Pfaffian in (2.23). This led to the proposal of the simplified models, the VDM model [8] and the bosonic model [10], which amounts to replacing the Pfaffian as

$$\mathrm{Pf}\mathcal{M}(A) \Longrightarrow \begin{cases} \Delta(\alpha)^{16} & \text{for the VDM model} \ , \\ 1 & \text{for the bosonic model} \ , \end{cases} \tag{2.40}$$

where $\Delta(\alpha) \equiv \prod_{a>b}^{N} (\alpha_a - \alpha_b)$ is the van der Monde (VDM) determinant. This replacement reduces the computational cost from $O(N^5)$ to $O(N^3)$, which enables simulations with considerably large matrix size. These two models are expected to describe the qualitative behaviors of the original model at early times and at late times, respectively.

In both these models, the spontaneous breaking of the SO(9) rotational symmetry to SO(3) was observed after some critical time as in the original model, and the rate of

expansion at late times was investigated. In the VDM model, the extent of space $R(t)$ defined in (2.36) exhibits an exponential growth [8]

$$R(t) \sim e^{\Lambda t} \,, \tag{2.41}$$

which is reminiscent of inflation[3] , and this behavior does not seem to change with increasing $t$. In the bosonic model, on the other hand, the exponential expansion observed at early times changes into a power-law expansion [10]

$$R(t) \sim t^{1/2} \tag{2.42}$$

at later times, which is reminiscent of the Friedmann-Robertson-Walker Universe at the radiation dominated era. Based on these results, it has been speculated that the extent of space $R(t)$ in the original model shows an exponential growth at early times and a power-law expansion at later times. If true, it implies that the e-folding or the duration of the cosmic inflation may be determined dynamically in the original model.

## 2.2 Space-time structure of the matrix configurations

In this section, we investigate the space-time structure of the matrix configurations generated by the Monte Carlo simulation of the model (2.23) and the simplified models (2.40).

### 2.2.1 Results for the bosonic model

In this subsection, we consider the bosonic model, which is a simplified model for the late time behaviors. Let us first look at the basic quantities such as the extent of space $R^2(t)$ and the eigenvalues $\langle \lambda_i(t) \rangle$ of $T_{ij}(t)$. In Figure 2.1 we plot the extent of space $R^2(t)/R^2(t_c)$ (Top-Left) and the normalized eigenvalues $\langle \lambda_i(t) \rangle / R^2(t_c)$ of $T_{ij}(t)$ (Top-Right) against $(t - t_c)/R(t_c)$ for $N = 256$, $C = 100$, $\kappa = 1.0$ with the block size $n = 18$ in (2.36). Here and for all the other plots in Figure 2.1, we only present the

[3] This behavior was observed also in the original model [9] although the matrix size used was not large enough to confirm the long-time behavior.

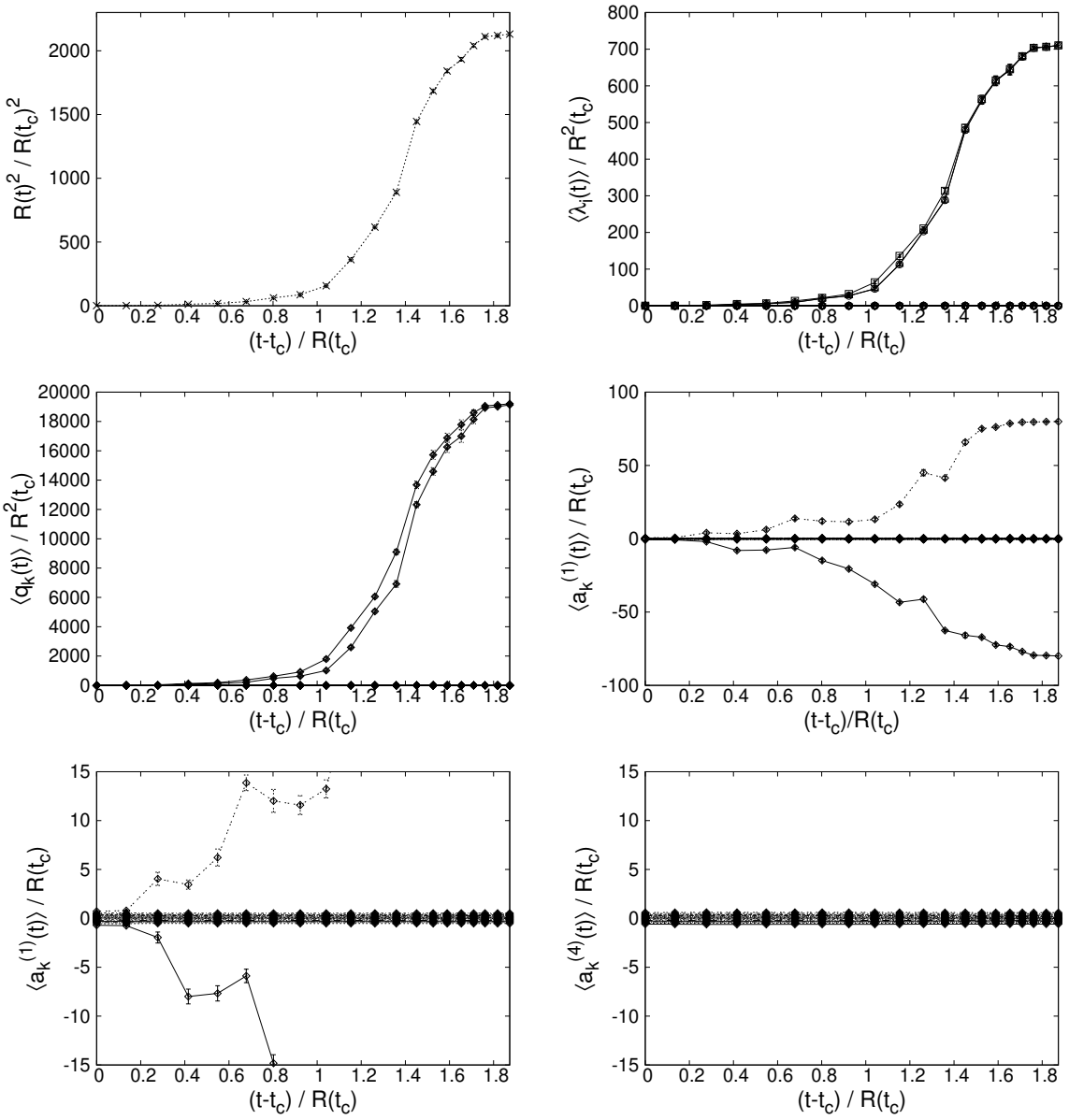


**Figure 2.1:** The extent of space $R^2(t)/R^2(t_c)$ (Top-Left) and the normalized eigenvalues $\langle\lambda_i(t)\rangle/R^2(t_c)$ of $T_{ij}(t)$ (Top-Right) are plotted against time $(t-t_c)/R(t_c)$ for the bosonic model with $N = 256$, $C = 100$, $\kappa = 1$, $p = 1.5$ and the block size $n = 18$. Similarly, the eigenvalues of $Q(t)/R^2(t_c)$ (Middle-Left), the eigenvalues of $\bar{A}^{(1)}(t)/R(t_c)$ (Middle-Right, Bottom-Left, the latter being the zoom-up version of the former), the eigenvalues of $\bar{A}^{(4)}(t)/R(t_c)$ (Bottom-Right) are plotted against time $(t-t_c)/R(t_c)$.

results in the $t < 0$ region since the results are symmetric[4] under the time reflection $t \mapsto -t$. The power $p$ in the IR cutoff (2.21) and (2.22) is chosen to be $p = 1.5$, which is found to be large enough to make the results almost independent of $p$ (See Section 2.3). Let us recall that $R^2(t)$ is related to $\langle \lambda_i(t) \rangle$ through (2.39). While the extent of space $R^2(t)/R^2(t_c)$ grows with $t$ for $t > t_c$, it is only three out of nine eigenvalues of $T_{ij}(t)$ that grow with $t$, which suggests that the rotational SO(9) symmetry is broken spontaneously to SO(3). These results are analogous to the previous results obtained for $p = 1$ [9].

The simplest way to probe the space-time structure is to define an $n \times n$ matrix

$$Q(t) \equiv \sum_{i=1}^{9} (\bar{A}_i(t))^2, \tag{2.43}$$

which is invariant under SO(9) rotations. Let us denote its eigenvalues as $q_k(t)$ $(k = 1, \cdots, n)$ with the ordering

$$q_1(t) < \cdots < q_n(t) \ . \tag{2.44}$$

These eigenvalues tell us how the space spreads in the radial direction at each time $t$.

In Figure 2.1 (Middle-Left), we plot the eigenvalues $q_k(t)/R^2(t_c)$ against $(t-t_c)/R(t_c)$. We find that the two largest eigenvalues grow with $t$, but not the others. Let us note that the eigenvalues of $Q(t)$ are related to the extent of space $R^2(t)$ as

$$R^2(t) = \left\langle \frac{1}{n} \mathrm{tr} Q(t) \right\rangle = \left\langle \frac{1}{n} \sum_{k=1}^{n} q_k(t) \right\rangle \ . \tag{2.45}$$

This implies that the time-dependence of $R^2(t)$ seen in the Top-Left panel is caused only by the two largest eigenvalues of $Q(t)$.

Let us next discuss the space-time structure in the three extended directions and the six shrunken directions separately. Since we are dealing with spontaneous symmetry breaking, we need to choose the frame properly in order to distinguish these directions. Suppose $v_j^{(i)}(t)$ $(j = 1, \cdots, 9)$ are the normalized eigenvectors of the "moment of inertia tensor" (2.37) corresponding to the eigenvalues $\lambda_i(t)$ with the ordering (2.38). Then, we

[4] This does not mean that the Big Crunch occurs in this model because the time difference between the symmetric point $t = 0$ and the critical time $t = t_c$ seems to diverge in physical units in an appropriate large-$N$ limit. See Section 2.2.3.

can define the $n \times n$ matrix corresponding to the spatial direction with the extent $\lambda_i$ as

$$\bar{A}^{(i)}(t) = \sum_{j=1}^{9} v_j^{(i)}(t)\, \bar{A}_j(t) \tag{2.46}$$

and its eigenvalues $a_k^{(i)}(t)$ $(k = 1, \cdots, n)$ with the ordering

$$a_1^{(i)}(t) < \cdots < a_n^{(i)}(t) \ . \tag{2.47}$$

In Figure 2.1 (Middle-Right), we plot the eigenvalues $a_k^{(1)}(t)/R(t_c)$ against $(t - t_c)/R(t_c)$. We find that only two eigenvalues $a_1^{(1)}(t)$ and $a_n^{(1)}(t)$ grow in magnitude with time $t$, and all the others remain close to zero. Similar behaviors are seen also for the eigenvalues $a_k^{(2)}(t)$ and $a_k^{(3)}(t)$ obtained for the other extended directions. In Figure 2.1 (Bottom-Left), we zoom up the same plot to make visible the eigenvalues close to zero. In Figure 2.1 (Bottom-Right), we plot the eigenvalues $a_k^{(4)}(t)/R(t_c)$ against $(t - t_c)/R(t_c)$. We find that all the eigenvalues remain close to zero. Similar behaviors are seen also for the eigenvalues $a_k^{(5)}(t), \cdots, a_k^{(9)}(t)$ obtained for the other shrunken directions. Comparing the two plots at the bottom of Figure 2.1, we notice that the eigenvalue distribution of $\bar{A}^{(i)}$ is almost identical for the extended directions and the shrunken directions except for the two eigenvalues with large magnitude.

Similarly to (2.45), the eigenvalues of $\bar{A}^{(i)}(t)$ are related to the extent of space $\lambda_i(t)$ in the $i$th direction as

$$\lambda_i(t) = \frac{1}{n} \sum_{k=1}^{n} \left( a_k^{(i)}(t) \right)^2 \ . \tag{2.48}$$

Our observation implies that the spontaneous symmetry breaking of the SO(9) rotational symmetry seen in the Top-Right panel is caused only by the two eigenvalues of $\bar{A}^{(i)}(t)$ with large magnitude.

### 2.2.2 Including fermionic contributions

In order to seek for the possibility to obtain a regular space-time, we repeat the analysis in the previous subsection in the case of the original model (2.23) including fermionic contributions. Since the cost of Monte Carlo simulations increases from $O(N^3)$ to $O(N^5)$, here we restrict ourselves to a rather small matrix size $N = 16$.

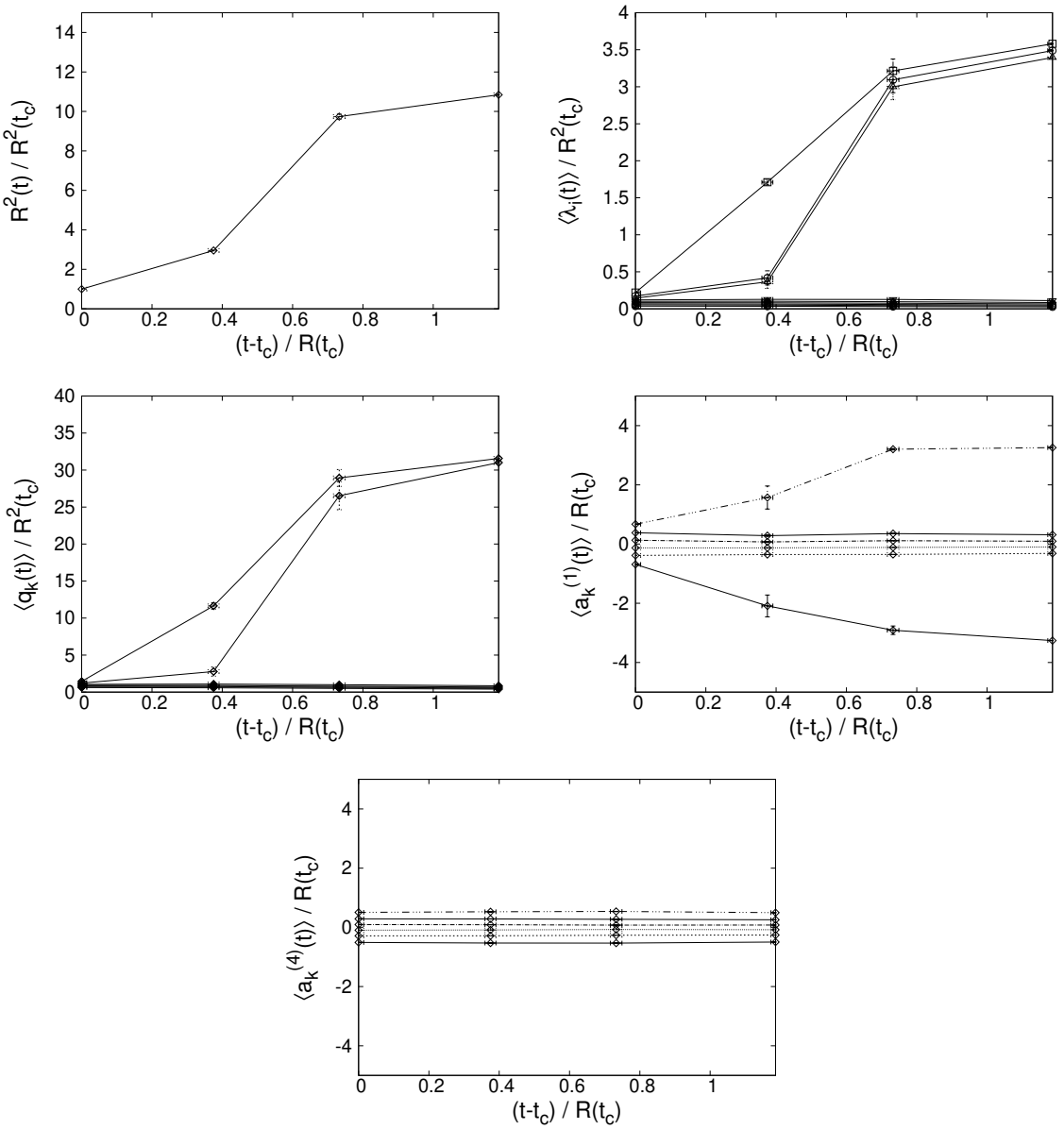


**Figure 2.2:** The extent of space $R^2(t)/R^2(t_c)$ (Top-Left) and the normalized eigenvalues $\langle\lambda_i(t)\rangle/R^2(t_c)$ of $T_{ij}(t)$ (Top-Right) are plotted against time $(t-t_c)/R(t_c)$ for the original model with $N = 16$, $C = 3.91$, $\kappa = 0.38$, $p = 1.6$ and the block size $n = 6$. Similarly, the eigenvalues of $Q(t)/R^2(t_c)$ (Middle-Left), the eigenvalues of $A^{(1)}(t)/R(t_c)$ (Middle-Right) and the eigenvalues of $A^{(4)}(t)/R(t_c)$ (Bottom) are plotted against time $(t-t_c)/R(t_c)$.

| $N$ | $C$ | $\kappa$ | $n$ | $\Delta$ | $\epsilon$ |
|---|---|---|---|---|---|
| 64 | 8.81 | 0.14 | 24 | 1.0990(16) | 0.0550(1) |
| 96 | 0 | 2.00 | 14 | 1.3811(41) | 0.1151(3) |
| 64 | 0 | 2.00 | 10 | 1.2726(63) | 0.1591(8) |
| 64 | 0 | 4.00 | 7 | 1.3762(87) | 0.2752(17) |

**Table 2.1:** The parameter sets ($N$, $C$, $\kappa$) used for the simulation of the VDM model are listed. We also present the block size $n$, the "volume" $\Delta$ and the "lattice spacing" $\epsilon$ determined from the data for each parameter set.

In Figure 2.2 we plot the same quantities as in Figure 2.1 for the original model with $N = 16$, $C = 3.91$, $\kappa = 0.38$ and the block size $n = 6$. The power $p$ in the IR cutoff (2.21) and (2.22) is chosen to be $p = 1.6$, which is found to be large enough to make the results almost independent of $p$ (See Section 2.3). These results are qualitatively the same as those obtained for the bosonic model. While the fermionic matrices are expected to play an important role in the properties of the model such as the expanding behavior, they do not seem to affect the singular space-time structure.

### 2.2.3 Taking the continuum limit

As yet another possibility to obtain a regular space-time, let us consider taking the continuum limit. Here we use the VDM model, which is a simplified model for the early time behaviors. In Figure 2.3 (Top-Left), we plot the extent of space $R^2(t)/R^2(t_c)$ against time $(t-t_c)/R(t_c)$ for various $N$, $C$ and $\kappa$ with the block size $n$ listed in Table 2.1. The power $p$ in the IR cutoff (2.21) and (2.22) is chosen as $p = 1.4$ following [16]. From this plot, we observe a clear scaling behavior for $(t - t_c)/R(t_c) \lesssim 0.40$.

In Figure 2.3 (Top-Right), we plot the normalized eigenvalues $\langle \lambda_i(t) \rangle / R^2(t_c)$ of $T_{ij}(t)$ for the VDM model with $N = 96$, $C = 0$ and $\kappa = 2$. Similar behaviors are obtained for the other parameter sets. We find that three out of nine eigenvalues of $T_{ij}(t)$ grow with time, which suggests that the rotational SO(9) symmetry is broken spontaneously to SO(3) for $t > t_c$. These results are similar to those obtained in [8, 16].

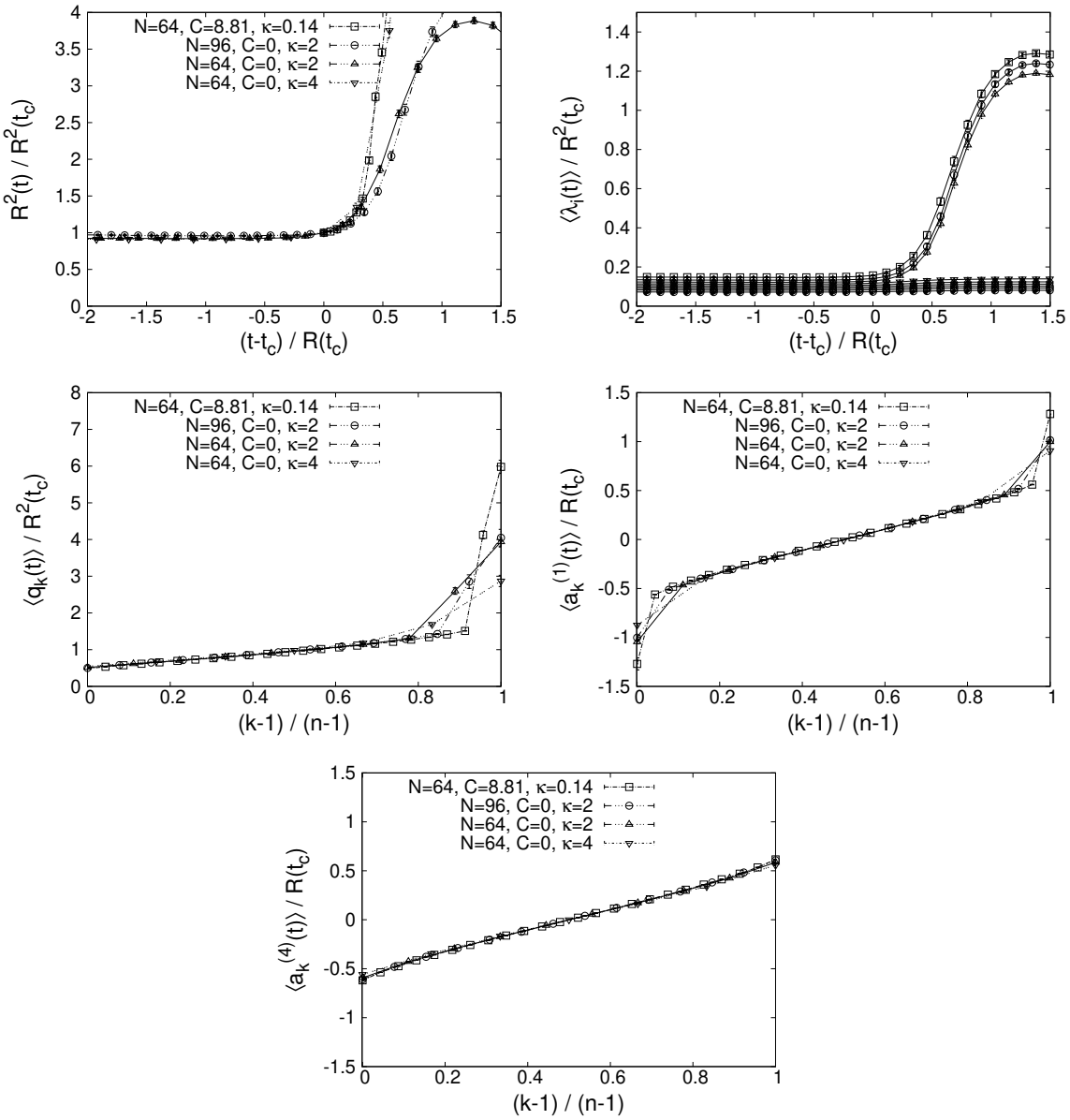


**Figure 2.3:** (Top-Left) The extent of space $R^2(t)/R^2(t_c)$ is plotted against time $(t-t_c)/R(t_c)$ for the VDM model with the parameter sets $(N,\ C,\ \kappa)$ and the block size $n$ listed in Table 2.1. The power $p$ in the IR cutoff (2.21) and (2.22) is chosen as $p = 1.4$. (Top-Right) The normalized eigenvalues $\langle\lambda_i(t)\rangle/R^2(t_c)$ of $T_{ij}(t)$ are plotted against time $(t-t_c)/R(t_c)$ for $N = 96$, $C = 0$, $\kappa = 2$. The eigenvalues of $Q(t)/R^2(t_c)$ (Middle-Left), the eigenvalues of $\bar{A}^{(1)}(t)/R(t_c)$ (Middle-Right) and the eigenvalues of $\bar{A}^{(4)}(t)/R(t_c)$ (Bottom) obtained at $(t-t_c)/R(t_c) \sim 0.40$ are plotted against their labels $(k-1)/(n-1)$ for the four parameter sets listed in Table 2.1.

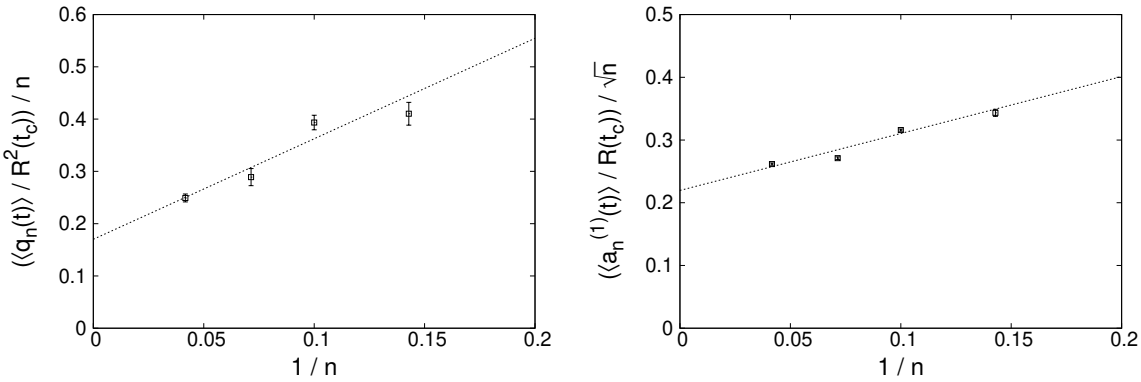


**Figure 2.4:** (Left) The largest eigenvalue $q_n(t)$ of the matrix $Q(t)$ obtained at $(t-t_{\rm c})/R(t_{\rm c}) \sim 0.40$ and normalized by $R^2(t_{\rm c})$ and $n$ is plotted against $1/n$. (Right) The largest eigenvalue $a_n^{(1)}(t)$ of the matrix $\bar{A}^{(1)}(t)$ obtained at $(t-t_{\rm c})/R(t_{\rm c}) \sim 0.40$ and normalized by $R(t_{\rm c})$ and $\sqrt{n}$ is plotted against $1/n$.

In order to discuss the continuum limit, let us define the "volume" and the "lattice spacing" in the temporal direction as [8]

$$\Delta \equiv \frac{t_{\rm peak} - t_{\rm c}}{R\left(t_{\rm c}\right)} \ , \qquad \epsilon \equiv \frac{\Delta}{\nu} \ , \tag{2.49}$$

where $t_{\rm peak}$ represents the position of the peak in $R^2(t)$ and $\nu$ is the number of data points of $R^2(t)$ contained within $t_{\rm c} < t \leq t_{\rm peak}$. Roughly speaking, the lattice spacing $\epsilon$ represents the average horizontal spacing between the adjacent data points of $R^2(t)/R^2(t_{\rm c})$. In Table 2.1, we present the volume $\Delta$ and the lattice spacing $\epsilon$ obtained for each parameter set $(N, C, \kappa)$ used in Figure 2.3. The deviation from the scaling behavior for $(t-t_{\rm c})/R(t_{\rm c}) > 0.40$ seen in Figure 2.3 can be understood either as the finite volume effects or as the finite lattice spacing effects depending on the parameter set.

In what follows, we focus on the point $(t-t_{\rm c})/R(t_{\rm c}) \sim 0.40$, at which the results for $R^2(t)/R^2(t_{\rm c})$ with the four parameter sets agree with each other. In Figure 2.3 (Middle-Left), we plot the normalized eigenvalues $\langle q_k(t)\rangle/R^2(t_{\rm c})$ $(k = 1, \cdots, n)$ of $Q(t)$ against their label $(k-1)/(n-1)$ for the four parameter sets. This reveals a clear scaling behavior except for the two largest eigenvalues, which grow as the lattice spacing $\epsilon$ decreases. This scaling behavior is consistent with the scaling of the ratio $R^2(t)/R^2(t_{\rm c})$ in the continuum limit [8, 10] seen in the Top-Left panel considering the relation (2.45). Note, however, that the time dependence of $R^2(t)/R^2(t_{\rm c})$ is caused by the two largest eigenvalues of $Q(t)$ as we have seen in the previous subsections. Therefore, the scaling of

$R^2(t)/R^2(t_c)$ implies that the two largest eigenvalues of $Q(t)$ should grow linearly in $n$ in the continuum limit. This is confirmed numerically in Figure 2.4 (Left) assuming the presence of $1/n$ corrections.

Let us next consider the space-time structure in the extended directions and the shrunken directions separately. In Figure 2.3 (Middle-Right), we plot the eigenvalues of $\bar{A}^{(1)}(t)/R(t_c)$ obtained at $(t - t_c)/R(t_c) \approx 0.40$ against the label $(k-1)/(n-1)$. Here again we observe a clear scaling behavior except for the ones at both ends of the spectrum. Similar behaviors are obtained for the other extended directions. According to the same argument as in the previous paragraph, we can deduce that the normalized eigenvalues at both ends of the spectrum grow in magnitude as $O(\sqrt{n})$ in the continuum limit, which is confirmed in Figure 2.4 (Right) assuming the presence of $1/n$ corrections.

In Figure 2.3 (Bottom), we plot the eigenvalues of $\bar{A}^{(4)}(t)/R(t_c)$ obtained at $(t - t_c)/R(t_c) \approx 0.40$ against the label $(k-1)/(n-1)$. We observe a clear scaling behavior here as well. In fact, the eigenvalues are almost the same as those for the extended directions except for the ones at both ends. Similar behaviors are obtained for the other shrunken directions.

Thus we find in the VDM model that the singular space-time structure becomes even more pronounced in the continuum limit instead of getting milder. It is surprising that the two eigenvalues of $\bar{A}^{(i)}(t)/R(t_c)$ $(i = 1, 2, 3)$ actually diverges in the continuum limit although the extent of space defined by $R^2(t)/R^2(t_c)$ remains finite. It is these two eigenvalues that cause the spontaneous breaking of the SO(9) rotational symmetry and the expansion of space. All the other eigenvalues of $\bar{A}^{(i)}(t)/R(t_c)$ remain finite and contribute only to the time-independent SO(9) symmetric part of the "moment of inertia tensor" $T_{ij}(t)$.

### 2.2.4 The Pauli-matrix structure

In this subsection, we provide deeper understanding of the singular space-time structure observed in the previous subsections. Let us work in the SU($n$) basis which diagonalizes $Q(t)$ at each time $t$ with the ordering (2.44), and consider the $2 \times 2$ submatrix $X_i(t)$ in the bottom-right corner of

$$\bar{A}^{(i)}(t) = \begin{pmatrix} * & * \\ * & X_i(t) \end{pmatrix} \tag{2.50}$$

for the extended directions $i = 1, 2, 3$. Here we use the VDM model with the parameter sets given in Table 2.1 and take the continuum limit focusing on the time $(t - t_c)/R(t_c) \approx 0.40$ as we did in Section 2.2.3.

We show below that the three matrices $X_i$ in (2.50) tend to satisfy the SU(2) Lie algebra

$$[X_i, X_j] = ic\epsilon_{ijk}X_k \tag{2.51}$$

for some real constant $c$ in the continuum limit. In order to determine the optimal value of $c$, we consider a quantity

$$S(c) \equiv \mathrm{tr}(i\epsilon_{ijk}[X_i, X_j] + 2cX_k)^2 \ , \tag{2.52}$$

which represents the violation of the relation (2.51). The value of $c$ that minimizes $S(c)$ can be readily obtained as

$$\tilde{c} = -\frac{i\epsilon_{ijk}\mathrm{tr}(X_k[X_i, X_j])}{2\mathrm{tr}(X_l^2)} \ . \tag{2.53}$$

Using $c = \tilde{c}$ as the optimal value for each configuration, we investigate to what extent the relation (2.51) is satisfied.

In Figure 2.5, we show a scatter plot for the real part (Left) and the imaginary part (Right) of each side of (2.51). The quantities on both sides are normalized by $\mathrm{tr}(X_l^2)$ so that they become invariant under the scale transformation $X_i \mapsto \mathrm{const.}X_i$. We observe that the data points tend to converge to the line $y = x$ as one goes from the top to the bottom corresponding to decreasing the lattice spacing $\epsilon$ (See Table 2.1.). This shows that the $2 \times 2$ matrices $X_i$ $(i = 1, 2, 3)$ tend to satisfy (2.51) in the continuum limit.

Thus we conclude that the singular space-time structure observed for the matrix configurations generated by simulations is essentially associated with the Pauli matrices. The Pauli matrices may be regarded as the simplest matrix configuration that has SO(3) symmetry in the sense that their SO(3) rotation can be absorbed by an appropriate SU($N$) transformation. Given the situation characterized by the two large eigenvalues of $Q(t)$, the appearance of the Pauli-matrix structure may not be that surprising.

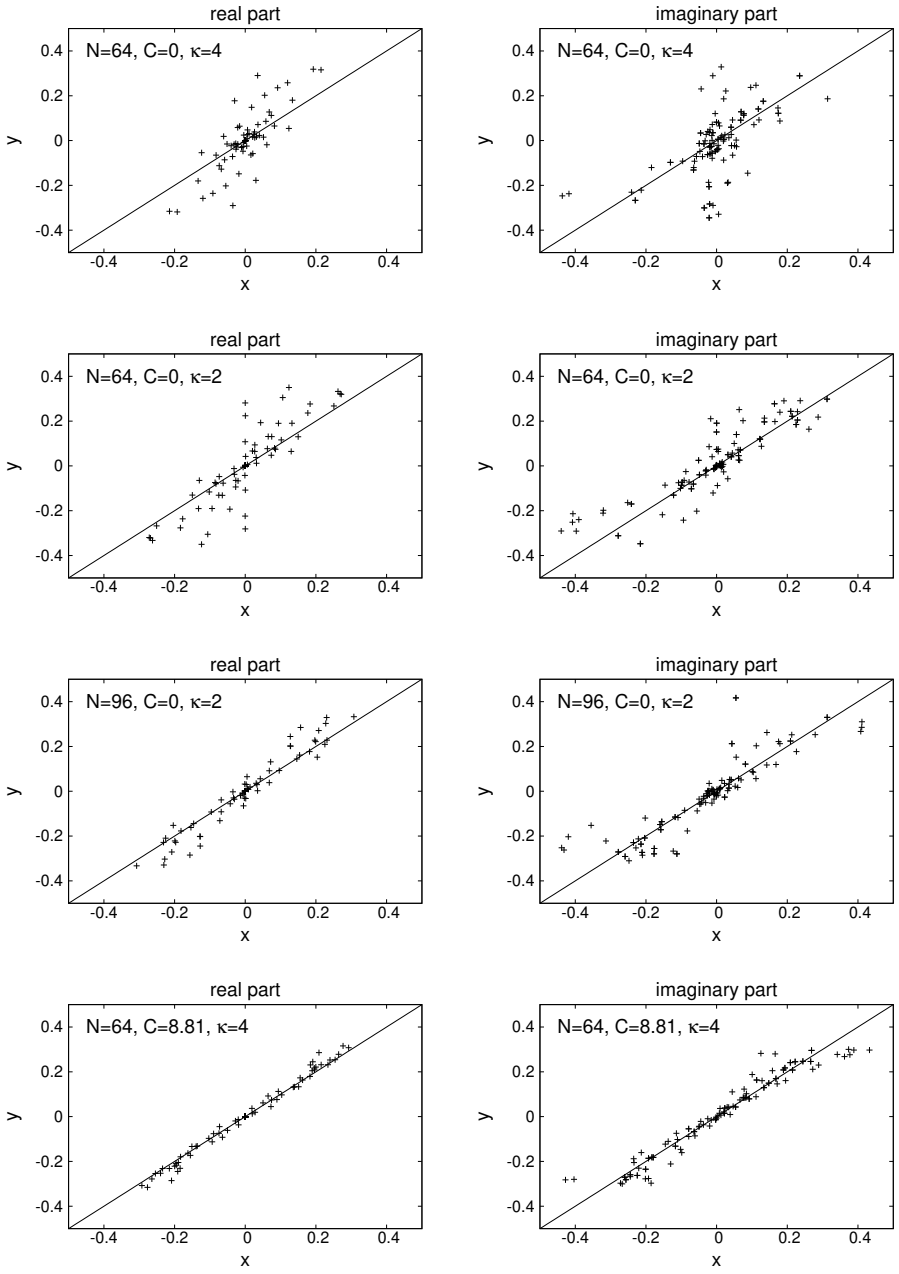


**Figure 2.5:** (Left) A scatter plot for the real part $x = \mathrm{Re}(i\tilde{c}\epsilon_{ijk}(X_k)_{ab})/\mathrm{tr}(X_l^2)$ and $y = \mathrm{Re}([X_i, X_j]_{ab})/\mathrm{tr}(X_l^2)$ of each side of (2.51) with (2.53) is shown for $(i, j) = (1, 2), (2, 3), (3, 1)$ and $(a, b) = (1, 1), (1, 2), (2, 2)$ using 10 configurations obtained by simulating the VDM model with the parameter sets given in Table 2.1. The solid line represents $y = x$. (Right) A scatter plot for the imaginary part $x = \mathrm{Im}(i\tilde{c}\epsilon_{ijk}(X_k)_{ab})/\mathrm{tr}(X_l^2)$ and $y = \mathrm{Im}([X_i, X_j]_{ab})/\mathrm{tr}(X_l^2)$ of each side of (2.51) with (2.53) is shown in the same way.

## 2.3 The determination of the parameter $p$

In this section, we explain how we determine the parameter $p$ in the IR cutoff (2.21) and (2.22). While a naive choice would be $p = 1$, it was proposed [16] that one should choose a slightly larger value so that the results become almost independent of $p$. There it was found in the VDM model that the results for the extent of space $R^2(t)$ become independent of $p$ when $p$ is larger[5] than $p_c = 1.2 \sim 1.3$. Based on this observation, we used $p = 1.4$ when we simulate the VDM model in Section 2.2.3.

Here we repeat the same analysis in the case of the bosonic model and the original model. In Figure 2.6, we plot the extent of space $R^2(t)/R^2(t_c)$ against time $(t-t_c)/R(t_c)$ for the bosonic model (Left) and the original model (Right), respectively, with various values of $p$. For all values of $p$, we find that only three directions start to expand at some critical time $t_c$. In the bosonic model, the results scale for $p = 1.3, 1.4, 1.5$ except for the data around the peak of $R^2(t)$. Similar scaling behavior is observed for the original model for $p = 1.4, 1.5, 1.6$. Based on these results, we use $p = 1.5$ for the bosonic model and $p = 1.6$ for the original model in sections 2.2.1 and 2.2.2, respectively.

## 2.4 A new interpretation of the simulation

In this section, we attribute the observed Pauli-matrix structure to the approximation involved in deriving the partition function (2.23), which was used in Monte Carlo simulation. We point out a subtlety in the approximation, and argue that the approximation amounts to replacing $e^{iS_b}$ by $e^{cS_b}$ in the original partition function (2.19). This new interpretation of the simulation provides us with a natural understanding of the (3+1)D expanding behavior with the Pauli-matrix structure discussed in Section 2.2. We also speculate on a possible scenario for the original model with the correct $e^{iS_b}$ factor.

### 2.4.1 The "derivation" of the partition function (2.23)

Let us first review how one can obtain the partition function (2.23) used in Monte Carlo simulation from the original partition function (2.19). (This was done in Appendix A of [8] for $p = 1$, but here we generalize it to arbitrary $p$.)

[5] For the values of $p$ in this region, it was also observed [16] from the analysis of the Schwinger-Dyson equations that the effect of the IR cutoff decreases as one takes the infinite volume limit.

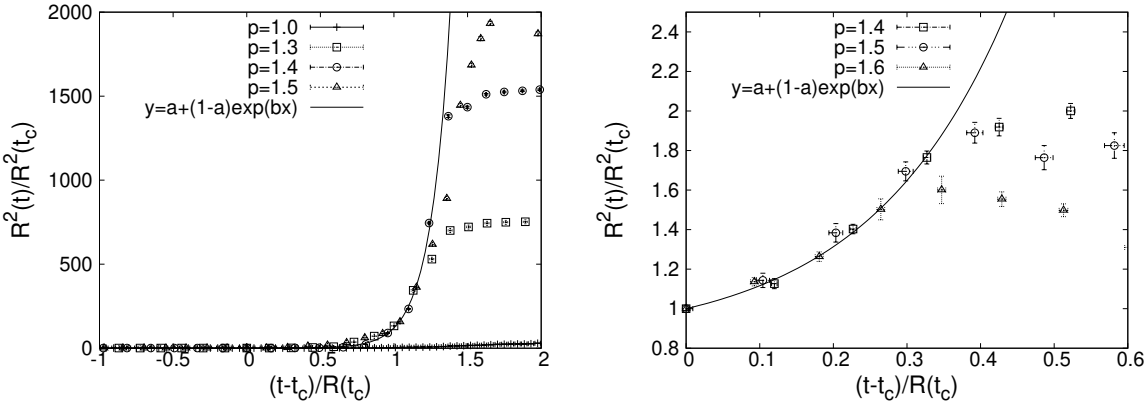


**Figure 2.6:** (Left) The extent of space $R^2(t)/R^2(t_c)$ obtained for the bosonic model is plotted against $x = (t - t_c)/R(t_c)$ for various values of $p$ with $N = 256$, $C = 100$, $\kappa = 1.0$. The block size is chosen as $n = 32, 24, 20, 18$ for $p = 1.0, 1.3, 1.4, 1.5$, respectively. The solid line represents a fit to the $p = 1.4$ data with $R^2(t)/R^2(t_c) = a+(1-a)\exp(bx)$, which gives $a = 0.92(5)$, $b = 7.3(6)$. (Right) The extent of space $R^2(t)/R^2(t_c)$ obtained for the original model is plotted against $x = (t-t_c)/R(t_c)$ for various values of $p$ with $N = 16$, $C = 5$, $\kappa = 0.46$. The block size is chosen as $n = 7, 6, 6$ for $p = 1.4, 1.5, 1.6$, respectively. The solid line represents a fit to the $p = 1.6$ data with $R^2(t)/R^2(t_c) = a + (1-a)\exp(bx)$, which gives $a = 0.83(4)$, $b = 5.3(7)$.

Note that the integrand of the partition function (2.19) involves a phase factor $e^{iS_b}$. As is commonly done in integrating oscillating functions, we introduce the convergence factor $e^{-\epsilon|S_b|}$ and take the $\epsilon \to 0$ limit after the integration.

The partition function can then be rewritten as

$$Z = \int dA \int_0^{L^{2p}} d\left(r^p\right) \delta\left(\frac{1}{N}\operatorname{Tr}\left\{\left(A_i\right)^2\right\}^p - r^p\right) \theta\left(\kappa^p r^p - \frac{1}{N}\operatorname{Tr}\left(A_0\right)^{2p}\right) e^{iS_b - \epsilon|S_b|} \operatorname{Pf}\mathcal{M}\,, \tag{2.54}$$

where $\kappa$ and $L$ are the cutoff parameters introduced in (2.21) and (2.22), respectively. Rescaling the variables $A_\mu \mapsto r^{1/2} A_\mu$ in the integrand, we get

$$Z = \int dA \operatorname{Pf}\mathcal{M}(A) f(S_b)\, \delta\left(\frac{1}{N}\operatorname{Tr}\left\{\left(A_i\right)^2\right\}^p - 1\right) \theta\left(\kappa^p - \frac{1}{N}\operatorname{Tr}\left(A_0\right)^{2p}\right)\,. \tag{2.55}$$

Here we have defined the function $f(S_b)$ by

$$f\left(S_b\right) \equiv \int_0^{L^{2p}} d\left(r^p\right) r^{9(N^2-1)-1} e^{r^2(iS_b - \epsilon|S_b|)}\,, \tag{2.56}$$

which is a complex-valued function with the property $f(-S_{\rm b}) = f(S_{\rm b})^*$.

For $|S_{\rm b}| \ll \frac{1}{L^4}$, the function can be well approximated by

$$f(S_{\rm b}) \approx \frac{p}{9\left(N^2-1\right)+p-1}\left(L^2\right)^{9(N^2-1)+p-1} \ . \tag{2.57}$$

For $|S_{\rm b}| \gtrsim \frac{1}{L^4}$, on the other hand, the phase of the integrand in (2.56) starts to oscillate violently in the region $r \gtrsim 1/\sqrt{|S_{\rm b}|}$, and hence the integral decreases rapidly in magnitude for increasing $|S_{\rm b}|$. In particular, the asymptotic behavior of $f(S_{\rm b})$ for $S_{\rm b} \gg \frac{1}{L^4}$ can be estimated as

$$\frac{|f(S_{\rm b})|}{f(0)} = \Gamma\left(\frac{9\left(N^2-1\right)+p+1}{2}\right)\left(\frac{1}{L^4\,|S_{\rm b}|}\right)^{\frac{9{\rm d}^2-1+p-1}{2}} + O\left(e^{-\epsilon L^4|S_{\rm b}|}\right) \tag{2.58}$$

by deforming the integration contour in (2.56).

Recalling (2.20), the condition $|S_{\rm b}| \ll \frac{1}{L^4}$ for (2.57) can be rewritten as

$$\left|\frac{1}{N}{\rm Tr}(F_{\mu\nu}F^{\mu\nu})\right| \ll \frac{4}{NL^4} \ . \tag{2.59}$$

Therefore, assuming that the right-hand side $\frac{4}{NL^4}$ of (2.59) becomes small at large $N$, we may make a replacement

$$f(S_{\rm b}) \Longrightarrow \delta\left(\frac{1}{N}{\rm Tr}(F_{\mu\nu}F^{\mu\nu})\right) \tag{2.60}$$

up to a normalization constant. For the bosonic model and the VDM model, one simply has to replace the Pfaffian in (2.54) and (2.55) as (2.40).

### 2.4.2 Subtlety in the derivation and the new interpretation

The only step in the derivation that may go wrong is the replacement (2.60). The subtlety in this replacement can be seen as follows. Note that the phase factor $e^{iS_{\rm b}}$ in the partition function (2.19) favors configurations at which the bosonic action $S_{\rm b}$ is stationary. On the other hand, the above approximation essentially replaces the phase factor $e^{iS_{\rm b}}$ by the delta function $\delta(S_{\rm b})$, which amounts to picking up configurations at which $S_{\rm b}$ is stationary only under rescaling $A_\mu \mapsto$ const $A_\mu$. While it is true that $|f(S_{\rm b})|$ is sharply peaked at $S_{\rm b} = 0$, the function $f(S_{\rm b})$ is actually a complex-valued function, whose phase rotates violently around $S_{\rm b} = 0$. This effect of the phase should be

responsible for favoring the configurations at which $S_{\rm b}$ is stationary. The approximation ignores this effect completely, and hence it cannot be justified.

If the model (2.23) is not equivalent to the original model (2.19), what kind of model does it actually correspond to? Here we point out that the constraint on $S_{\rm b}$ that appears in (2.23) may be regarded as the constraint one uses in defining a microcanonical ensemble. From this viewpoint, we consider that the model (2.23) is actually equivalent to the corresponding canonical ensemble with the Boltzmann weight $e^{cS_{\rm b}}$. The real parameter $c$ depends on the parameter $C$ in the constraint[6]. As we will see below, we consider that the model (2.23) corresponds essentially to replacing $e^{iS_{\rm b}}$ by $e^{cS_{\rm b}}$ with $c > 0$.

For $c > 0$, the first term in (2.20) that appears in $e^{cS_{\rm b}}$ favors configurations in which $A_0$ and $A_i$ commute. This means that the spatial matrices $A_i$ tend to become diagonal in the SU($N$) basis which diagonalizes $A_0$. On the other hand, the second term in (2.20) favors configurations in which the noncommutativity among the spatial matrices $A_i$ is large. The band-diagonal structure, which plays a crucial role in extracting the real-time evolution as in Section 2.1.3, can be understood as a consequence of the balance of these two effects.

We can also understand the reason for the (3+1)D expanding behavior with the Pauli-matrix structure. Here we assume that the first term in (2.20) is not important except in realizing the band-diagonal structure and focus on the effect of the second term in (2.20), which favors large $\mathrm{Tr}\left(F_{ij}\right)^2$, where $F_{ij} = i\left[A_i, A_j\right]$. We also have to take into account the constraint $\frac{1}{N}\mathrm{Tr}\left\{(A_i)^2\right\}^p = 1$, where we set $p = 1$ in what follows.

Simplifying the band-diagonal structure of the spatial matrices $A_i$ $(i = 1, \cdots, 9)$, we consider the block-diagonal structure given as

$$A_i = \begin{pmatrix} \bar{A}_i^{(1)} & & & \\ & \bar{A}_i^{(2)} & & \\ & & \ddots & \\ & & & \bar{A}_i^{(B)} \end{pmatrix} , \tag{2.61}$$

where $n$ is the common block size and $B$ is the number of blocks satisfying $N = nB$. Within this ansatz, we would like to maximize $\mathrm{Tr}(F_{ij})^2$ under the constraint $\frac{1}{N}\mathrm{Tr}(A_i)^2 =$

[6] This connection also provides clear justification of the renormalization-group-like method [8, 17], which amounts to tuning the parameter $C$ in order to obtain the late-time behaviors with smaller matrix size.

1. Note that we have

$$\frac{1}{N}\mathrm{Tr}(A_i)^2 = \frac{1}{B}\sum_{b=1}^{B}\frac{1}{n}\mathrm{Tr}(\bar{A}_i^{(b)})^2 \ , \tag{2.62}$$

$$\frac{1}{N}\mathrm{Tr}(F_{ij})^2 = \frac{1}{B}\sum_{b=1}^{B}\frac{1}{n}\mathrm{Tr}(\bar{F}_{ij}^{(b)})^2 \ , \tag{2.63}$$

where we have defined $\bar{F}_{ij}^{(b)} = i\,[\bar{A}_i^{(b)}, \bar{A}_j^{(b)}]$ for each block $b$.

Let us solve the maximization problem in two steps. First we fix

$$\frac{1}{n}\mathrm{Tr}(\bar{A}_i^{(b)})^2 = (r_b)^2 \ , \tag{2.64}$$

$$\frac{1}{B}\sum_{b=1}^{B}(r_b)^2 = 1 \ , \tag{2.65}$$

and maximize $\mathrm{Tr}(F_{ij})^2$ under this constraint. Following the discussion given in ref. [6], the solution to this first maximization problem can be written in terms of the Pauli matrices $\sigma_i$ as

$$\bar{A}_i^{(b)} = \frac{1}{\sqrt{6}} r_b\,(\sigma_i \oplus \mathbf{0}_{n-2}) \ , \tag{2.66}$$

for $i = 1, 2, 3$ and $\bar{A}_i^{(b)} = 0$ otherwise, up to the symmetries of the problem such as the SO(9) rotational symmetry and the SU($n$) symmetry within each block. The value of $\mathrm{Tr}(F_{ij})^2$ for (2.66) is given as

$$\mathrm{Tr}(F_{ij})^2 = \frac{2}{3}\sum_{b=1}^{B}(r_b)^4 \ . \tag{2.67}$$

As the second step of the maximization, we maximize (2.67) under the constraint (2.65). The maximum is given when all but one of the $r_b$'s are zero.

In reality, one should also take into account the entropic factor due to quantum fluctuations, which is expected to favor certain distribution of $r_b$. Due to the time-reversal symmetry $A_0 \mapsto -A_0$ of the model, the most natural distribution would be that $r_b$ is large around $t = 0$ and decreases with $|t|$. Thus we can understand the appearance of the (3+1)D expanding behavior with the Pauli-matrix structure.

### 2.4.3 A possible scenario for the original model

In the previous subsections, we have argued that the model (2.23) used for Monte Carlo simulation actually corresponds to a model with $e^{cS_{\rm b}}$ instead of $e^{iS_{\rm b}}$ in (2.19). This new interpretation explains naturally the (3+1)D expanding behavior with the Pauli-matrix structure. The crucial question then is what happens for the model with the correct $e^{iS_{\rm b}}$ factor. It is not easy to answer this question due to the sign problem, which occurs because $e^{iS_{\rm b}}$ is a pure phase factor and one cannot regard the integrand of the partition function (2.19) as the probability distribution. Here we speculate on a possible scenario based on the results obtained so far.

For that purpose, let us consider a generalized model with a factor $e^{c(\cos\theta + i\sin\theta)S_{\rm b}}$ ($0 \leq \theta \leq \pi/2$) which interpolates the two models. At $\theta = 0$, we obtain the model with the positive definite factor $e^{cS_{\rm b}}$ we have been studying, whereas at $\theta = \pi/2$, we obtain the model with $e^{icS_{\rm b}}$ we are aiming at. The scale parameter $c$ can be absorbed, if one wishes, by the redefinition $A_\mu \mapsto c^{-1/4}A_\mu$ and the replacement $L \mapsto c^{1/4}L$ in (2.22).

As far as $\theta < \pi/2$, the real part of the coefficient of $S_{\rm b}$ is positive. Therefore, certain effects favoring the band-diagonal structure and the Pauli-matrix structure in $A_i$ are at work. Note also that the classical equation of motion is common to all values of $\theta$. In fact, the classical equation of motion becomes valid at late times if the expansion of space occurs because each term in the bosonic action becomes large [18, 19]. Therefore, if some classical solution dominates for $\theta = 0$, the same solution may well dominate also for other $\theta$ less than some value $\theta_0$. From this argument, we speculate that the models with $0 \leq \theta \leq \theta_0$ are qualitatively the same.

As one approaches $\theta = \pi/2$, the real part of the coefficient of $S_{\rm b}$ becomes small, and different classical solutions may dominate. Note that the matrix configurations with the Pauli-matrix structure are obtained essentially by maximizing $S_{\rm b}$, but the classical solutions that can be obtained by *extremizing* $S_{\rm b}$ instead of *maximizing* it should have more variety. Indeed we have generated numerically many classical solutions that have (3+1)D expanding behavior and find for all of them that the matrix $Q(t)$ defined in (2.43) has a smooth eigenvalue distribution [20]. This is understandable since the configurations with the Pauli-matrix structure are actually disfavored entropically. Recall, for instance, that only two eigenvalues of the matrix $Q(t)$ are large, meaning that the entropy for such configurations must be small. It should be mentioned, however, that from the above classical analysis alone, one cannot single out the (3+1)D expanding space-time

because there are also other solutions with different dimensionality. Whether the (3+1)D expanding behavior remains even for $\theta \sim \pi/2$ is therefore a highly nontrivial question.

## 2.5 Summary and discussions

In this chapter we have investigated the space-time structure of the matrix configurations obtained in Monte Carlo studies of the Lorentzian type IIB matrix model and the simplified models. In these models, the time-evolution can be extracted from the matrix configurations by working in the SU($N$) basis which diagonalizes the temporal matrix $A_0$. The $n \times n$ spatial submatrices $\bar{A}_i(t)$ $(i = 1, \cdots, 9)$ at each time $t$ show that only three out of nine directions expand after some critical time suggesting the SSB of rotational SO(9) symmetry to SO(3). By calculating the eigenvalues of $\bar{A}_i(t)$ at each $t$, however, we have found that only two of them increase in magnitude with $t$ in the extended directions, while the rest are independent of $t$ and SO(9) symmetric. This implies that the SSB is caused only by the two eigenvalues. In the continuum limit, the magnitude of the two eigenvalues diverges in physical units and the spatial matrices $\bar{A}_i(t)$ approach a configuration which is essentially described by the Pauli matrices.

We have attributed this problem to the approximation used in Monte Carlo simulation to avoid the sign problem, which actually amounts to replacing $e^{iS_{\rm b}}$ by $e^{cS_{\rm b}}$ in the partition function (2.19) of the Lorentzian type IIB matrix model. This new interpretation of the Monte Carlo simulation enables us to understand the interesting aspects of the obtained results such as the band-diagonal structure of the spatial matrices $A_i$ as well as the appearance of the (3+1)D expanding behavior with the Pauli-matrix structure.

In order to discuss what happens in the original model, we have considered a model with a factor $e^{c(\cos\theta + i\sin\theta)S_{\rm b}}$, which interpolates the model we have been studying ($\theta = 0$) and the model we are aiming at ($\theta = \pi/2$). Using some arguments based on the classical equation of motion, which is common to all $\theta$, we have speculated that it is possible to obtain a regular space-time structure with the (3+1)D expanding behavior by approaching $\theta = \pi/2$ in the large-$N$ limit. The crucial point is that the Pauli-matrix structure is obtained by maximizing the action at the expense of reducing the entropy. By approaching $\theta = \pi/2$, one may obtain classical solutions which only extremize the action that have larger entropy due to a smooth eigenvalue distribution of the matrix $Q(t)$. The existence of such classical solutions with the (3+1)D expanding behavior has been confirmed numerically [20] (See Figure 2.7 and Figure 2.8). Whether such classical

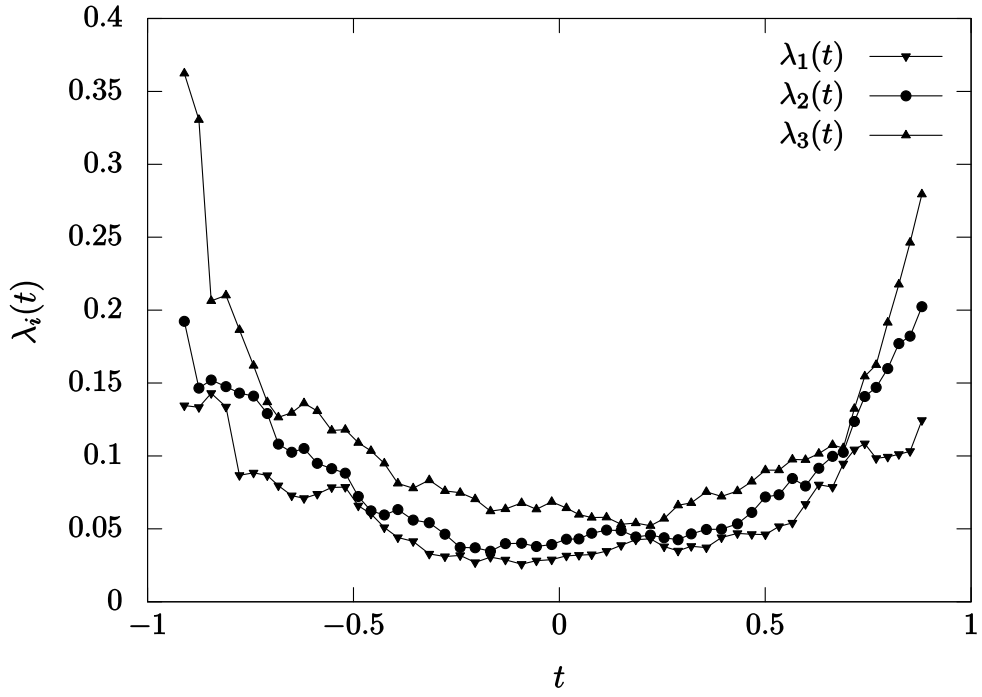


**Figure 2.7:** The eigenvalues $\lambda_i(t)$ of $T_{ij}(t)$ $(i, j = 1, 2, 3)$ are plotted against $t$ for the typical solution obtained by numerically solving the classical equation of motion, which is expected to be valid at late times since the action becomes large due to the expansion of space [20].

solutions appear from the full quantum theory by approaching $\theta = \pi/2$ remains to be seen.

Monte Carlo simulation of the interpolating model for $\theta \neq 0$ is difficult since the complex weight $e^{c(\cos\theta + i \sin\theta) S_{\mathrm{b}}}$ causes the sign problem. As a promising approach to overcome this problem, we may use the Complex Langevin method [21, 22], which has attracted much attention recently [23, 24, 25, 26, 27, 28, 29]. It was successful also in investigating the SSB of rotational symmetry in the 6d Euclidean type IIB matrix model [30]. Preliminary results [12] for the bosonic Lorentzian model suggest that by approaching $\theta = \pi/2$, one obtains clear deviations from the Pauli-matrix structure without losing the (3+1)D expanding behavior. We hope to see whether a regular (3+1)D expanding space-time emerges or not in the near future.

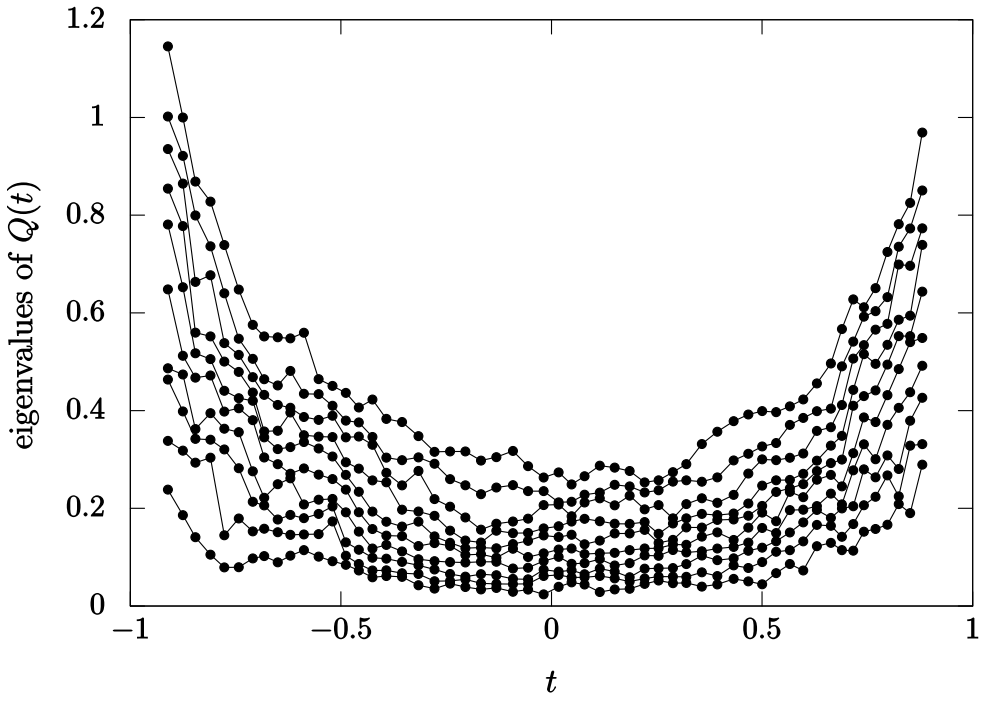


**Figure 2.8:** The eigenvalues of $Q(t)$ are plotted against $t$ for the typical solution obtained by numerically solving the classical equation of motion [20].

# Chapter 3

# Complex Langevin simulations of the space-time structure

The material presented in Chapter 3 is based on the collaborative project on the Complex Langevin simulation cooperation with K. N. Anagnostopoulos, T. Azuma, M. Hirasawa, Y. Ito, J. Nishimura, S. K. Papadoudis and A. Tsuchiya. In this Chapter 3, numerical results the author obtained are presented. They are preliminary results.

## 3.1 Brief review of Complex Langevin method

We start with defining the ordinary Lagevin method, and then review the Complex Langevin method.

### 3.1.1 Langevin method

We briefly review the ordinary Lagevin method, starting with the well-established case of non-negative real weight, which is known also under the name of stochastic quantization. Here we consider a system of $n$ real variables $x_k$ $(k = 1, \cdots, n)$ given by the partition function

$$Z = \int dx w(x) = \int \prod_k dx_k w(x) \ , \tag{3.1}$$

where the weight $w(x)$ is a function of the real variables $x = (x_1, \cdots, x_n)$.

When the weight is non-negative real($w(x) \geq 0$), we can use the ordinary Langevin method to study this system [31]. Introducing a fictitious time $\tau$, we consider the $\tau$-evolution governed by the Langevin equation

$$\frac{d}{d\tau}x_k^{(\eta)}(\tau) = v_k\left(x^{(\eta)}(\tau)\right) + \eta_k(\tau) \ , \tag{3.2}$$

where

$$v_k(x) \equiv w(x)^{-1}\frac{\partial w(x)}{\partial x_k} \ , \tag{3.3}$$

and $\eta_k(\tau)$ are probabilistic variables obeying the probability distribution which is the Gaussian noise

$$\exp\left(-\frac{1}{4}\int d\tau\,(\eta_k(\tau))^2\right) \ . \tag{3.4}$$

The first term and the second term on the right-hand side of the Langevin equation (3.2) are commonly called the drift term and the noise term, respectively, for historical reasons.

The probability distribution of the dynamical variables $x^{(\eta)}(\tau)$ can be defined as

$$P(x,\tau) = \left\langle \prod_k \delta\left(x_k - x_k^{(\eta)}(\tau)\right)\right\rangle_\eta \ , \tag{3.5}$$

where the expectation value $\langle\,\cdots\,\rangle_\eta$ is defined by

$$\langle\cdots\rangle_\eta = \frac{\int \mathcal{D}\eta\ \cdots \mathrm{e}^{-\frac{1}{4}\int d\tau\ \eta_k(\tau)^2}}{\int \mathcal{D}\eta\ \mathrm{e}^{-\frac{1}{4}\int d\tau\ \eta_k(\tau)^2}} \ . \tag{3.6}$$

Using this notation, one obtains, for instance, the expectation value of the correlation function for the probabilistic variables, which is given as

$$\langle\eta_k(\tau_1)\,\eta_l(\tau_2)\rangle_\eta = 2\delta_{kl}\delta(\tau_1-\tau_2) \ . \tag{3.7}$$

We can actually show with (3.2) that $P(x,\tau)$ satisfies the Fokker-Planck (FP) equation

$$\frac{\partial P}{\partial \tau} = \frac{\partial}{\partial x_k}\left(\frac{\partial}{\partial x_k} - v_k(x)\right)P \ , \tag{3.8}$$

which has a time-independent solution

$$P_{\text{time-indep}}\,(x) = \frac{1}{Z}\omega(x)\ . \tag{3.9}$$

$P(x,\tau)$ satisfying the FP equation converges to this time-independent solution for $\tau \to \infty$,

$$\lim_{\tau\to\infty} P(x,\tau) = \frac{1}{Z}w(x)\ . \tag{3.10}$$

We can therefore obtain the expectation value of the observable with respect to the partition function (3.1) as

$$\begin{aligned}
\left\langle \mathcal{O}\left(x^{(\eta)}(\tau)\right)\right\rangle_\eta &= \frac{1}{Z}\int dx\ \mathcal{O}(x)\ \omega(x) \\
&= \int dx\ \mathcal{O}(x) P_{\text{time-indep}}\,(x) \\
&= \lim_{\tau\to\infty}\int dx\ \mathcal{O}(x) P(x,\tau) \\
&= \lim_{\tau\to\infty}\left\langle \mathcal{O}\left(x^{(\eta)}(\tau)\right)\right\rangle_\eta \\
&= \lim_{T\to\infty}\frac{1}{T}\int_{\tau_0}^{\tau_0+T} d\tau\ \mathcal{O}\left(x^{(\eta)}(\tau)\right)
\end{aligned}$$

In the last step, the statistical average over $\eta$ is replaced by the time average assuming the ergodicity of the stochastic process as is done in usual Monte Carlo methods.

### The discretized Langevin equation

When one tries to solve the Langevin equation (3.2) numerically, one must discretize the fictitious time $\tau$ and solve, for instance,

$$x_k^{(\eta)}(\tau+\epsilon) = x_k^{(\eta)}(\tau) + \epsilon\left(v_k(x) + \eta_k(\tau)\right)\ , \tag{3.11}$$

where the probabilistic variables $\eta_k(\tau)$ obey the probability distribution

$$\exp\left(-\frac{1}{4}\epsilon\sum_\tau(\eta_k(\tau))^2\right)\ . \tag{3.12}$$

Let us rescale them as $\tilde{\eta}_k = \sqrt{\epsilon}\eta_k$ so that they obey the probability distribution

$$\exp\left(-\frac{1}{4}\sum_{\tau}(\tilde{\eta}_k(\tau))^2\right) \ . \tag{3.13}$$

and hence, in particular

$$\left\langle \tilde{\eta}_k\left(\tau_1\right)\tilde{\eta}_l\left(\tau_2\right)\right\rangle_\eta = 2\delta_{kl}\delta_{\tau_1,\tau_2} \ . \tag{3.14}$$

With this normalization, the discretized Langevin equation (3.11) becomes

$$x_k^{(\eta)}(\tau+\epsilon) = x_k^{(\eta)}(\tau) + \epsilon v_k(x) + \sqrt{\epsilon}\tilde{\eta}_k(\tau) \ . \tag{3.15}$$

Below we omit the tilde on $\eta_k$ to simplify the notation.

With this discretized version, we can derive the FP equation (3.8) in a more elementary manner than in the continuum [32]. Let us consider a test function $f(x)$ and its expectation value

$$\left\langle f\left(x^{(\eta)}(\tau)\right)\right\rangle_\eta = \int dx \ f(x)P(x;\tau) \tag{3.16}$$

at a fictitious time $\tau$. The $\tau$-evolution of this quantity is given by

$$\begin{aligned}
&\left\langle f\left(x^{(\eta)}(\tau+\epsilon)\right)\right\rangle_\eta - \left\langle f\left(x^{(\eta)}(\tau)\right)\right\rangle_\eta \\
&= \left\langle \frac{\partial f}{\partial x_k}\left(\epsilon v_k(x)\right) + \frac{1}{2}\frac{\partial^2 f}{\partial x_k \partial x_l}(\sqrt{\epsilon})^2\eta_k(\tau)\eta_l(\tau)\right\rangle_\eta + O\left(\epsilon^2\right) \\
&= \epsilon\int dx\left(\frac{\partial f}{\partial x_k}v_k(x) + \frac{\partial^2 f}{\partial x_k^2}\right)P(x;\tau) + O\left(\epsilon^2\right) \\
&= \epsilon\int dx f(x)\frac{\partial}{\partial x_k}\left(\frac{\partial}{\partial x_k} - v_k(x)\right)P + O\left(\epsilon^2\right) \ .
\end{aligned} \tag{3.17}$$

Here we have used

$$\left\langle \frac{1}{2}\frac{\partial^2 f}{\partial x_k \partial x_l}(\sqrt{\epsilon})^2\eta_k(\tau)\eta_l(\tau)\right\rangle_\eta = \frac{1}{2}\epsilon\left\langle \frac{\partial^2 f}{\partial x_k \partial x_l}\right\rangle_\eta \left\langle \eta_k(\tau)\eta_l(\tau)\right\rangle_\eta = \epsilon\left\langle \frac{\partial^2 f}{\partial x_k^2}\right\rangle_\eta \ , \tag{3.18}$$

which follows from the fact that the function $\frac{\partial^2 f}{\partial x_k \partial x_l}$ is evaluated at $x = x^{(\eta)}(\tau)$, which depends only on $\eta(0), \eta(\epsilon), \cdots, \eta(\tau-\epsilon)$, but not on $\eta(\tau)$. Using (3.16), the same quantity

(3.17) should be written as

$$\left\langle f\left(x^{(\eta)}(\tau+\epsilon)\right)\right\rangle_{\eta} - \left\langle f\left(x^{(\eta)}(\tau)\right)\right\rangle_{\eta} = \int dx f(x)(P(x;\tau+\epsilon) - P(x;\tau)) \ . \tag{3.19}$$

Since (3.17) and (3.19) should be equal for an arbitrary $f(x)$, one obtains

$$P(x;\tau+\epsilon) - P(x;\tau) = \epsilon \frac{\partial}{\partial x_k}\left(\frac{\partial}{\partial x_k} - v_k(x)\right) P + O\left(\epsilon^2\right) \tag{3.20}$$

Thus, in the $\epsilon \to 0$ limit, one obtains (3.8).

### 3.1.2 Complex Langevin method

Let us apply the same method to the case in which the weight $\omega$ is a complex-valued function ($w(x) \in \mathbb{C}$) of the real variables $x_k$ ($k = 1, \cdots, n$). In that case the drift term of the Langevin equation (3.2) becomes complex, which means that $x_k^{(\eta)}(\tau)$ becomes complex even if one starts from a real configuration $x_k^{(\eta)}(\tau = 0) \in \mathbb{R}$. Let us therefore complexify the variables as $x_k \mapsto z_k = x_k + iy_k$, and consider the complex Langevin equation

$$\frac{d}{d\tau} z_k^{(\eta)}(\tau) = v_k\left(z^{(\eta)}(\tau)\right) + \eta_k(\tau) \ , \tag{3.21}$$

where the drift term $v_k\left(z^{(\eta)}(\tau)\right)$ is obtained by analytically continuing (3.3). The probabilistic variables $\eta_k(\tau)$ in (3.21) are, in general, complex

$$\eta_k(\tau) = \eta_k^{(\mathrm{R})}(\tau) + i\eta_k^{(\mathrm{I})}(\tau) \ , \tag{3.22}$$

and obey the probability distribution

$$\exp\left[-\frac{1}{4}\int d\tau \left\{\frac{1}{N_{\mathrm{R}}}\eta_k^{(\mathrm{R})}(\tau)^2 + \frac{1}{N_{\mathrm{I}}}\eta_k^{(\mathrm{I})}(\tau)^2\right\}\right] \ , \tag{3.23}$$

where we must choose

$$N_{\mathrm{R}} - N_{\mathrm{I}} = 1 \ . \tag{3.24}$$

For practical purposes, one should actually use $N_{\mathrm{R}} = 1$, $N_{\mathrm{I}} = 0$, corresponding to real $\eta_k(\tau)$, to reduce the excursion in the imaginary directions, which spoils the validity of the method [24, 25, 33].

The probability distribution corresponding to (3.5) is defined as

$$P(x, y; \tau) = \left\langle \prod_k \delta\left(x_k - x_k^{(\eta)}(\tau)\right) \delta\left(y_k - y_k^{(\eta)}(\tau)\right) \right\rangle_\eta \ , \tag{3.25}$$

where the expectation value $\langle \cdots \rangle_\eta$ is defined by

$$\langle \cdots \rangle_\eta = \frac{\int \mathcal{D}\eta \ \cdots \mathrm{e}^{-\frac{1}{4}\int d\tau \left\{ \frac{1}{N_{\mathrm{R}}} \eta_k^{(\mathrm{R})}(\tau)^2 + \frac{1}{N_{\mathrm{I}}} \eta_k^{(\mathrm{I})}(\tau)^2 \right\}}}{\int \mathcal{D}\eta \ \mathrm{e}^{-\frac{1}{4}\int d\tau \left\{ \frac{1}{N_{\mathrm{R}}} \eta_k^{(\mathrm{R})}(\tau)^2 + \frac{1}{N_{\mathrm{I}}} \eta_k^{(\mathrm{I})}(\tau)^2 \right\}}} \tag{3.26}$$

With this notation, we have, for instance,

$$\begin{aligned} \left\langle \eta_k^{(\mathrm{R})}(\tau_1)\, \eta_l^{(\mathrm{R})}(\tau_2) \right\rangle_\eta &= 2N_{\mathrm{R}} \delta_{kl} \delta(\tau_1 - \tau_2) \ , \\ \left\langle \eta_k^{(\mathrm{I})}(\tau_1)\, \eta_l^{(\mathrm{I})}(\tau_2) \right\rangle_\eta &= 2N_{\mathrm{I}} \delta_{kl} \delta(\tau_1 - \tau_2) \ , \\ \left\langle \eta_k^{(\mathrm{R})}(\tau_1)\, \eta_l^{(\mathrm{I})}(\tau_2) \right\rangle_\eta &= 0 \ . \end{aligned}$$

### The discretized Complex Langevin equation

The discretized complex Langevin equation is given by

$$z_k^{(\eta)}(\tau + \epsilon) = z_k^{(\eta)}(\tau) + \epsilon v_k(z) + \sqrt{\epsilon}\ \eta_k(\tau) \ , \tag{3.27}$$

The probabilistic variables $\eta_k(\tau)$ obey the probability distribution

$$\exp\left[ -\frac{1}{4} \sum_\tau \left\{ \frac{1}{N_{\mathrm{R}}} \eta_k^{(\mathrm{R})}(\tau)^2 + \frac{1}{N_{\mathrm{I}}} \eta_k^{(\mathrm{I})}(\tau)^2 \right\} \right] \ . \tag{3.28}$$

The expectation value $\langle \cdots \rangle_\eta$ is defined by

$$\langle \cdots \rangle_\eta = \frac{\int \mathcal{D}\eta \cdots \mathrm{e}^{-\frac{1}{4}\sum_\tau \left\{ \frac{1}{N_{\mathrm{R}}} \eta_k^{(\mathrm{R})}(\tau)^2 + \frac{1}{N_{\mathrm{I}}} \eta_k^{(\mathrm{I})}(\tau)^2 \right\}}}{\int \mathcal{D}\eta \ \mathrm{e}^{-\frac{1}{4}\sum_\tau \left\{ \frac{1}{N_{\mathrm{R}}} \eta_k^{(\mathrm{R})}(\tau)^2 + \frac{1}{N_{\mathrm{I}}} \eta_k^{(\mathrm{I})}(\tau)^2 \right\}}} \tag{3.29}$$

With this notation, we have,

$$\begin{aligned}\left\langle \eta_k^{(\mathrm{R})}(\tau_1)\,\eta_l^{(\mathrm{R})}(\tau_2)\right\rangle_\eta &= 2N_{\mathrm{R}}\delta_{kl}\delta_{\tau_1,\tau_2}\ ,\\ \left\langle \eta_k^{(\mathrm{I})}(\tau_1)\,\eta_l^{(\mathrm{I})}(\tau_2)\right\rangle_\eta &= 2N_{\mathrm{I}}\delta_{kl}\delta_{\tau_1,\tau_2}\ ,\\ \left\langle \eta_k^{(\mathrm{R})}(\tau_1)\,\eta_l^{(\mathrm{I})}(\tau_2)\right\rangle_\eta &= 0\ .\end{aligned}$$

### The condition for correct convergence

Then we discuss the case of complex weight focusing on the conditions for correct convergence. Here we review the refined argument for justification of the CLM, which leads to the condition for correct convergence [28].

Let us consider the expectation value of the observable $\mathcal{O}(x)$. In the Complex Langevin method (CLM), one can compute the expectation value of the holomorphic observable $\mathcal{O}(x+iy)$ defined as an analytic continuation of $\mathcal{O}(x)$ as

$$\Phi(\tau) = \left\langle \mathcal{O}\left(z^{(\eta)}(\tau)\right)\right\rangle_\eta = \int dxdy\ \mathcal{O}(x+iy)P(x,y;\tau)\ . \tag{3.30}$$

Then, the correct convergence of the CLM implies the equality

$$\lim_{\tau\to\infty}\lim_{\epsilon\to 0}\Phi(\tau) = \frac{1}{Z}\int dx\ \mathcal{O}(x)w(x)\ , \tag{3.31}$$

where the right-hand side is the expectation value of $\mathcal{O}(x)$ in the original theory (3.1), where the weight is complex.

The basic idea in proving the equality (3.31) is to consider the time evolution of the expectation value $\Phi(\tau)$, which is given by

$$\Phi(\tau+\epsilon) = \int dxdy\ \mathcal{O}_\epsilon(x+iy)P(x,y;\tau)\ , \tag{3.32}$$

where we have defined the time-evolved observable

$$\mathcal{O}_\epsilon(z) = \frac{1}{\mathcal{N}}\int d\eta\ e^{-\frac{1}{4}\eta^2}\mathcal{O}(z+\epsilon v(z)+\sqrt{\epsilon}\eta) \tag{3.33}$$

Note that if $\mathcal{O}(z)$ and $v(z)$ are holomorphic, so is $\mathcal{O}_\epsilon(z)$. Expanding the right-hand side of (3.33) with respect to $\epsilon$ and integrating $\eta$ out, one can rewrite (3.32) as

$$\Phi(\tau+\epsilon) = \sum_{n=0}^{\infty} \frac{1}{n!}\epsilon^n \int dxdy \left\{ : \tilde{L}^n : \ \mathcal{O}(z) \right\} P(x,y;\tau) \tag{3.34}$$

where we have defined a differential operator

$$\tilde{L} = \left( \frac{\partial}{\partial z_k} + v_k(z) \right) \frac{\partial}{\partial z_k} \tag{3.35}$$

acting on a holomorphic function of $z_k$, and the symbol $: \cdots :$ implies that the derivatives are moved to the right, i.e., $: (f(x)+\partial)^2 := f(x)^2 + 2f(x)\partial + \partial^2$.

Taking the $\epsilon \to 0$ limit in (3.34), one naively obtains

$$\frac{d}{d\tau}\Phi(\tau) = \int dxdy \{\tilde{L}\mathcal{O}(z)\} P(x,y;\tau) \tag{3.36}$$

and a finite time evolution of $\Phi(\tau)$ as

$$\Phi(\tau+t) = \sum_{n=0}^{\infty} \frac{1}{n!}t^n \int dxdy \left\{ \tilde{L}^n \mathcal{O}(z) \right\} P(x,y;\tau) \ . \tag{3.37}$$

Assuming that (3.37) is valid for finite $t$ at arbitrary $\tau$, one can derive the time evolution of an equivalent system of real variables by induction with respect to $\tau$, from which (3.31) follows.

The expressions such as (3.34) and (3.37) need some care, though. In order for the $\epsilon$-expansion (3.34) to be valid, the integral on the right-hand side should be convergent for all $n$. In order for the expression (3.37) to be valid for finite $t$, the integral on the right-hand side should be convergent for all $n$, and on top of that, the infinite sum over $n$ should have a finite convergence radius, which may depend on $\tau$.

The issues raised above are non-trivial since the drift term $v_k(z)$ in the differential operator (3.35) can become large for some $z = x+iy$, which appears with the probability distribution $P(x,y;\tau)$. Defining the magnitude of the drift term $u(z)$ in a suitable manner, the most dominant contribution from $\tilde{L}^n$ in (3.34) and (3.37) can be estimated as $\tilde{L}^n \sim u(z)^n$. Therefore, the integral appearing in the infinite series can be estimated

as

$$\int dxdy\ u(z)^n\ P(x,y;\tau) = \int_0^\infty du\ u^n p(u;\tau) \tag{3.38}$$

where we have defined the probability distribution of $u(z)$ by

$$p(u;\tau) \equiv \int dxdy\ \delta(u(z)-u)\ P(x,y;\tau) \tag{3.39}$$

In order for (3.36) to be valid, (3.38) should be finite for arbitrary $n$, which requires that $p(u;\tau)$ should fall off faster than any power law. In order for the infinite series (3.37) to have a finite convergence radius, $p(u;\tau)$ should fall off exponentially or faster. Since the latter condition is slightly stronger than the former, it can be regarded as a necessary and sufficient condition for correct convergence in the CLM.

The situation in which the CLM fails can be classified into two cases. One is the case in which the complexified variables make long excursions in the imaginary directions [24, 25], which is called "excursion problem", and the other is the case in which the drift term has singularities and the complexified variables come close to these points frequently [26], which is called " the singular-drift problem".

In both these cases, the magnitude of the drift term tends to become large, and the probability distribution of the drift term can have a power-law behavior at large magnitude. Thus, this criterion can detect these two problems in a unified manner, and more importantly, it enables us to determine precisely the parameter region in which these problems occur. The usefulness of this criterion was demonstrated in [28] for two simple one-variable models, which suffer from the excursion problem and the singular drift problem, respectively, in some parameter region.

## 3.2 Deform the Lorentzian type IIB matrix model

To apply the CLM to the Lorentzian type IIB matrix model, we deform it. Here we introduce two deformation parameters $s$ and $k$, which correspond to Wick rotations on the worldsheet and in the target space, respectively. Let us introduce $\tilde{S} = -iS_{\rm b}$ so that the partition function (2.19) is rewritten as

$$Z = \int dA\ \mathrm{Pf}\,\mathcal{M}(A)\ e^{-\tilde{S}}\ . \tag{3.40}$$

We introduce the first parameter $s$ $(-1 \leq s \leq 1)$ corresponding to the Wick rotation on the worldsheet as

$$S_{\mathrm{b}} \mapsto \mathrm{e}^{is\pi/2} S_{\mathrm{b}} \ . \tag{3.41}$$

In that case, the action is rewritten as

$$\tilde{S} = -iN\beta \mathrm{e}^{is\pi/2} \left\{ -\frac{1}{2} \operatorname{Tr} \left(F_{0i}\right)^2 + \frac{1}{4} \operatorname{Tr} \left(F_{ij}\right)^2 \right\} \ , \tag{3.42}$$

where $\beta = \frac{1}{g^2 N}$. The second parameter $k$ $(0 \leq k \leq 1)$ corresponding to the Wick rotation in the target space can be introduced by the replacement

$$A_0 \mapsto \mathrm{e}^{-ik\pi/2} A_0 \ . \tag{3.43}$$

The action (3.42) becomes

$$\tilde{S} = -iN\beta \mathrm{e}^{is\pi/2} \left\{ -\frac{1}{2} \mathrm{e}^{-ik\pi} \operatorname{Tr} \left(F_{0i}\right)^2 + \frac{1}{4} \operatorname{Tr} \left(F_{ij}\right)^2 \right\} \ , \tag{3.44}$$

and the $\mathrm{Pf}\mathcal{M}\left(A\right)$ in should be replaced by $\mathrm{Pf}\,\mathcal{M}\left(\mathrm{e}^{-ik\pi/2} A_0, A_i\right)$. The Lorentzian model is retrieved at $(s,k) = (0,0)$, whereas the Euclidean model corresponds to setting $(s,k) = (1,1)$.

## 3.3 Apply the CLM to the Lorentzian model

### 3.3.1 Improve treatment of the IR cutoffs

In order to make the partition function finite, we need to take into account the infrared cutoffs as we have seen in Section 2.1.

Let us start with the action (3.44), which reads

$$\tilde{S} = -iN\beta \mathrm{e}^{is\pi/2} \left\{ -\frac{1}{2} \mathrm{e}^{-ik\pi} \operatorname{Tr} \left(F_{0i}\right)^2 + \frac{1}{4} \operatorname{Tr} \left(F_{ij}\right)^2 \right\} \ , \tag{3.45}$$

where we have introduced the Hermitian matrices $F_{\mu\nu} = i\left[A_\mu, A_\nu\right]$. We also have constraints in both the temporal and spatial directions, for instance, as

$$\frac{1}{N}\operatorname{Tr}\left(A_0\right)^2 \leq \kappa L^2 \ , \tag{3.46}$$

$$\frac{1}{N}\operatorname{Tr}\left(A_i\right)^2 \leq L^2 \ , \tag{3.47}$$

which correspond to the IR cutoff. Taking into account the infrared cutoffs, we arrive at the partition function

$$\begin{aligned} Z = \int \prod_{a=1}^{N} d\alpha_a \Delta(\alpha)^2 \int dA_i e^{-\tilde{S}} \operatorname{Pf}\mathcal{M}\left(\mathrm{e}^{-ik\pi/2}A_0, A_i\right) \\ \times \theta\left(\kappa L^2 - \frac{1}{N}\operatorname{Tr}\left(A_0\right)^2\right)\theta\left(L^2 - \frac{1}{N}\operatorname{Tr}\left(A_i\right)^2\right) \end{aligned} \tag{3.48}$$

where $\theta(x)$ is the Heaviside step function. By rescaling $A_\mu \mapsto LA_\mu$ and $\beta \mapsto L^{-4}A_\mu$, we can set $L = 1$ without loss or generality.

In what follows, we omit the Pfaffian to avoid time-consuming. Moreover, including it is not straightforward because the singular-drift problem might occur in the presence of the fermions.

In [12], the constraints (3.46) and (3.47) were treated by the potential

$$V_{\text{pot}} = \frac{1}{p}\gamma_{\text{s}}\left(\frac{1}{N}\operatorname{Tr}\left(A_i\right)^2 - 1\right)^p + \frac{1}{p}\gamma_{\text{t}}\left(\frac{1}{N}\operatorname{Tr}\left(A_0\right)^2 - \kappa\right)^p \ , \tag{3.49}$$

where the power $p$ is set to $p = 4$, and the coefficients $\gamma_{\text{s}}$ and $\gamma_{\text{t}}$ are chosen to be large enough to make $\frac{1}{N}\operatorname{Tr}\left(A_i\right)^2$ and $\frac{1}{N}\operatorname{Tr}\left(A_0\right)^2$ fluctuate around some constants.[1]

This is not very nice because one has to use a huge number for $\gamma_{\text{s}}$ and $\gamma_{\text{t}}$ and the drift term coming from this potential becomes large. In such moments, the results become biased to some extent by the treatment of the constraint.

In what follows we will discuss how one can treat not only (3.46) but also (3.47) without using the potential (3.49). The basic idea is to treat the constraints

$$\frac{1}{N}\operatorname{Tr}\left(A_0\right)^2 = \kappa \ , \tag{3.50}$$

[1] This appears different from imposing the inequalities (3.46) and (3.47), but the difference is not important since the inequalities are typically saturated due to entropic effects.

and

$$\frac{1}{N}\,\mathrm{Tr}\,(A_i)^2 = 1\ , \tag{3.51}$$

by rescaling $A_0$ and $A_i$ instead of constraining them by some strong potential, which mimics the delta funtion as we also implemented it in Monte Carlo studies of Chapter 2.

This new treatment makes the drift term much smaller than the previous work [12] , which allows us to use much larger Langevin stepsize. The magnitude is typically smaller by a factor of ten or more. As a consequence, we are able to perform stable simulations even with large Langevin stepsize such as $\epsilon = 10^{-5}$ and most importantly the constraints are treated exactly; i.e., there is no need for extrapolations such as $\gamma_{\mathrm{s}} \to \infty$, $\gamma_{\mathrm{t}} \to \infty$ in the case of using the potential (3.49). The results of this treatment suggest that the basic conclusion does not change dramatically, but the minor details are quite different. This new treatment enables us to investigate much larger range of $(s, k)$, and then approach our target values $(s, k) = (0, 0)$.

Let us denote the matrices satisfying the constraints (3.50) and (3.51) as $X_0$ and $X_i$, as

$$\frac{1}{N}\,\mathrm{Tr}\,(X_0)^2 = \kappa\ , \tag{3.52}$$

and

$$\frac{1}{N}\,\mathrm{Tr}\,(X_i)^2 = 1\ . \tag{3.53}$$

The partition function before "gauge fixing" reads

$$Z = \int dX\ e^{-\tilde{S}(X)}\delta\left(\frac{1}{N}\,\mathrm{Tr}\,(X_0)^2 - \kappa\right)\delta\left(\frac{1}{N}\,\mathrm{Tr}\,(X_i)^2 - 1\right)\ , \tag{3.54}$$

where $\tilde{S}(X)$ is given by

$$\tilde{S}(X) = -iN\beta \mathrm{e}^{is\pi/2}\left\{-\frac{1}{2}\mathrm{e}^{-ik\pi}\,\mathrm{Tr}\,(F_{0i})^2 + \frac{1}{4}\,\mathrm{Tr}\,(F_{ij})^2\right\}\ , \tag{3.55}$$

where we introduce the Hermitian matrices $F_{\mu\nu} = i\left[X_\mu, X_\nu\right]$.

Then, we introduce auxiliary variables $u, v \geq 0$ into the system and rewrite (3.54) as

$$Z = \int_0^\infty du dv \int dX \; u^p v^q e^{-f(u)} e^{-g(v)} e^{-\tilde{S}(X)} \delta\left(\frac{1}{N}\mathrm{Tr}\,(X_0)^2 - \kappa\right) \delta\left(\frac{1}{N}\mathrm{Tr}\,(X_i)^2 - 1\right) \tag{3.56}$$

where $p$ and $q$ are some positive constants and $f(u)$ and $g(v)$ are some functions to be chosen arbitrarily as far as the integration over $u$ and $v$ converges. Then we make a change of variables

$$A_0 = \sqrt{\frac{u}{\kappa}} X_0, \quad A_i = \sqrt{v} X_i \tag{3.57}$$

under which the measure and the delta functions transform as

$$dA = \left(\frac{u}{\kappa}\right)^{\frac{1}{2}N^2} v^{\frac{1}{2}(D-1)N^2} dX \;, \tag{3.58}$$

$$\delta\left(\frac{1}{N}\mathrm{Tr}\,(X_0)^2 - \kappa\right) = \frac{u}{\kappa}\delta\left(\frac{1}{N}\mathrm{Tr}\,(A_0)^2 - u\right) \;, \tag{3.59}$$

$$\delta\left(\frac{1}{N}\mathrm{Tr}\,(X_i)^2 - 1\right) = v\delta\left(\frac{1}{N}\mathrm{Tr}\,(A_i)^2 - v\right) \;. \tag{3.60}$$

Therefore, by choosing $p = \frac{1}{2}N^2 - 1$ and $q = \frac{1}{2}(D-1)N^2 - 1$, we obtain

$$\begin{aligned} Z = \int du \; dv \; dA \; e^{-f(u)} e^{-g(v)} e^{-\tilde{S}\left(A_0\sqrt{\kappa/u},\; A_i/\sqrt{v}\right)} \\ \delta\left(\frac{1}{N}\mathrm{Tr}\,(A_0)^2 - u\right) \delta\left(\frac{1}{N}\mathrm{Tr}\,(A_i)^2 - v\right) \;, \end{aligned} \tag{3.61}$$

neglecting an irrelevant overall factor. Integrating out $u$ and $v$, we arrive at

$$Z = \int dA \; e^{-S_{\mathrm{new}}} \;, \tag{3.62}$$

where the action $S_{\text{new}}$ is given by

$$\begin{aligned} S_{\text{new}} =& \tilde{S}\left(\frac{\sqrt{\kappa}A_0}{\sqrt{\frac{1}{N}\operatorname{Tr}(A_0)^2}}, \frac{A_i}{\sqrt{\frac{1}{N}\operatorname{Tr}(A_i)^2}}\right) + f\left(\frac{1}{N}\operatorname{Tr}(A_0)^2\right) + g\left(\frac{1}{N}\operatorname{Tr}(A_i)^2\right) \\ =& -iN\beta^{is\pi/2}\left\{-\frac{1}{2}\mathrm{e}^{-ik\pi}\frac{\operatorname{Tr}(F_{0i})^2}{\frac{1}{N}\operatorname{Tr}(A_0)^2\,\frac{1}{N}\operatorname{Tr}(A_i)^2} + \frac{1}{4}\frac{\operatorname{Tr}(F_{ij})^2}{\left(\frac{1}{N}\operatorname{Tr}(A_i)^2\right)^2}\right\} \\ &+ f\left(\frac{1}{N}\operatorname{Tr}(A_0)^2\right) + g\left(\frac{1}{N}\operatorname{Tr}(A_i)^2\right) \end{aligned} \tag{3.63}$$

Thus the original system is rewritten in terms of the unconstrained variables $A_0$ and $A_i$, and all we have to do is to rescale them in such a way that the constraints (3.52) and (3.53) are satisfied before measuring observables. The first term in (3.63) is invariant under rescaling $A_0$ and $A_i$ separately. The expectation values of $\frac{1}{N}\operatorname{Tr}(A_0)^2$ and $\frac{1}{N}\operatorname{Tr}(A_i)^2$ are determined completely by the functions $f(u)$ and $g(v)$ as one can see from (3.56). Below we choose them to be $f(x) = g(x) = \frac{1}{2}N^2x$, which corresponds to canonical Gaussian terms with respect to $A_0$ and $A_i$. In that case, we obtain

$$\left\langle \frac{1}{N}\operatorname{Tr}(A_0)^2 \right\rangle = 1 \tag{3.64}$$

$$\left\langle \frac{1}{N}\operatorname{Tr}(A_i)^2 \right\rangle = D-1 \tag{3.65}$$

These results can be used to test the validity of the Complex Langevin method. Also they can be used to estimate the systematic errors due to finite Langevin stepsize.[2]

### 3.3.2 How to introduce the time ordering

The new system (3.63) can be investigated by the Complex Langevin method. The first step of the CLM is to complexify the real variables. As for the spatial matrices $A_i$, we simply treat them as general complex matrices instead of Hermitian matrices. As for the temporal matrix $A_0$, we can use the SU($N$) symmetry of the model to bring the temporal matrix $A_0$ into the diagonal form

$$A_0 = \operatorname{diag}(\alpha_1, \ldots, \alpha_N), \qquad \text{where } \alpha_1 < \cdots < \alpha_N . \tag{3.66}$$

[2]The error is found to be proportional to the stepsize $\epsilon$. This situation can be improved by using the second-order Runge-Kutta algorithm.

By "fixing the gauge" in this way, we can rewrite the partition function (3.62) as

$$Z = \int \prod_{a=1}^{N} d\alpha_a \, \Delta(\alpha)^2 \int dA_i \, e^{-S_{\text{new}}} \,, \tag{3.67}$$

$$\Delta(\alpha) \equiv \prod_{a>b}^{N} (\alpha_a - \alpha_b) \,, \tag{3.68}$$

where $\Delta(\alpha)$ is the van der Monde determinant. We have to take into account the ordering of the eigenvalues. For that purpose, we make the change of variables as

$$\alpha_1 = 0, \quad \alpha_2 = \mathrm{e}^{\tau_1}, \quad \alpha_3 = \mathrm{e}^{\tau_1} + \mathrm{e}^{\tau_2}, \quad \cdots, \quad \alpha_N = \sum_{a=1}^{N-1} \mathrm{e}^{\tau_a} \,, \tag{3.69}$$

so that the ordering (3.66) is implemented automatically, and then complexify $\tau_a (a = , \dots, N-1)$. We have chosen to set $\alpha_1 = 0$ using the shift symmetry $A_0 \mapsto A_0 + \text{const.}\mathbf{1}$ of the action. In order to respect this symmetry, we decide to impose the cutoff like (3.52) only on the traceless part $\tilde{A}_0 \equiv A_0 - \frac{1}{N} \operatorname{Tr} A_0$. We can easily generalize the argument given above to this case, and the effective action reads

$$\begin{aligned} S_{\text{eff}} = N\beta e^{-i\frac{\pi}{2}(1-s)} \left\{ \frac{1}{2} e^{-ik\pi} \frac{\kappa \operatorname{Tr}\left[\tilde{A}_0, A_i\right]^2}{\frac{1}{N}\operatorname{Tr}\left(\tilde{A}_0\right)^2 \frac{1}{N}\operatorname{Tr}\left(A_i\right)^2} - \frac{1}{4} \frac{\operatorname{Tr}\left[A_i, A_j\right]^2}{\left(\frac{1}{N}\operatorname{Tr}\left(A_i\right)^2\right)^2} \right\} \\ + \frac{1}{2} N \operatorname{Tr}\left(\tilde{A}_0\right)^2 + \frac{1}{2} N \operatorname{Tr}\left(A_i\right)^2 - 2 \log \Delta(\alpha) - \sum_{a=1}^{N-1} \tau_a \,, \end{aligned} \tag{3.70}$$

where the last term comes from the Jacobian associated with the change of variables (3.69). The prediction (3.64) is replaced by

$$\left\langle \frac{1}{N} \operatorname{Tr}\left(\tilde{A}_0\right)^2 \right\rangle = 1 - \frac{1}{N^2} \,, \tag{3.71}$$

due to the absence of the trace part.

### 3.3.3 Complex Langevin equation of this model

The Complex Langevin equation is given by

$$\frac{d\tau_a}{dt} = -\frac{\partial S_{\text{eff}}}{\partial \tau_a} + \eta_a(t)\,, \tag{3.72}$$

$$\frac{d\left(A_i\right)_{ab}}{dt} = -\frac{\partial S_{\text{eff}}}{\partial \left(A_i\right)_{ba}} + \left(\eta_i\right)_{ab}(t)\,, \tag{3.73}$$

where the $\eta_a(t)$ in the first equation are random real numbers obeying the probability distribution $\exp\left(-\frac{1}{4}\int dt \sum_a \left\{\eta_a(t)\right\}^2\right)$ and the $\eta_i(t)$ in the second equation are random Hermitian matrices obeying the probability distributions $\exp\left(-\frac{1}{4}\int dt \sum_i \mathrm{Tr}\left\{\eta_i(t)\right\}^2\right)$.

These drift terms are given explicitly as

$$\begin{aligned}
\frac{\partial S_{\text{eff}}}{\partial \tau_a} =& \beta e^{-i\frac{\pi}{2}(1-s)} e^{-ik\pi}\frac{\kappa}{L} e^{\tau_a} \\
&\left\{ -\frac{2N}{K}\sum_{b=a+1}^{N}\sum_{c\neq b}\left(\alpha_b-\alpha_c\right)\left(A_i\right)_{bc}\left(A_i\right)_{cb} \right. \\
&\left. +\frac{1}{K^2}\sum_{b=a+1}^{N}\left(\alpha_b-\frac{1}{N}\sum_c\alpha_c\right)\sum_{de}\left(\alpha_d-\alpha_e\right)^2\left(A_i\right)_{de}\left(A_i\right)_{ed} \right\} \\
&-e^{\tau_a}\sum_{b=a+1}^{N}\sum_{c\neq b}\frac{2}{\alpha_b-\alpha_c} - 1 + Ne^{\tau_a}\sum_{b=a+1}^{N}\left(\alpha_b-\frac{1}{N}\sum_c\alpha_c\right)\,,
\end{aligned} \tag{3.74}$$

$$\begin{aligned}
\frac{\partial S_{\text{eff}}}{\partial \left(A_i\right)_{ba}} =& -\beta e^{-i\frac{\pi}{2}(1-s)} e^{-ik\pi}\frac{\kappa}{K} \\
&\left\{ \frac{N}{L}\left[A_0,\left[A_0,A_i\right]\right]_{ab} + \frac{\mathrm{Tr}\left[A_0,A_j\right]^2}{L^2}\left(A_i\right)_{ab} \right\} \\
&+\beta e^{-i\frac{\pi}{2}(1-s)}\left\{ \frac{N\left[A_j,\left[A_j,A_i\right]\right]_{ab}}{L^2} + \frac{\mathrm{Tr}\left[A_j,A_k\right]^2}{L^3}\left(A_i\right)_{ab} \right\} + N\left(A_i\right)_{ab}\,,
\end{aligned} \tag{3.75}$$

where we define

$$K \equiv \frac{1}{N}\mathrm{Tr}\left(\tilde{A}_0\right)^2 = \frac{1}{N}\sum_a^N\left(\alpha_a\right)^2 - \left(\frac{1}{N}\sum_a^N\alpha_a\right)^2 \tag{3.76}$$

$$L \equiv \frac{1}{N} \mathrm{Tr}\,(A_i)^2 \tag{3.77}$$

In our algorism, we also implement the peak stabilizing potential introduced in [10]. This concerns the spontaneous breaking of the shift symmetry $A_0 \mapsto A_0 + \alpha \mathbf{1}$. For instance, let us consider calculating the expectation value $R^2(t)$. The peak of this quantity measured for each configuration fluctuates considerably. This reflects the ambiguity in choosing the origin of the time coordinate, and we should fix it before taking the ensemble average. Here we fix it by introducing a potential

$$V = \frac{1}{2}\gamma_{\mathrm{v}} \frac{\Xi^2}{\left(\frac{1}{N}\mathrm{Tr}\,(A_i)^2\right)^2}\,, \tag{3.78}$$

$$\Xi = \frac{1}{N}\left[\mathrm{Tr}\,(A_i)^2\right]_{\mathrm{L}} - \frac{1}{N}\left[\mathrm{Tr}\,(A_i)^2\right]_{\mathrm{R}}\,, \tag{3.79}$$

$$\left[\mathrm{Tr}\,(A_i)^2\right]_{\mathrm{L}} = \sum_{i=1}^{D-1} \sum_{a+b<N+1} (A_i)_{ab} (A_i)_{ba}\,, \tag{3.80}$$

$$\left[\mathrm{Tr}\,(A_i)^2\right]_{\mathrm{R}} = \sum_{i=1}^{D-1} \sum_{a+b>N+1} (A_i)_{ab} (A_i)_{ba}\,, \tag{3.81}$$

where the values of the coefficient $\gamma_{\mathrm{V}}$ should be chosen large enough to stabilize the peak, but too large values may cause systematic errors. The appropriate value depends on the parameters.

Taking this potential into account, the drift term (3.75) for $(A_i)_{ab}$ have additional terms

$$\frac{\partial V}{\partial (A_i)_{ba}} = \pm \frac{2\gamma_{\mathrm{v}}}{NL^2} \Xi (A_i)_{ab} - \frac{2\gamma_{\mathrm{v}}}{NL^3} \Xi^2 (A_i)_{ab} \tag{3.82}$$

where the symbol $\pm$ implies that $+$ and $-$ should be chosen for $i+j < N+1$ and $i+j > N+1$, respectively.

The expectation values of observables can be calculated by defining them holomorphically for complexified $\tau_a$ and $A_i$ and taking an average using the configurations generated by solving the discretized version of (3.72), (3.73) for sufficiently long time. In order for

this method to work, the probability distribution of the drift terms, namely the first terms on the right-hand side of (3.72), (3.73), has to fall off exponentially [28]. We must check that this criterion is satisfied for all the values of parameters used.

## 3.4 Emergence of (3+1)D expanding behavior

In this section, we mainly discuss the spontaneous symmetry breaking and investigate the space-time structure of the matrix configurations generated by the Complex Langevin simulation of the model (3.70). In what follows, we focus on (5+1)D bosonic model to avoid time-consuming.

### 3.4.1 $(s, k) = (-1, 0)$ corresponding to the approximate model in Monte Carlo simulations

First, we focus on $(s, k) = (-1, 0)$ in the deformation parameter space, where we do not have the sign problem. As we see below, this case corresponds to the approximate model investigated in our Monte Carlo studies. In fact, we here observe the emergence of (3+1)D expanding space-time with the Pauli-matrix structure.

Here we consider $(s, k) = (-1, 0)$ in the parameter space. The action (3.55) becomes

$$\tilde{S} = -N\beta \left\{ -\frac{1}{2} \operatorname{Tr} \left(F_{0i}\right)^2 + \frac{1}{4} \operatorname{Tr} \left(F_{ij}\right)^2 \right\} \tag{3.83}$$

$$= -N\beta \left\{ \frac{1}{2} \operatorname{Tr} \left[X_0, X_i\right]^2 - \frac{1}{4} \operatorname{Tr} \left[X_i, X_j\right]^2 \right\} , \tag{3.84}$$

which is real, and the CLM reduces to the ordinary Langevin method. The first term in (3.84) tries to minimize the space-time noncommutativity, which has the effects of making the spatial matrices close to diagonal in the basis (3.66). On the other hand, the second term favors maximal noncommutativity among spatial matrices.

We can extract a time-evolution from configurations generated by simulating (3.67). In the basis that makes $X_0$ diagonal, the spatial matrices $X_i$ are not diagonal in general, but they actually turn out to be band-diagonal. In order to see it, we plot

$$Q_{IJ}^{sq} = \sum_{i=1}^{D-1=5} \left| \left(X_i\right)_{IJ} \right|^2 \tag{3.85}$$

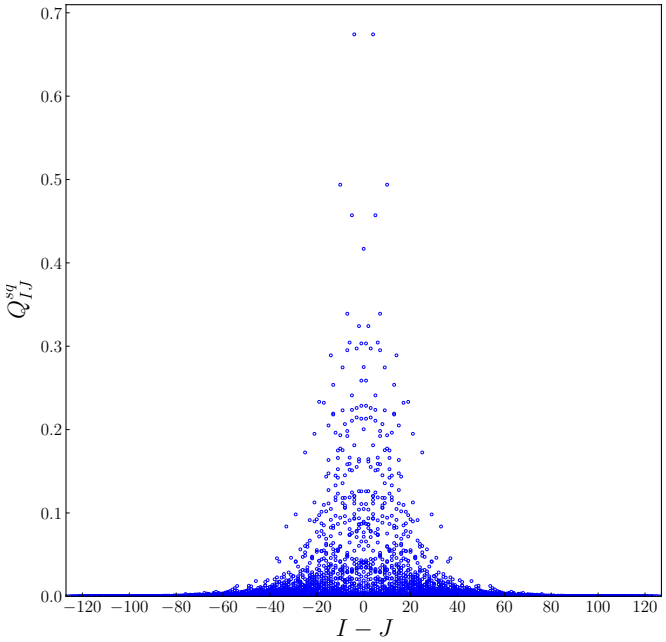


**Figure 3.1:** The quantity $Q^{sq}_{IJ}$ defined by (3.85) is plotted against the labels $I$ and $J$ for the typical configuration with (5+1)D, $N = 128$, $(s, k) = (-1, 0)$, $\kappa = 0.02$, $\beta = 8.0$.

in Figure 3.1.

We find that $Q^{sq}_{IJ}$ becomes very small for $|I - J| > n$ with some integer $n$, which is $n \sim 18$ in Figure 3.1. The band-diagonal structure guarantees the locality of time, which enables us to extract the time evolution. This features are actually shared also by the dominant configurations generated by previous Monte Carlo studies.

Based on this observation, we may naturally consider $n \times n$ submatrices of $X_i$ defined as

$$\left(\bar{X}_i\right)_{rs}(t) \equiv \left(X_i\right)_{\nu+r,\nu+s} \tag{3.86}$$

where $r, s = 1, \ldots, n, \nu = 0, 1, \ldots, N-n$, and the argument $t$ represents the "time" defined by

$$t = \frac{1}{n}\sum_{r=1}^{n} \alpha_{\nu+r} \ , \tag{3.87}$$

which has two components, its real part and its imaginary part, and can thus be plotted in the complex plane, where we find that its imaginary part is very small compared to

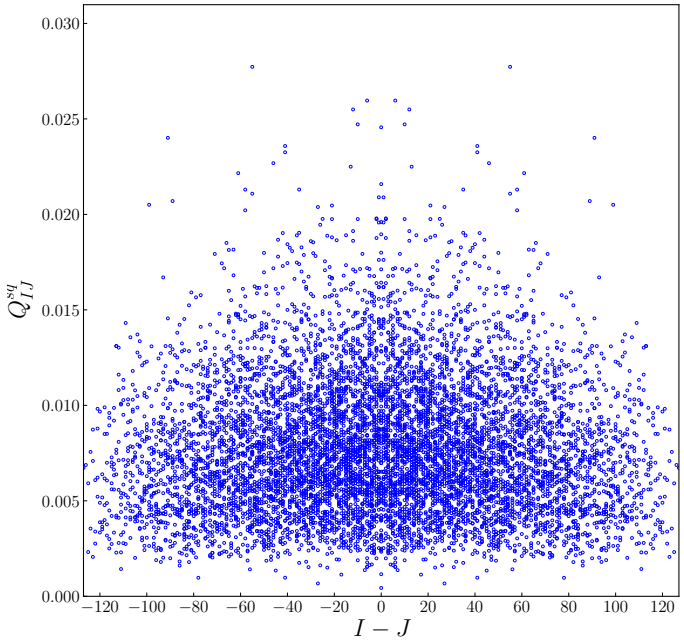


**Figure 3.2:** The quantity $Q_{IJ}^{sq}$ defined by (3.85) is plotted against the labels $I$ and $J$ for the typical configuration with (5+1)D, $N = 128$, $(s, k) = (1, 1)$, $\kappa = 0.02$, $\beta = 8.0$.

its real part. Therefore, we can neglect its imaginary part. Here we interpret the $\bar{X}_i(t)$ as representing the space structure at time $t$.

This feature is not observed at $(s, k) = (1, 1)$, which corresponds to the Euclidean model, where the action is given by

$$\tilde{S} = N\beta \left\{ \frac{1}{2} \operatorname{Tr} (F_{0i})^2 + \frac{1}{4} \operatorname{Tr} \left(F_{ij}\right)^2 \right\} \tag{3.88}$$

$$= -N\beta \left\{ \frac{1}{2} \operatorname{Tr} [X_0, X_i]^2 + \frac{1}{4} \operatorname{Tr} \left[X_i, X_j\right]^2 \right\} \ . \tag{3.89}$$

Its quantity $Q_{IJ}^{sq}$ is plotted in Figure 3.2. The spatial matrices $X_i$ do not have a band-diagonal structure, which causes a loss of ability to extraction of the real-time evolution. Hence it implies that its Euclidean model is not suitable for studying the real-time dynamics.

For instance, we define the extent of space at $t$ by

$$R^2(t) = \left\langle \frac{1}{n} \operatorname{tr} \sum_i \left(\bar{X}_i(t)\right)^2 \right\rangle \tag{3.90}$$

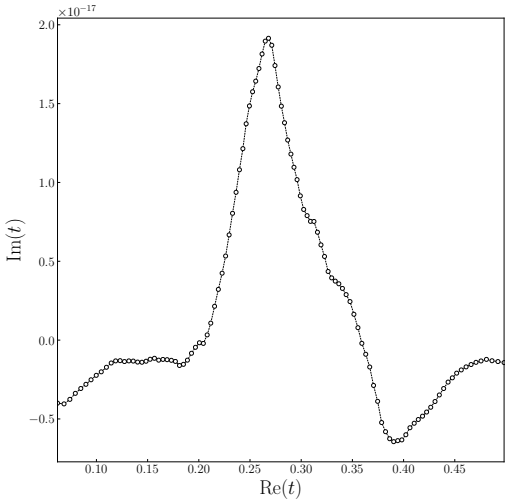


**Figure 3.3:** The time $t$ defined by (3.87) is plotted in the complex plane for the typical configuration with (5+1)D, $N = 128$, $(s, k) = (-1, 0)$, $\kappa = 0.02$, $\beta = 8.0$, $n = 18$, where the $x$-coordinate refers to the real part and the $y$-coordinate refers to the imaginary part of the time $t$.

where the symbol "tr" represents a trace over the $n \times n$ submatrix. In Figure 3.4, we plot the real and imaginary parts of $R^2(t)$ for the typical configuration. We find that $R^2(t)$ is dominated only by the real part and roughly symmetric under the reflection $t - t_{\mathrm{p}} \mapsto -\big(t - t_{\mathrm{p}}\big)$, where $t_p$ represents the time at which $R^2(t)$ is peaked, reflecting the symmetry of the model under $X_0 \mapsto -X_0$.

Let us also take a look at the "Hermiticity norm" for $\bar{X}_i(t)$ defined by

$$h(t) = \frac{-\operatorname{tr}\left(\bar{X}_i(t) - \bar{X}_i(t)^\dagger\right)^2}{4\operatorname{tr}\left(\bar{X}_i(t)^\dagger \bar{X}_i(t)\right)} \tag{3.91}$$

using the configuration generated by the simulation. The result is plotted in Figure 3.4 as well. Note that $h(t) = 0$ implies that the matrices $\bar{X}_i(t)$ are all Hermitian, while $h(t) = 1$ implies that they are all anti-Hermitian. We understand that $h(t)$ is zero and hence the $\bar{X}_i(t)$ are very close to Hermitian, which is consistent with our Monte Carlo studies.

Next we discuss the SSB of SO(5) symmetry by considering the "moment of inertia tensor". We define a $5 \times 5$ real symmetric tensor

$$T_{ij}(t) = \frac{1}{n}\operatorname{tr}\left(\bar{X}_i(t)\bar{X}_j(t)\right) \ , \tag{3.92}$$

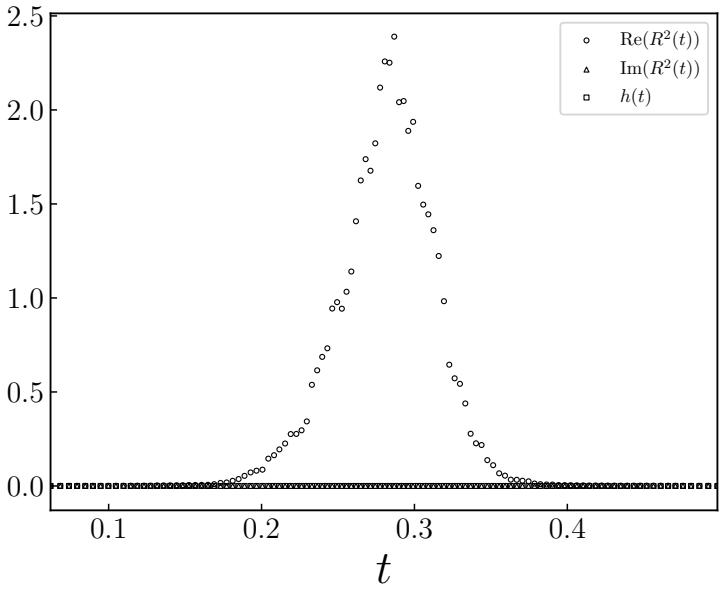


**Figure 3.4:** Results for (5+1)D, $N = 128$, $(s, k) = (-1, 0)$, $\kappa = 0.02$, $\beta = 8.0$, $n = 18$ are shown. The real and imaginary parts of $R^2(t)$ are plotted against $t$. The Hermiticity norm $h(t)$ of the matrix $\bar{X}_i(t)$ is also plotted.

whose eigenvalues $\lambda_i(t)$, which we order as

$$\lambda_1(t) > \lambda_2(t) > \cdots > \lambda_5(t) \ , \tag{3.93}$$

represent the spatial extent in each of the nine directions at time $t$. These eigenvalues are related to the extent of space $R^2(t)$ as

$$R^2(t) = \left\langle \sum_{i=1}^{5} \lambda_i(t) \right\rangle \ . \tag{3.94}$$

In general, $\bar{X}_i(t)$ are not Hermitian as we will see in Section 3.5. Thus, when we see its eigenvalues, we define Hermitian matrices as

$$\bar{Y}_i(t) = \frac{1}{2} \left( \bar{X}_i(t) + \bar{X}_i(t)^\dagger \right) \ . \tag{3.95}$$

In Figure 3.5, we plot the eigenvalues $\lambda_i(t)$ of

$$T_{ij}(t) = \frac{1}{n} \operatorname{tr} \left( \bar{Y}_i(t) \bar{Y}_j(t) \right) \ , \tag{3.96}$$

which shows that only three out of five eigenvalues become large in the time region around $t = t_{\mathrm{p}}$.

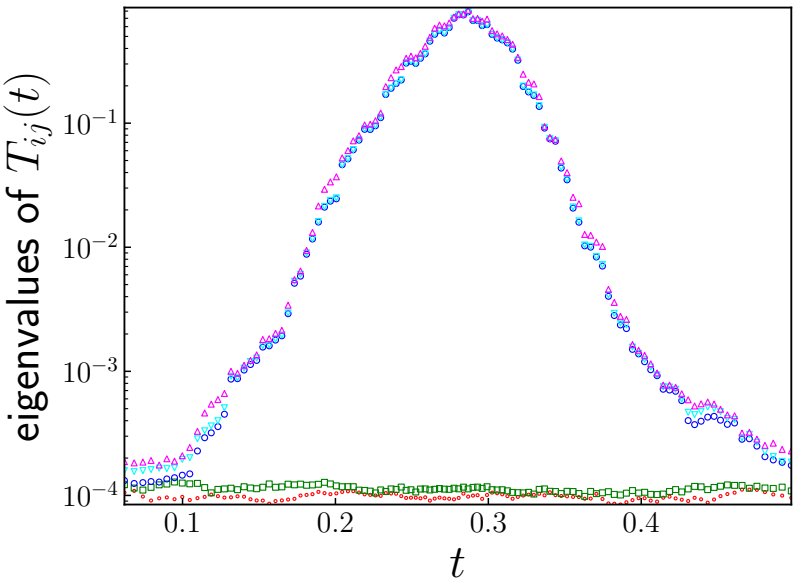


**Figure 3.5:** Results for (5+1)D, $N = 128$, $(s, k) = (-1, 0)$, $\kappa = 0.02$, $\beta = 8.0$, $n = 18$ are shown. The five eigenvalues of the moment of inertia tensor are plotted against $t$ in the log scale.

This result suggests that the rotational SO(5) symmetry of the (5+1)D bosonic model is spontaneously broken down to SO(3) in that time region. These results are qualitatively the same as what has been obtained in Monte Carlo studies of the model, which is consistent with the speculation that the previous simulations correspond to the parameter choice $(s, k) = (-1, 0)$. Note that $\lambda_i(t)$ tend to be equal in the large-$N$ limit when the SO(5) symmetry is not spontaneously broken.

As is known from the previous work, the time difference between the peak ($t = t_{\rm p}$) and the critical time at which the SSB occurs increases in physical units as we take the large-$N$ limit. Therefore, the reflection symmetry with respect to $t$ does not necessarily imply that the Big Crunch occurs in the finite future.

As we mentioned in Section 2.4.2, the mechanism of this SSB can be understood as follows. Since the first term in (3.84) favors $X_i$ close to diagonal, we may consider the submatrices $\bar{X}_i(t)$ as the effective degrees of freedom. The infrared cutoff (3.53) fixes $\mathrm{Tr}\{\bar{X}_i(t)\}^2$ to some constant, and the second term in (3.84) favors maximal noncommutativity between $\bar{X}_i(t)$. According to the argument in [6] as well as Section 2.4.2, this leads to $\bar{X}_i(t) \propto \sigma_i \oplus \mathbf{0}_{n-2}$ for $i = 1, 2, 3$ and $\bar{X}_i(t) = \mathbf{0}_n$ for $i \geq 4$ up to SO(5) rotations, where $\sigma_i$ are the Pauli matrices.

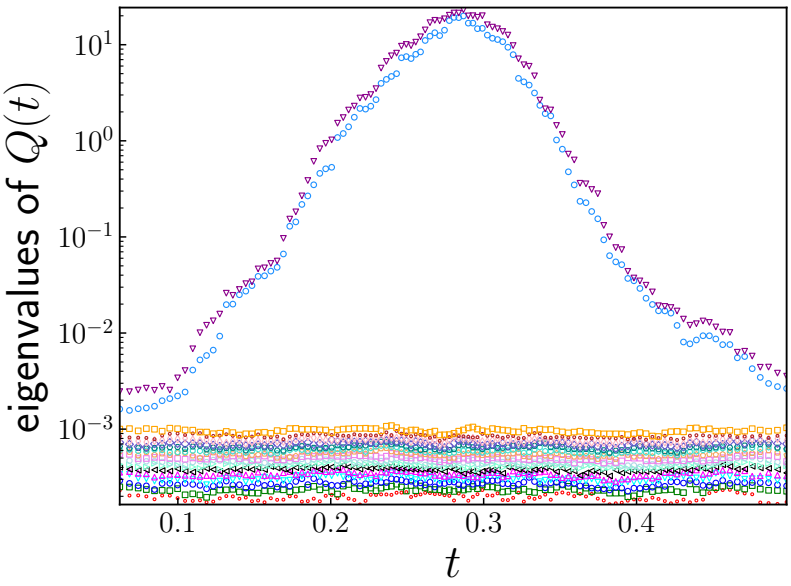


**Figure 3.6:** Results for (5+1)D, $N = 128$, $(s, k) = (-1, 0)$, $\kappa = 0.02$, $\beta = 8.0$, $n = 18$ are shown. The eigenvalues of the matrix $Q(t)$ are plotted against $t$ in the log scale.

In order to confirm this mechanism, we probe the structure of the space, calculating the $n \times n$ matrix

$$Q(t) = \sum_{i=1}^{5} \left\{ \bar{Y}_i(t) \right\}^2 \tag{3.97}$$

and plot the eigenvalues $q_r(t)$ of $Q(t)$ in Figure 3.6. These eigenvalues represent the radial distribution of the points which describe the 5-dimensional space. Note that the eigenvalues $q_r(t)$ are related to the extent of space $R^2(t)$ as

$$R^2(t) = \left\langle \frac{1}{n} \mathrm{tr} Q(t) \right\rangle = \left\langle \frac{1}{n} \sum_{r=1}^{n} q_r(t) \right\rangle \ . \tag{3.98}$$

Indeed we find that only two of them are large, while the rest are very small in the time region in which the SSB occurs.

### 3.4.2 On the line $k = (1 + s)/2$

Next we tune the worldsheet deformation parameter $s$ close to that for the Lorentzian model ($s = 0$) keeping the target space deformation parameter $k$ in such a way that the space-time noncommutativity is minimized.

In the (3.55), the coefficient of the first term in

$$\tilde{S} = -iN\beta \mathrm{e}^{is\pi/2} \left\{ -\frac{1}{2} \mathrm{e}^{-ik\pi} \operatorname{Tr} \left(F_{0i}\right)^2 + \frac{1}{4} \operatorname{Tr} \left(F_{ij}\right)^2 \right\} \tag{3.99}$$

can be made real positive by choosing the parameters so that

$$ie^{is\frac{\pi}{2}} e^{-ik\pi} = 1 \ , \tag{3.100}$$

which implies

$$k = \frac{1+s}{2} \ . \tag{3.101}$$

For this choice, the bosonic action is most effective in minimizing the noncommutativity between the spatial matrices $X_i$ and the temporal matrix $X_0$. Thus, the action reads

$$\tilde{S} = -N\beta \left\{ -\frac{1}{2} \operatorname{Tr} \left(F_{0i}\right)^2 - \mathrm{e}^{-i\frac{\pi}{2}(1-s)} \frac{1}{4} \operatorname{Tr} \left(F_{ij}\right)^2 \right\} \tag{3.102}$$

$$= -N\beta \left\{ \frac{1}{2} \operatorname{Tr} \left[X_0, X_i\right]^2 + \mathrm{e}^{-i\frac{\pi}{2}(1-s)} \frac{1}{4} \operatorname{Tr} \left[X_i, X_j\right]^2 \right\} \ . \tag{3.103}$$

The only difference from (3.84) is the second term with the coefficient $\mathrm{e}^{-i\frac{\pi}{2}(1-s)}$ whose real part changes its sign at $s = 0$. Specifically, if $s < 0$, we have the real part $< 0$, or if $s > 0$, we have the real part $> 0$. This implies, in particular, that for $s < 0$ the second term maximizes the noncommutativity among the spatial matrices. Therefore, we will experience a drastic change of the behavior around $s = 0$.

Unlike the $(s, k) = (-1, 0)$ case, the action becomes complex for $s > -1$ in general. Therefore, the time $t$ defined by (3.87) is not guaranteed to be real. However, it turns out to be close to real for the configurations generated by the Complex Langevin method in Figure 3.7 for (5+1)D, $N = 128$, $\kappa = 0.02$, $\beta = 8.0$, $n = 18$ with $(s, k) = (-0.5, 0.25)$(Left) and $(s, k) = (-0.05, 0.475)$(Right). Its integer $n$ can also be determined by observing (3.85). We therefore neglect the small imaginary part of $t$ in making the plots in analogy with the $(s, k) = (-1, 0)$ case.

Similarly, the quantity such as $R^2(t)$ defined in (3.90) is not guaranteed to be real positive. In Figure 3.8 we plot the real and imaginary parts of $R^2(t)$. Here we evaluate $R^2(t)$ by calculating $\frac{1}{n}\mathrm{tr} \sum_i \left(\bar{X}_i\left(t\right)\right)^2$ for one complex $\bar{X}_i(t)$ obtained from configurations generated by the Complex Langevin simulation without taking the Hermitian part. We find that $R^2(t)$ is dominated by the real part near the peak. Next we take a look at the

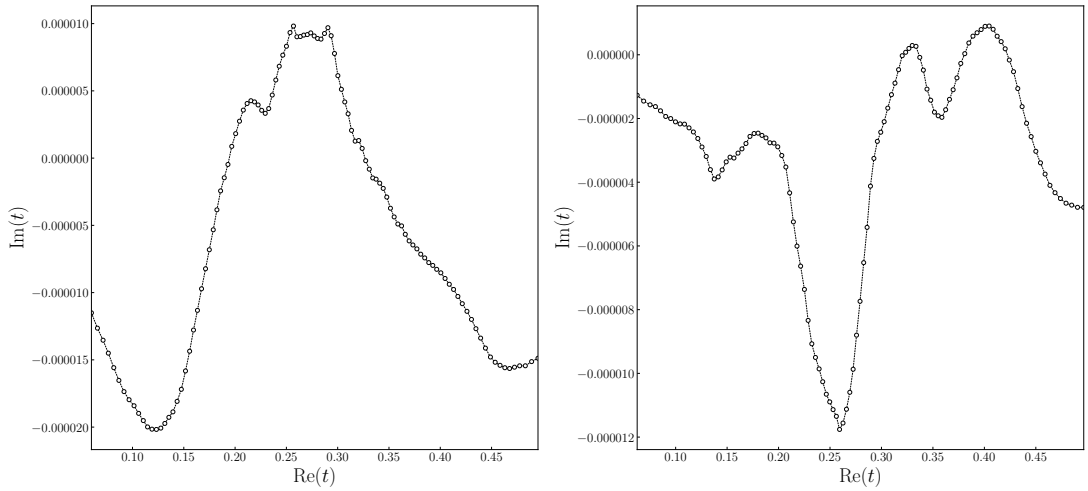


**Figure 3.7:** The time $t$ defined by (3.87) is plotted in the complex plane for the typical configuration with (5+1)D, $N = 128$, $\kappa = 0.02$, $\beta = 8.0$ and the block size $n = 18$, where the $x$-coordinate refers to the real part and the $y$-coordinate refers to the imaginary part of the time $t$. Left is plotted with $(s, k) = (-0.5, 0.25)$ and Right is plotted with $(s, k) = (-0.05, 0.475)$.

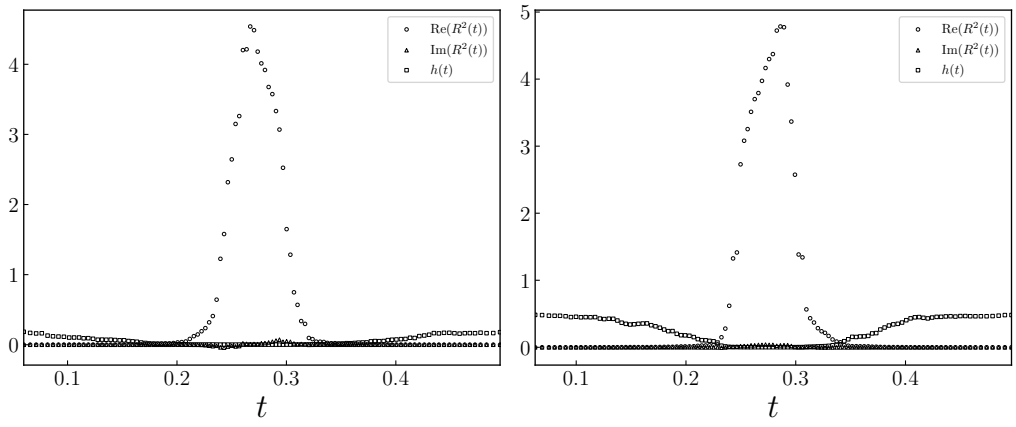


**Figure 3.8:** Results for (5+1)D, $N = 128$, $\kappa = 0.02$, $\beta = 8.0$ and the block size $n = 18$ are shown. The real and imaginary parts of $R^2(t)$ are plotted against $t$. The Hermiticity norm $h(t)$ of the matrix $\bar{X}_i(t)$ is also plotted. Left is plotted with $(s, k) = (-0.5, 0.25)$ and Right is plotted with $(s, k) = (-0.05, 0.475)$.

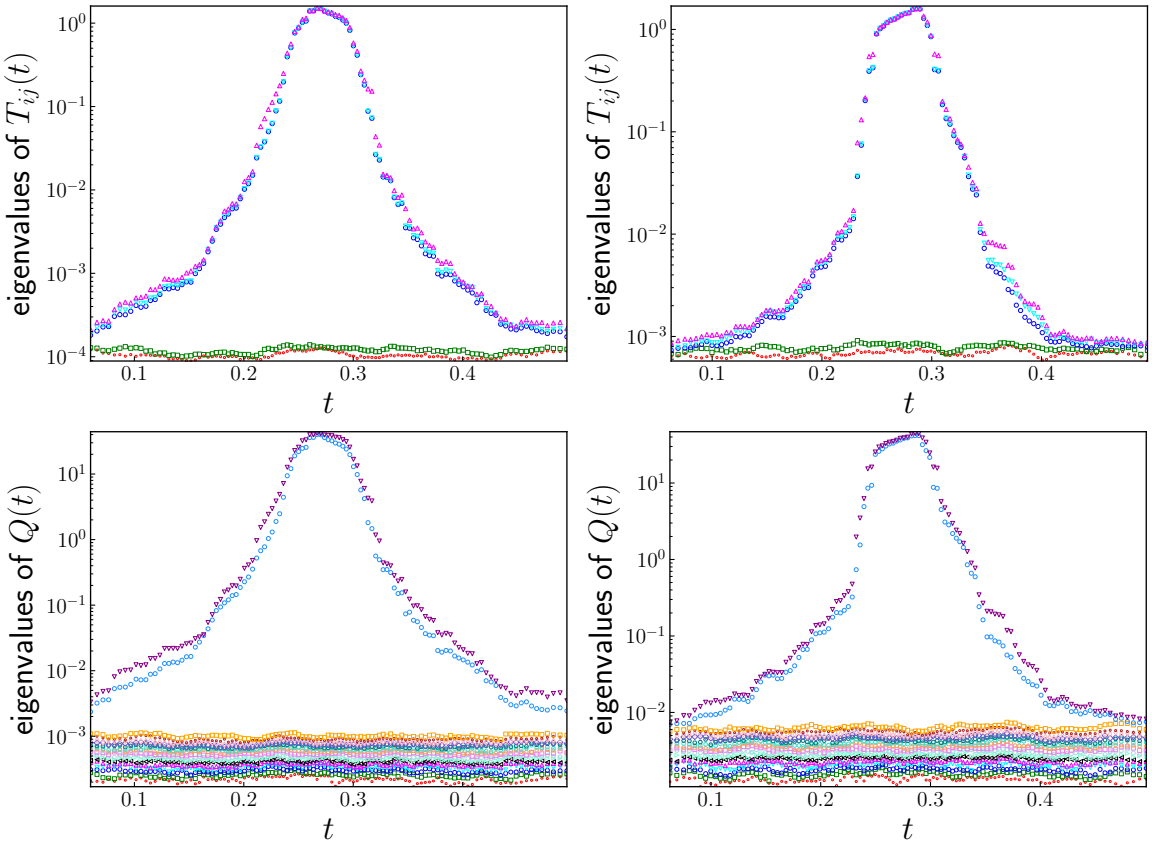


**Figure 3.9:** Results for (5+1)D, $N = 128$, $\kappa = 0.02$, $\beta = 8.0$ and the block size $n = 18$ are shown. (Top)The five eigenvalues of the moment of inertia tensor are plotted against $t$ in the log scale. (Bottom)The eigenvalues of the matrix $Q(t)$ are plotted against $t$ in the log scale. Left is plotted with $(s, k) = (-0.5, 0.25)$ and Right is plotted with $(s, k) = (-0.05, 0.475)$.

"Hermiticity norm" for $\bar{X}_i(t)$ defined by (3.91) using a configuration generated by the simulation. The result is plotted as well. We find that $h(t)$ is small near the peak and hence the $\bar{X}_i(t)$ are close to Hermitian there, which is consistent with our observation that $R^2(t)$ is dominated by the real part in this region. First of all, this is a good news because otherwise we run into a strange situation that the space is not "real".

In Figure 3.9, on the Top panels we plot the same quantities defined by (3.92). In fact, it is not straightforward to calculate the expectation values of the eigenvalues of $T_{ij}(t)$ in the CLM respecting holomorphicity because of their multi-valuedness. Here as (3.95) we simply evaluate $T_{ij}(t)$ using the Hermitian part of $\bar{X}_i(t)$ from one configuration generated by the Complex Langevin simulation, and plot their eigenvalues. From the Top panel, we observe that (3+1)D expanding behavior persists even at $s > -1$. In Figure 3.9, on the Bottom panels we plot the same quantities defined by (3.97). It is also not straightforward to calculate the expectation values of the eigenvalues of $Q(t)$ in the CLM because of its multi-valuedness. Again we simply evaluate $Q(t)$ using the Hermitian part of $\bar{X}_i(t)$ and plot their eigenvalues. From the Bottom panel, we see that the Pauli-matrix structure persists even at $s > -1$.

To estimate the systematic errors due to finite Langevin stepsizes and test the validity of the Complex Langevin method, in one example we plot the history of

$$\frac{1}{N} \mathrm{Tr} \left( \tilde{A}_0 \right)^2 \ , \tag{3.104}$$

in Figure 3.10(Top). According to (3.71), its expectation value must be close to $1-1/N^2$. We also plot the history of

$$\frac{1}{N} \mathrm{Tr} \left( A_i \right)^2 \ , \tag{3.105}$$

in (3.65) in Figure 3.10(Top). (3.71) requires its expectation value to be close to $D-1 = 5$. The error is seen through the derivation from these quantities. The ensemble average is taken, it suggests that the systematic error of these quantities is small. In the simulation, an input of the Langevin stepsize is typically chosen as $\epsilon = 10^{-6}$ and then it is chosen adaptively. The stepsize should be taken small enough to make the systematic error of these quantities small. It depends on the parameter choice. We improved the algorithm further by adopting the 2nd order Runge-Kutta method for discretizing the Complex Langevin method, which makes the systematic error $O(\epsilon^2)$ instead of the present $O(\epsilon)$. The material presented in Chapter 3 do not use it though.

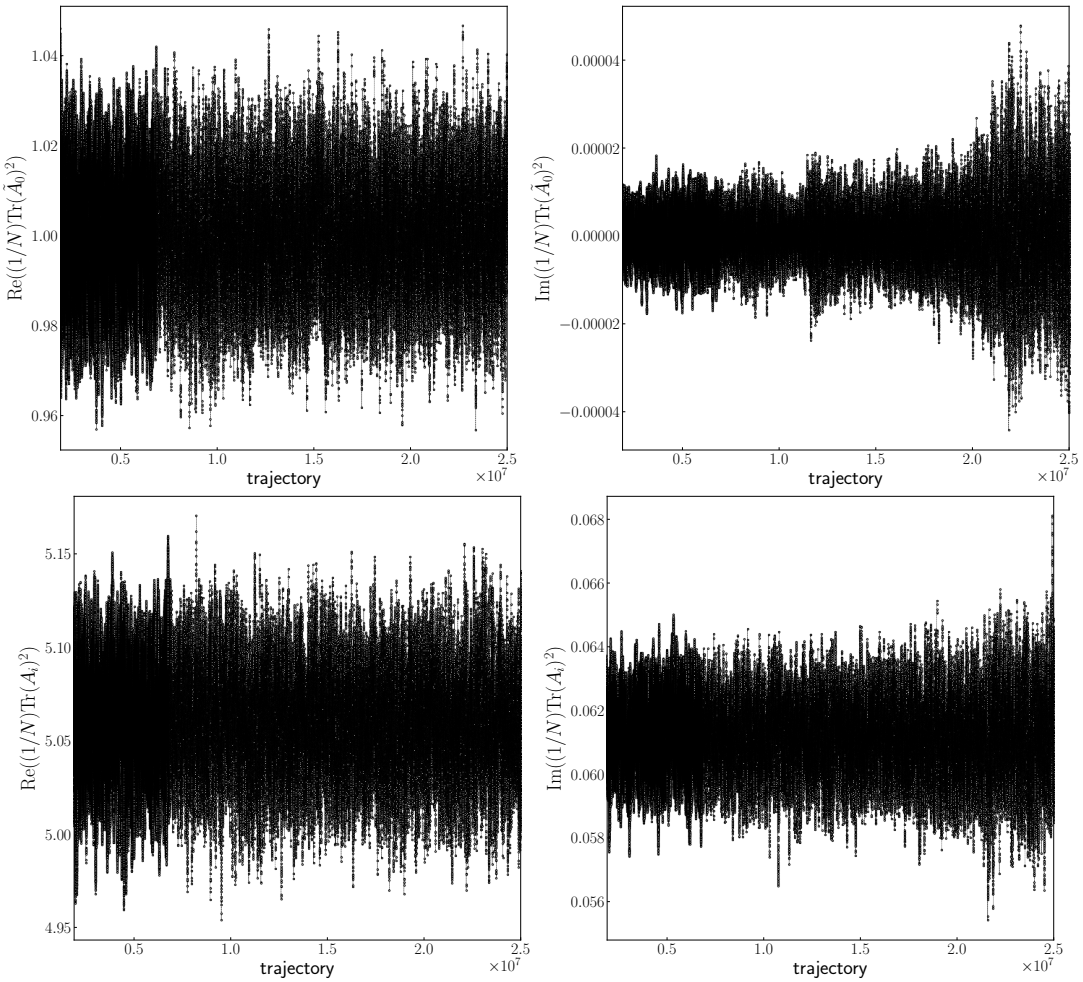


**Figure 3.10:** Results for (5+1)D, $N = 128$, $(s, k) = (-0.5, 0.25)$, $\kappa = 0.02$, $\beta = 8.0$ and the block size $n = 18$ are shown. (Top)The real part and imaginary part of $\frac{1}{N}\,\mathrm{Tr}\left(\tilde{A}_0\right)^2$ are plotted against the number of the Langevin steps. (Bottom)The real part and imaginary part of $\frac{1}{N}\,\mathrm{Tr}\,(A_i)^2$ are plotted against the number of the Langevin steps.

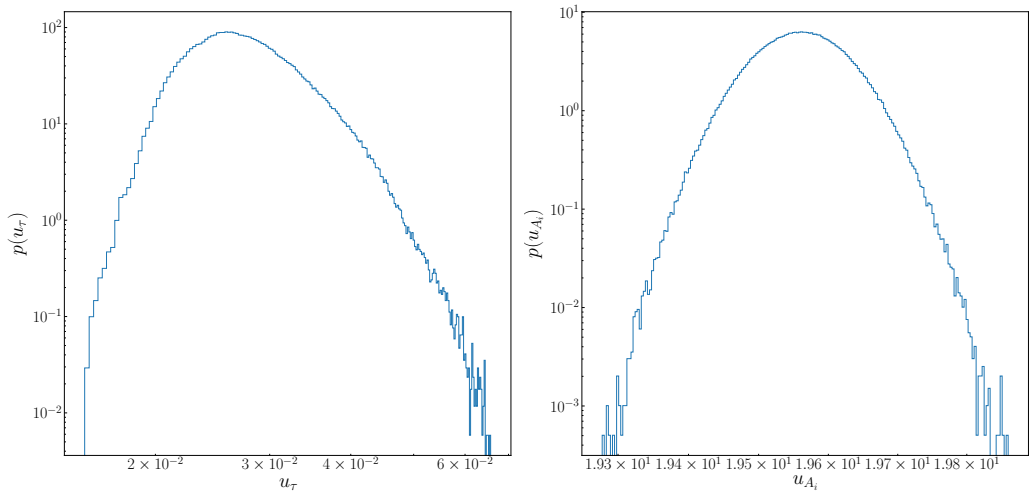


**Figure 3.11:** Results for (5+1)D, $N = 128$, $(s, k) = (-0.5, 0.25)$, $\kappa = 0.02$, $\beta = 8.0$ and the block size $n = 18$ are shown. (Left)The probability distribution of the drift terms in (3.72) is plotted. (Right)The probability distribution of the drift terms in (3.73) is plotted.

In the Complex Langevin simulation, we also must check the criterion as we briefly review the method in Section 3.1.2. In order for this method to hold, the probability distribution $p(u)$ of the magnitude of the drift

$$u_\tau = \sqrt{\frac{1}{N^3} \sum_{i=1}^{N-1} \left| \frac{dS_{\text{eff}}}{d\tau_i} \right|^2} \,, \tag{3.106}$$

$$u_{A_i} = \sqrt{\frac{1}{(D-1)N^3} \sum_{I=1}^{D-1} \sum_{i,j=1}^{N} \left| \frac{dS_{\text{eff}}}{d\,(A_I)_{ji}} \right|^2} \tag{3.107}$$

in the ensemble have to fall off exponentially or faster. The above condition can be violated if the $A_i$ makes long excursions in the anti-Hermitian direction, namely "excursion problem". Another reason for the condition on the drift distribution to be violated is the singular-drift problem. One of the advantages of using $e^{\tau_a)}$ (3.69) is that one can avoid the singular-drift problem that may occur, in principle, from the van der Monde determinant $\Delta(\alpha)$. Note that the associated drift term (3.74) has poles for $\alpha_{a+1} = \alpha_a$, which corresponds to $\tau_a = -\infty$. Therefore, the poles of the drift term occurs only at $\tau_a = -\infty$, which enables us to avoid the singular-drift problem. In one example we plot the probability distribution of these drift terms in Figure 3.11. These plots satisfy the

criteria laid out in [28]. In this way, we also have checked that this criterion is satisfied for all the values of parameters used in this thesis.

## 3.5 Departure from the Pauli-matrix structure

### 3.5.1 Approach $k = 0$ on the line $s = -0.1$

Based on findings from these results, to obtain a regular space-time we have recognized the need to approach the region $(s, k) \sim (0, 0)$, though it is very difficult even for the CLM to study the original model which corresponds to $(s, k) = (0, 0)$ because the Complex Langevin simulation becomes unstable.

For that purpose, we tune the target space deformation parameter $k$ to some values near $k = 0$, which is the target value for the Lorentzian model, keeping the worldsheet deformation parameter $s$ to be on the line $s = -0.1$. Its action is defined by

$$\tilde{S} = -iN\beta e^{is\pi/2} \left\{ -\frac{1}{2} e^{-ik\pi} \operatorname{Tr} (F_{0i})^2 + \frac{1}{4} \operatorname{Tr} (F_{ij})^2 \right\} \tag{3.108}$$

$$= -iN\beta e^{is\pi/2} \left\{ \frac{1}{2} e^{-ik\pi} \operatorname{Tr} [X_0, X_i]^2 - \frac{1}{4} \operatorname{Tr} [X_i, X_j]^2 \right\} . \tag{3.109}$$

We perform the same analysis in (5+1)D, $N = 128$, $\kappa = 0.02$, $\beta = 8.0$ and the block size $n = 18$ with $s = -0.1$ and $k$ decreased from 0.45 to 0.4 and then 0.3. These parameters except for $(s, k)$ are chosen as before.

Figure 3.12 suggests that the time $t$ turns out to be close to real for the configurations. We therefore neglect the small imaginary part of $t$ in making the plots.

In Figure 3.13, we plot the real and imaginary parts of $R^2(t)$ and the Hermiticity norm $h(t)$ defined by (3.91). As we have seen in Figure 3.8, the spatial matrices $\bar{X}_i(t)$ are close to Hermitian near the peak of $R^2(t)$, which suggests that the behavior in this region is semi-classical. This property supports previous speculation [18, 19] that some classical solution which is typically represented by a real configuration, dominates the path integral in the time region near the peak due to the expansion of space. However, in the Bottom panel we find that $R^2(t)$ is getting to be dominated by its imaginary part near the peak. Its configuration generated by the Complex Langevin simulation

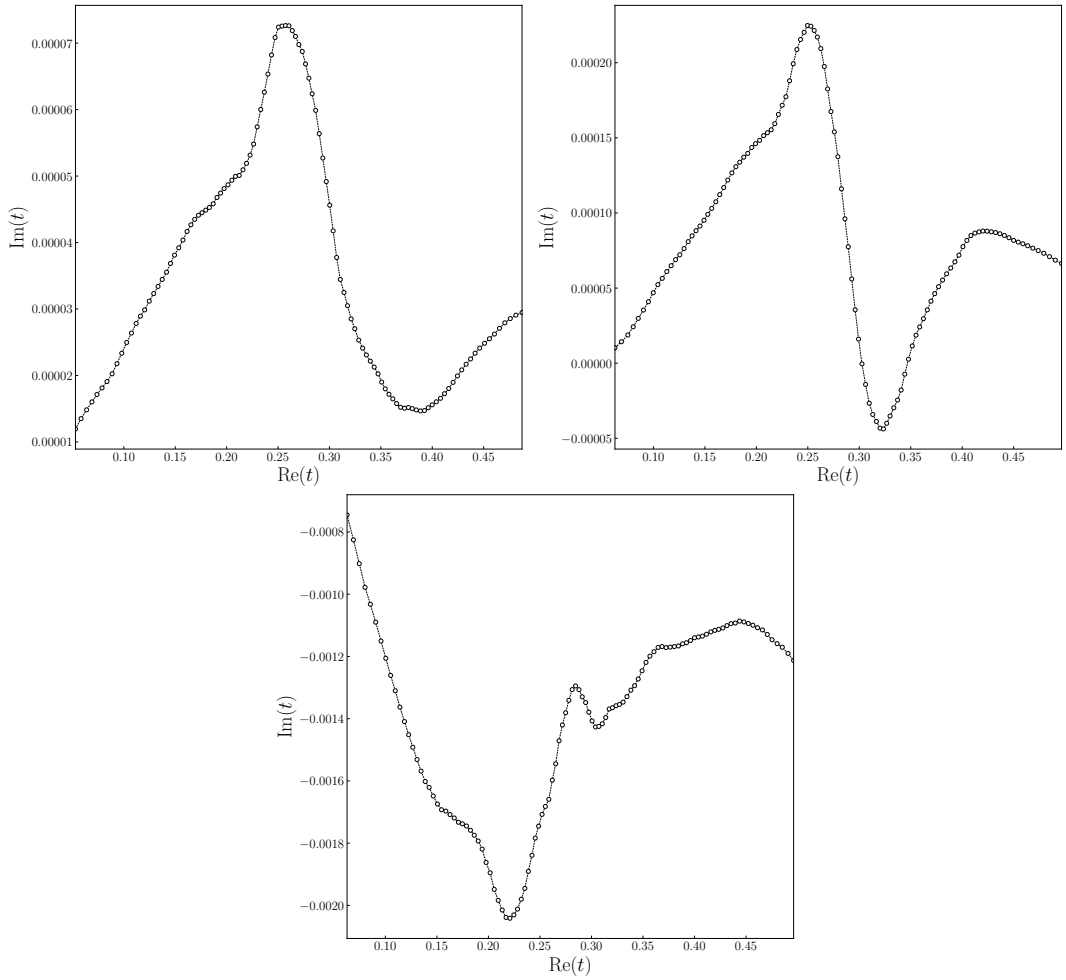


**Figure 3.12:** The time $t$ defined by (3.87) is plotted in the complex plane for the typical configuration with (5+1)D, $N = 128$, $\kappa = 0.02$, $\beta = 8.0$ and the block size $n = 18$, where the $x$-coordinate refers to the real part and the $y$-coordinate refers to the imaginary part of the time $t$. (Top-Left) Results for $(s, k) = (-0.1, 0.45)$ are shown. (Top-Right) Results for $(s, k) = (-0.1, 0.4)$ are shown. (Bottom) Results for $(s, k) = (-0.1, 0.3)$ are shown.

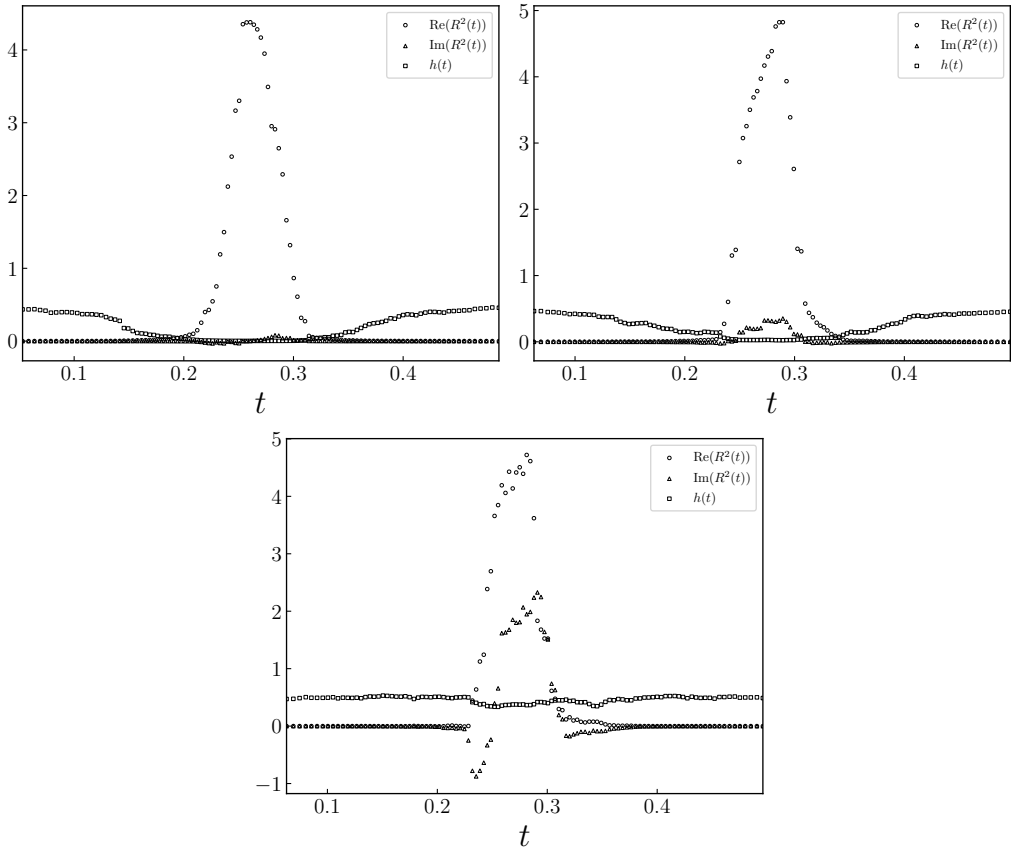


**Figure 3.13:** The real and imaginary parts of $R^2(t)$ are plotted against $t$ for (5+1)D, $N = 128$, $\kappa = 0.02$, $\beta = 8.0$ and the block size $n = 18$. The Hermiticity norm $h(t)$ of the matrix $\bar{X}_i(t)$ is also plotted. (Top-Left) Results for $(s, k) = (-0.1, 0.45)$ are shown. (Top-Right) Results for $(s, k) = (-0.1, 0.4)$ are shown. (Bottom) Results for $(s, k) = (-0.1, 0.3)$ are shown.

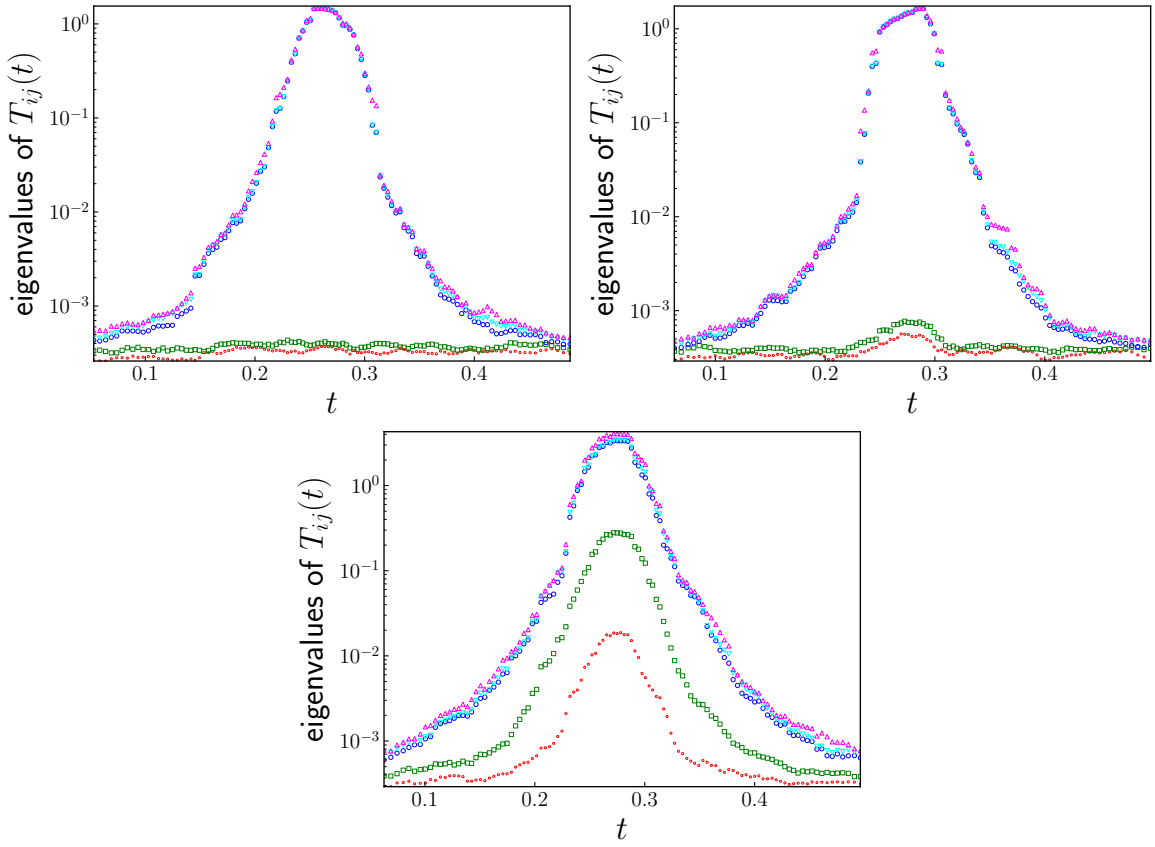


**Figure 3.14:** Results for (5+1)D, $N = 128$, $\kappa = 0.02$, $\beta = 8.0$ and the block size $n = 18$ are shown. The five eigenvalues of the moment of inertia tensor are plotted against $t$ in the log scale. (Top-Left) Results for $(s, k) = (-0.1, 0.45)$ are shown. (Top-Right) Results for $(s, k) = (-0.1, 0.4)$ are shown. (Bottom) Results for $(s, k) = (-0.1, 0.3)$ are shown.

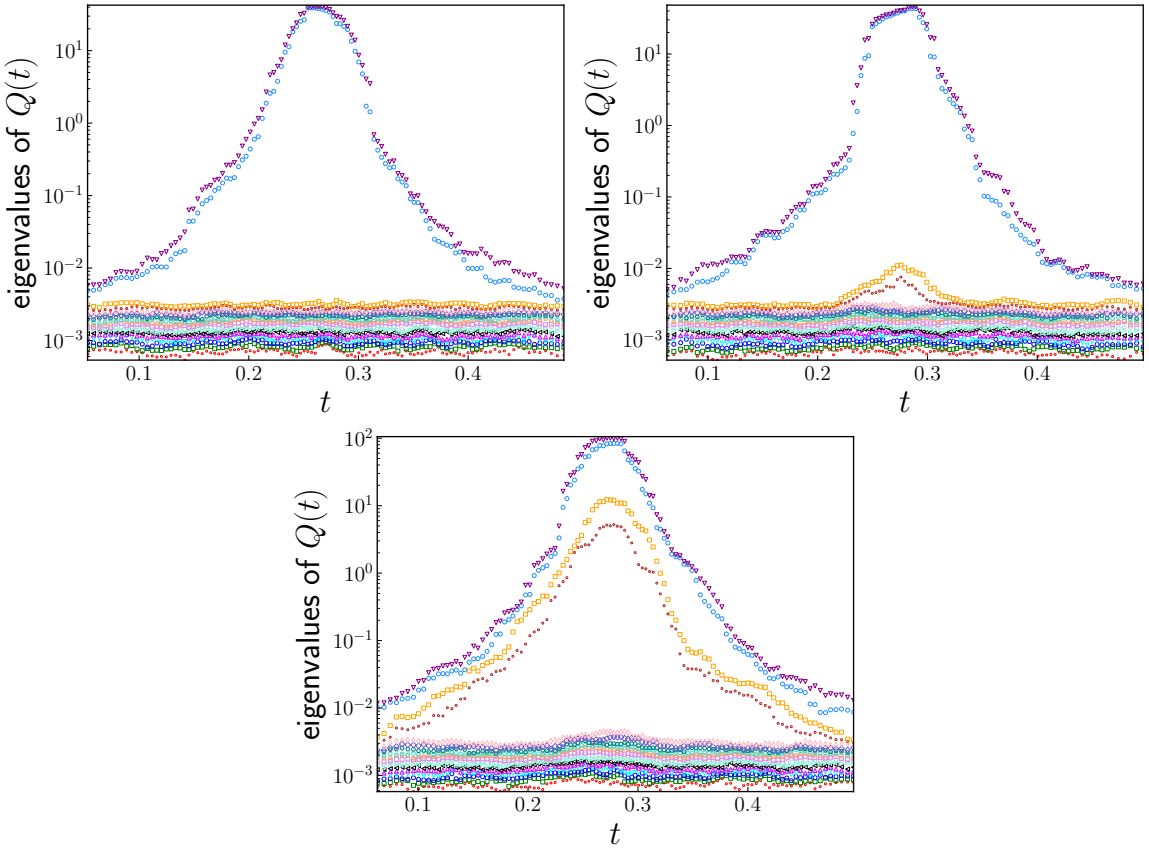


**Figure 3.15:** Results for (5+1)D, $N = 128$, $\kappa = 0.02$, $\beta = 8.0$ and the block size $n = 18$ are shown. The eigenvalues of the matrix $Q(t)$ are plotted against $t$ in the log scale. (Top-Left) Results for $(s, k) = (-0.1, 0.45)$ are shown. (Top-Right) Results for $(s, k) = (-0.1, 0.4)$ are shown. (Bottom) Results for $(s, k) = (-0.1, 0.3)$ are shown.

begins to lose the Hermiticity as well. In fact, when we get closer to the target value for the Lorentzian model which is $(s, k) = (0, 0)$, its Complex Langevin simulation becomes more unstable. To tackle straightforwardly this problems, we should take the large-N limit because we attribute the cause of the instability to the finite matrix size effects.

In Figure 3.14, we plot the same quantities defined by (3.92). In addition, we plot the eigenvalues of $Q(t)$ defined by (3.97) in Figure 3.15. We can observe that the departure from the Pauli-matrix structure is even more pronounced when $k \to 0$. In particular, the result for $(s, k) = (-0.1, 0.3)$ reveals a clear departure from the Pauli-matrix structure. In line with behavior, the 4th, 5th eigenvalues of $T_{ij}$ is lifting up, where the hierarchy of the eigenvalues is formed. We notice the gap between the 3rd largest eigenvalue and the 4th one, and the gap between the 4th and the 5th largest one. As we have mentioned above, its configuration begins to lose the Hermiticity. Therefore must check whether we observe the same behavior or not when we increase the matrix size.

### 3.5.2 Approach $s = 0$ on the line $k = 0$

Lastly, we tune the worldsheet deformation parameter $s$ to some values near $s = 0$, which is the target value for the Lorentzian model, keeping the target space deformation parameter $k$ to be on the line $k = 0$, which is also the target value for the Lorentzian model. In the present case, the action (3.55) is rewritten as

$$\tilde{S} = -N\beta e^{i\frac{\pi}{2}(s+1)} \left\{ -\frac{1}{2} \mathrm{Tr}\,(F_{0i})^2 + \frac{1}{4} \mathrm{Tr}\,(F_{ij})^2 \right\} \tag{3.110}$$

$$= -N\beta e^{i\frac{\pi}{2}(s+1)} \left\{ \frac{1}{2} \mathrm{Tr}\,[X_0, X_i]^2 - \frac{1}{4} \mathrm{Tr}\,[X_i, X_j]^2 \right\} . \tag{3.111}$$

In order to seek the possibility of obtaining a regular space-time, we repeat the same analysis in (5+1)D, $N = 128$, $\kappa = 0.02$, $\beta = 8.0$ and the block size $n = 18$ with $k = 0$ and $s$ decreased from $s = -1$ to $s = -0.9$ and then $s = -0.8$. These parameters except for $(s, k)$ are chosen as before. The case of $(s, k) = (-1, 0)$ we have observed in Section 3.4.1 is added again for the sake of comparison.

In Figure 3.16, we plot the same quantities as in Figure 3.12. It suggests that the time $t$ is close to real for the configurations. We therefore neglect the small imaginary part of $t$ in making the plots. In Figure 3.17, we plot the real and imaginary parts of $R^2(t)$ and the Hermiticity norm $h(t)$ as well. The spatial matrices $\bar{X}_i(t)$ are close to Hermitian

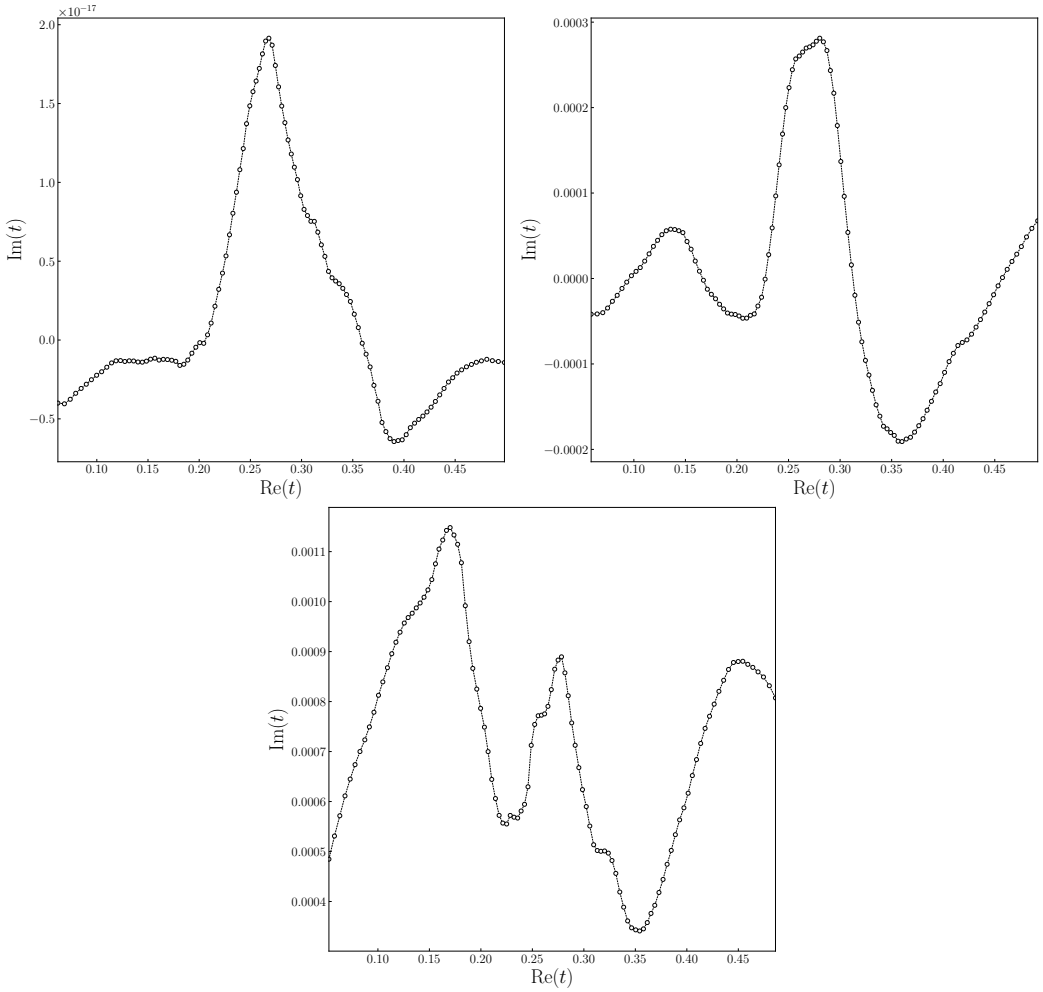


**Figure 3.16:** The time $t$ defined by (3.87) is plotted in the complex plane for the typical configuration with (5+1)D, $N = 128$, $\kappa = 0.02$, $\beta = 8.0$, $n = 18$, where the $x$-coordinate refers to the real part and the $y$-coordinate refers to the imaginary part of the time $t$. (Top-Left) Results for $(s, k) = (-1, 0)$ are shown. (Top-Right) Results for $(s, k) = (-0.9, 0)$ are shown. (Bottom) Results for $(s, k) = (-0.8, 0)$ are shown.

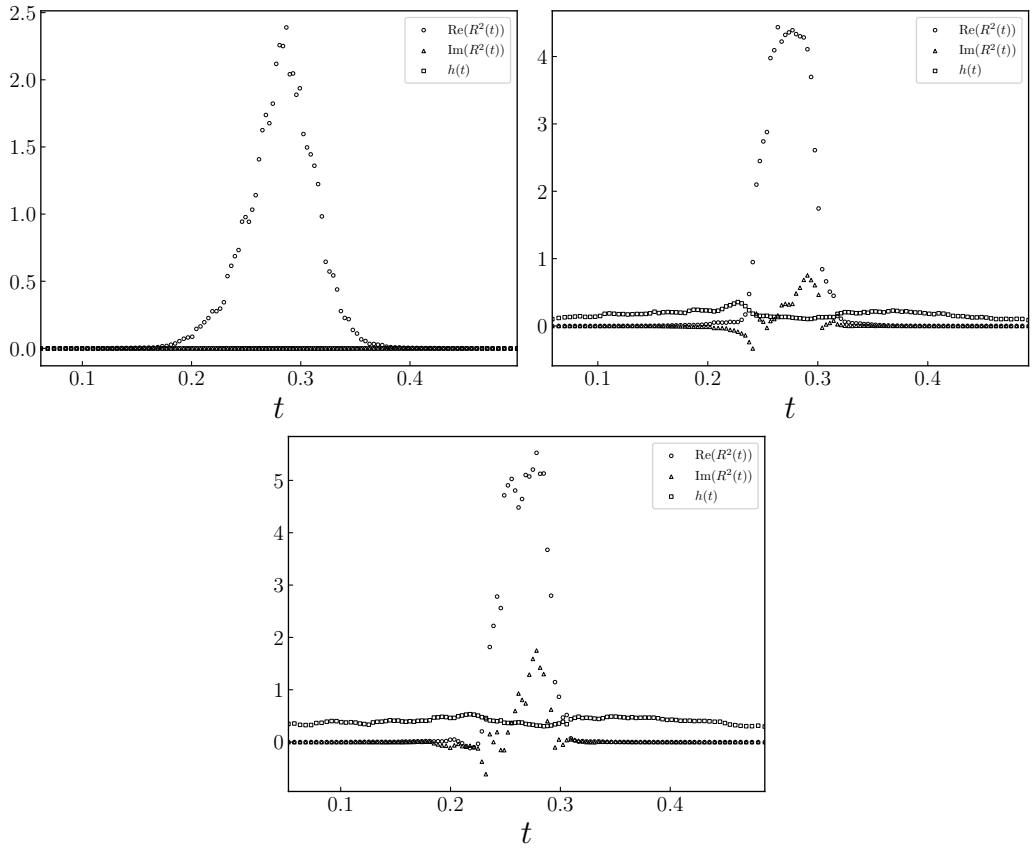


**Figure 3.17:** The real and imaginary parts of $R^2(t)$ are plotted against $t$ for (5+1)D, $N = 128$, $\kappa = 0.02$, $\beta = 8.0$ and the block size $n = 18$. The Hermiticity norm $h(t)$ of the matrix $\bar{X}_i(t)$ is also plotted. (Top-Left) Results for $(s, k) = (-1, 0)$ are shown. (Top-Right) Results for $(s, k) = (-0.9, 0)$ are shown. (Bottom) Results for $(s, k) = (-0.8, 0)$ are shown.

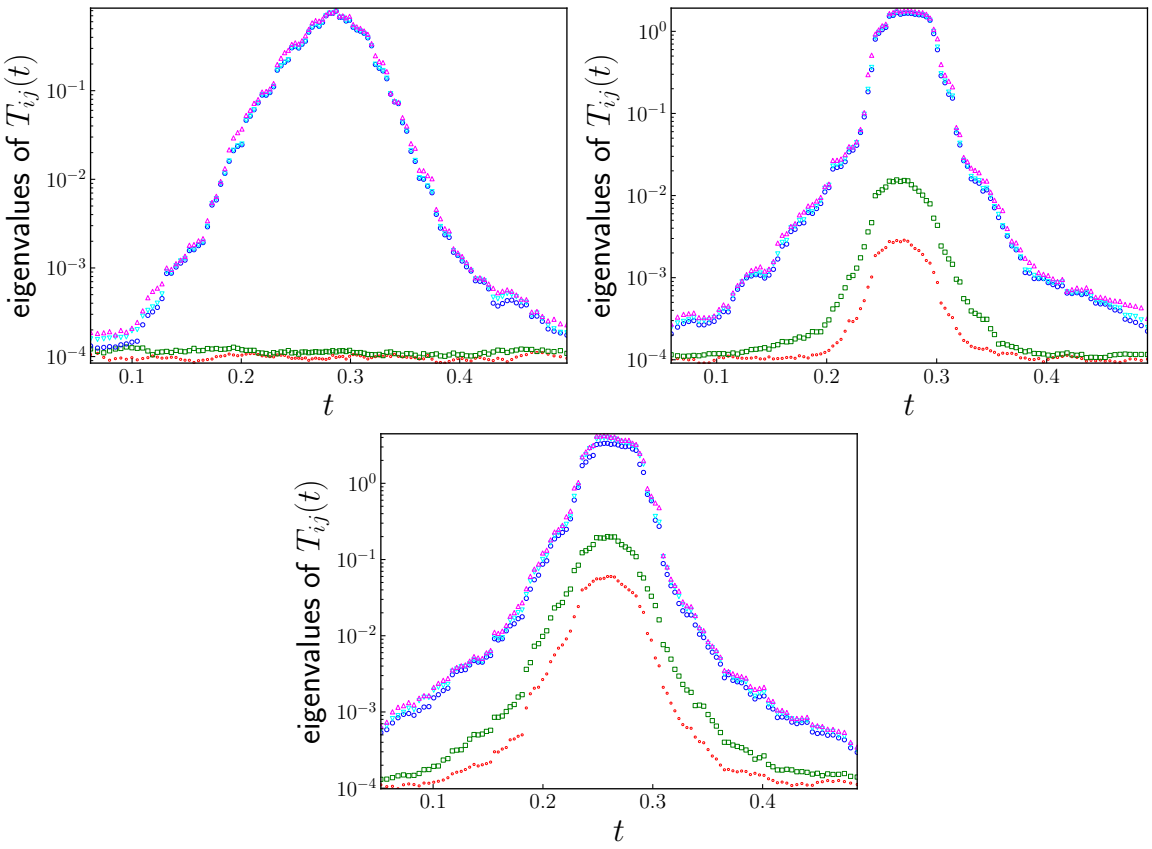


**Figure 3.18:** The five eigenvalues of the moment of inertia tensor are plotted against $t$ in the log scale for (5+1)D, $N = 128$, $\kappa = 0.02$, $\beta = 8.0$ and the block size $n = 18$. (Top-Left) Results for $(s, k) = (-1, 0)$ are shown. (Top-Right) Results for $(s, k) = (-0.9, 0)$ are shown. (Bottom) Results for $(s, k) = (-0.8, 0)$ are shown.

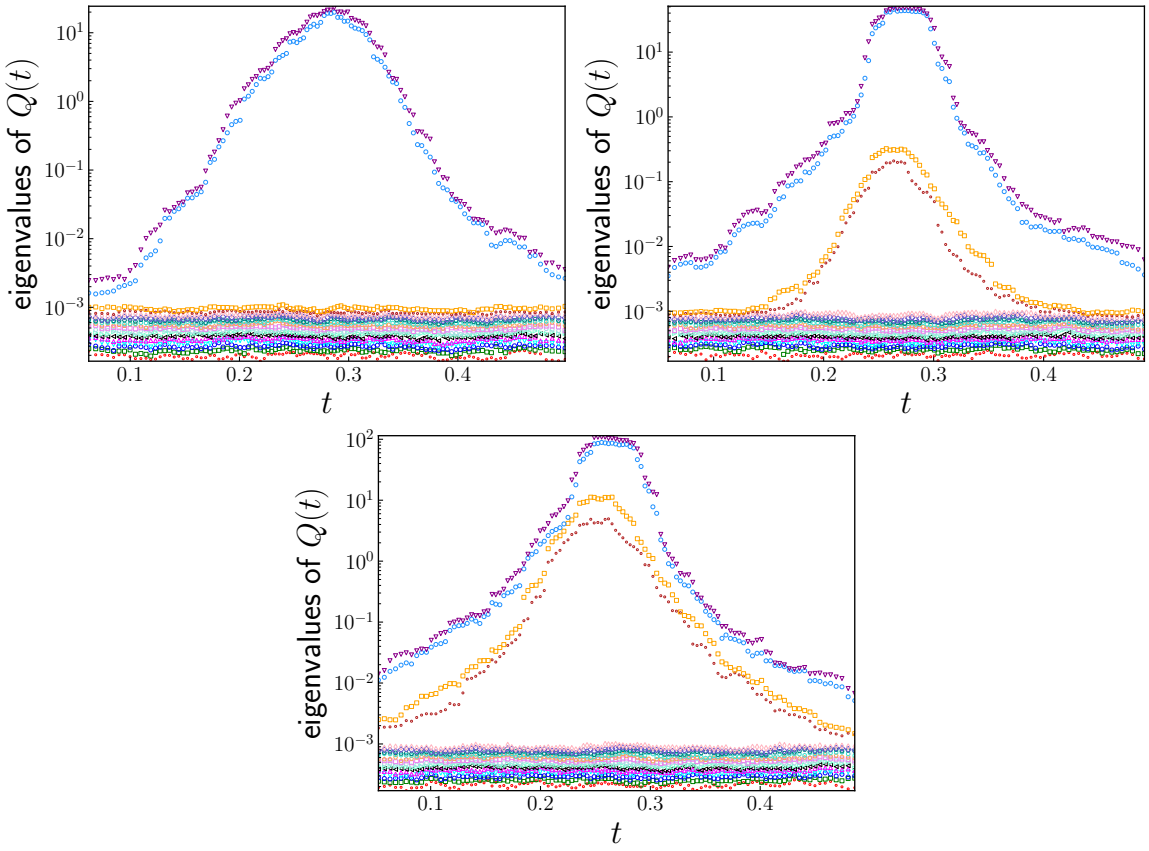


**Figure 3.19:** The eigenvalues of the matrix $Q(t)$ are plotted against $t$ in the log scale for (5+1)D, $N = 128$, $\kappa = 0.02$, $\beta = 8.0$ and the block size $n = 18$. (Top-Left) Results for $(s, k) = (-1, 0)$ are shown. (Top-Right) Results for $(s, k) = (-0.9, 0)$ are shown. (Bottom) Results for $(s, k) = (-0.8, 0)$ are shown.

near the peak of $R^2(t)$. However, in the Bottom panel we find that $R^2(t)$ is getting to be dominated by its imaginary part near the peak. These results are qualitatively the same as those obtained in Section 3.5.1.

In Figure 3.18, we plot the eigenvalues of $T_{ij}$. In addition, we plot the eigenvalues of $Q(t)$. in Figure 3.19. We find that the departure from the Pauli-matrix structure is even more pronounced when $s \to 0$. The result for $(s, k) = (-0.8, 0)$ reveals a clear departure from the Pauli-matrix structure. In line with behavior, the 4th, 5th eigenvalues of $T_{ij}$ are lifting up, where the hierarchy of the eigenvalues is formed. These results are qualitatively the same as those obtained in Section 3.5.1 as well.

## 3.6 Phase diagram in the deformation parameter space $(s, k)$

In our calculations, we start the Complex Langevin simulation with the configuration generated at $(s, k) = (-1, 0)$, where we do not have the sign problem, and proceed to tune the worldsheet deformation parameter $s$ to some values on $(-1 \leq s \leq 1)$, the target-space deformation parameter $k$ to some values on $(0 \leq k \leq 1)$. To summarize, for instance, as we can see in Figure 3.20, one can construct a phase diagram in the deformation parameter space $(s, k)$ through probing the behavior of $Q(t)$, whose eigenvalues represent the radial distribution of the points which describe the 5-dimensional space.

In Figure 3.20, "pauli" correspond to the Pauli-matrix structure (See Figure 3.5 in one example), and "departure from pauli" means the departure from the Pauli-matrix structure (See Figure 3.18(Bottom) in one example). When the Hermiticity of the configurations is completely lost, and the criterion for justifying the CLM is found to be violated, we refer to it as "crash". In fact, the probability distribution of the drift term do not fall off exponentially or faster. In [12], when $s > 0$ the authors observed the deviation from the Pauli-matrix structure. However, according to (3.103), there the Complex Langevin simulation is expected to collapse. With improvement of the treatment of the IR cutoffs, we naturally obtain the solution $s < 0$. The "non band-diagonal structure" corresponds to the situation that when we plot $Q^{sq}_{IJ}$ defined by (3.85), we cannot observe band-diagonal structure. Therefore we cannot follow time evolution. At $(s, k) = (1, 1)$ which is the Euclidean bosonic model, we observe this feature.

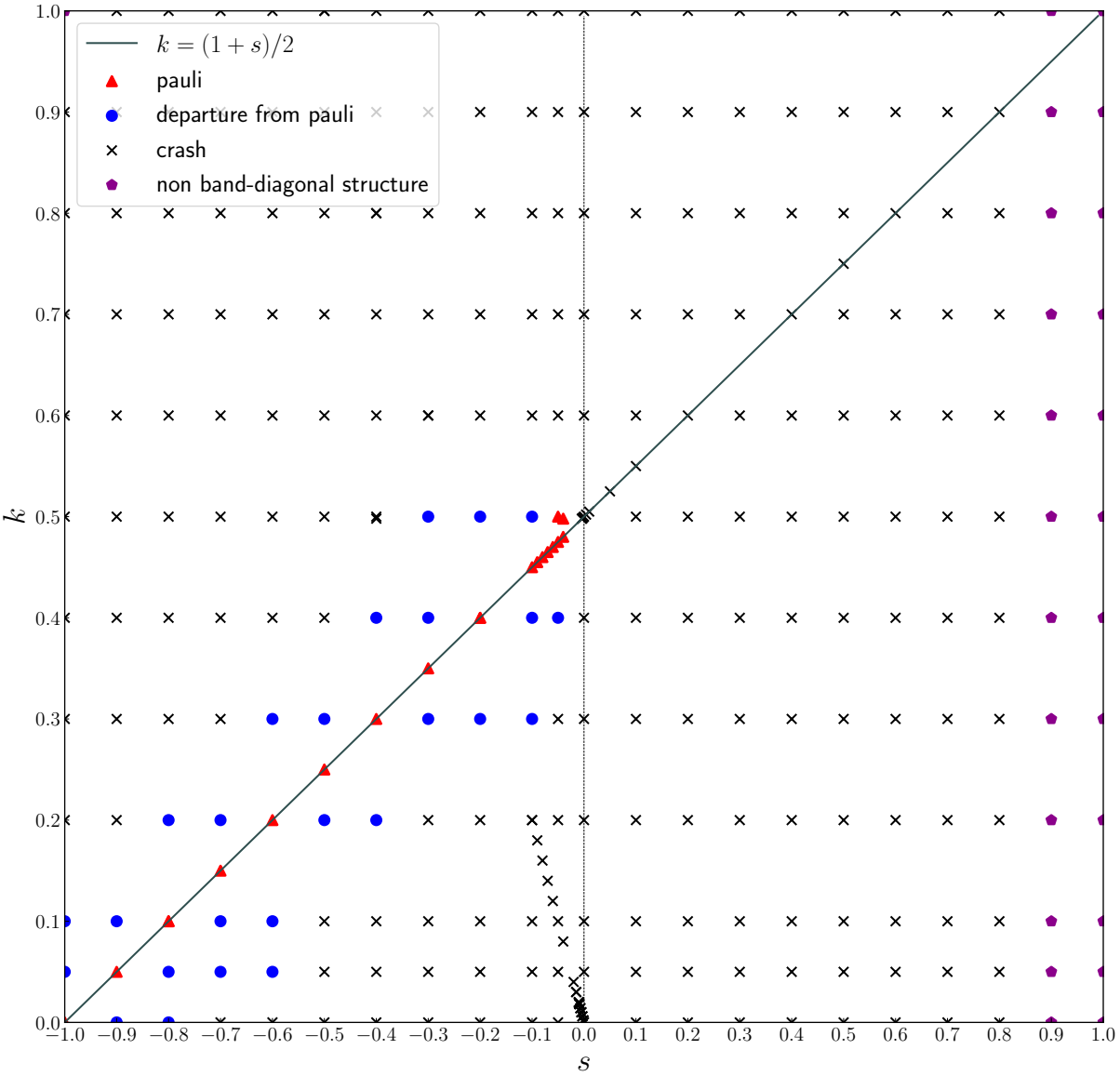


**Figure 3.20:** Phase diagram in the deformation parameter space $(s, k)$ for (5+1)D, $N = 128$, $\kappa = 0.02$, $\beta = 8.0$ and the block size $n = 18$.

Figure 3.20 implies that when we approach our target values $(s, k) = (0, 0)$ which is the Lorentzian model, we can find a clearer departure from the Pauli-matrix structure. However, for the moment, namely $N = 128$ it is not straightforward due to instability of the Complex Langevin method, which comes from finite matrix size effects. Here we have confirmed that $\beta$ does not affect this phase diagram as well. Thus the use of large values of $N$ seems to be crucial in investigating the model near the target values $(s, k) = (0, 0)$.

## 3.7 Summary and discussions

In this chapter we have investigated the space-time structure of the matrix configurations obtained in the Complex Langevin simulations of the Lorentzian type IIB matrix model. Here we have mainly performed the (5+1)D bosonic model in its Lorentzian version to avoid time-consuming.

There the deformation parameters $s$ and $k$ corresponding to the Wick rotations on the worldsheet and in the target space, respectively, have been introduced as previous study had done [12]. In our work, we have improved the treatment of infrared cutoffs on both the spatial and temporal matrices as we discussed in Section 3.3.1. The basic idea is to treat two constraints by rescaling the spatial and temporal matrices instead of constraining them by some strong potential, which mimics the delta function, which we also have implemented in Monte Carlo studies. This new treatment have made the drift term much smaller than the previous work [12], which allows us to use much larger Langevin stepsize. Therefore this improvement have enabled us to investigate a much larger range of deformation parameters, and then approach our target, namely the original model.

In the deformation parameter space $(s, k)$ the original model corresponds to $(s, k) = (0, 0)$, whereas the results Monte Carlo simulations obtained corresponds to the $(s, k) = (-1, 0)$ case. The results for $(s, k) = (-1, 0)$ have reproduced the (3+1)D expanding behavior with the Pauli-matrix structure as previous study [12] had observed. Next we have tuned the parameter $s$ towards the region $s \sim 0$ restricting ourselves to $k = (1+s)/2$ in order to stabilize the Complex Langevin simulation. The results have also showed the Pauli-matrix structure, while the (3+1)D expanding behavior is kept intact as well [3]. Based on findings from these results, we have recognized the need to approach the region $(s, k) \sim (0, 0)$, though it is very difficult even for the CLM to study the original model which corresponds to $(s, k) = (0, 0)$ because the Complex Langevin simulation becomes unstable.

Therefore we have tuned the target space deformation parameter $k$ to some values near $k = 0$, which is the target value for the Lorentzian model, keeping the worldsheet deformation parameter $s$ to be on the line $s = -0.1$. The results indeed showed a clearer departure from the Pauli-matrix structure when nearer $k = 0$. After that, eventually it has been found that we are able to obtain the departure from the Pauli-matrix structure

[3] From the recent study, we observe a departure from the Pauli-matrix structure on the line $k = (1+s)/2$ when we change $\kappa$ and $\beta$ to some values from $\kappa = 0.02$ and $\beta = 8.0$, respectively.

even on the line $k = 0$, tuning the worldsheet deformation parameter $s$ to some values near $s = 0$.

At $(s, k) = (-1, 0)$ the appearance of the Pauli-matrix structure is due to the $\mathrm{Tr}(F_{ij})^2$ term in the action, which tries to make the spatial matrices $X_i$ maximally noncommutative, which plays the important role in the expanding behavior. This feature also affects simulations at $s < 0$. In fact, when $s < 0$ we have naturally obtained the expanding behavior with the non Pauli-matrix structure, though Ref. [12] showed it at $s > 0$. We attribute the different minor details to the improved treatment of IR cutoffs.

On the other hand, when we approach the Euclidean bosonic model, the spatial matrices $X_i$ do not have a band-diagonal structure, which causes a loss of ability to extraction of the real-time evolution. Hence we have reaffirmed that its Lorentzian model is more suitable for studying the real-time dynamics.

In order to obtain a regular space-time with the Lorentzian type IIB matrix model, the phase diagram which summarizes the behavior of the space-time structure relates that we can obtain a smoother space-time structure near our target values $(s, k) = (0, 0)$, which is the Lorentzian model. However, the hermiticity of the configurations becomes completely lost, and the criterion for justifying the CLM is found to be violated. Thus, it is interesting to investigate the model near the target values $(s, k) = (0, 0)$ with large values of $N$ to make the hermiticity norm of the configuration small.

# Chapter 4

# Summary and discussions

The type IIB matrix model was proposed as a non-perturbative formulation of superstring theory in 1997. Monte Carlo studies of its Lorentzian version is arduous hard due to the sign problem caused by the phase factor $e^{iS_{\mathrm{b}}}$ in the partition function. In our Monte Carlo simulations, namely Chapter 2, we have avoided this problem by integrating out the scale factor of the bosonic matrices and using the approximation that we essentially have converted the phase factor $e^{iS_{\mathrm{b}}}$ into the constraint $S_{\mathrm{b}} \simeq 0$. It has been found that the matrix configurations generated by the Monte Carlo simulation are singular in that the submatrices representing the expanding 3D space have only two large eigenvalues associated with the Pauli matrices. We have attributed this problem to the approximation mentioned above used to avoid the sign problem because the function obtained after integrating out the scale factor is complex-valued, and the effect of the phase is not taken into account. It has been noticed that this approximation actually amounts to replacing the phase factor $e^{iS_{\mathrm{b}}}$ by a positive definite weight $e^{cS_{\mathrm{b}}}$ for some $c > 0$. While this new interpretation of the previous simulation enables us to understand better why we obtain the (3+1)D expanding behavior with the Pauli-matrix structure, it also suggests the importance of investigating the model without such an approximation. In other words, whether 3D expanding space with a smooth structure can be obtained if the phase factor $e^{iS_{\mathrm{b}}}$ is used correctly is a very nontrivial issue.

For the purpose of it, we have aimed at applying the Complex Langevin method to the Lorentzian type IIB matrix model in order to overcome the sign problem instead of using the approximation, being motivated by [12]. In this thesis, we have mainly investigated the space-time structure of the (5+1)D bosonic version of the model with the deformation parameters $s$ and $k$ corresponding to the Wick rotations on the worldsheet and in the target space, respectively.

In the deformation parameter space $(s, k)$, we have found the results Monte Carlo simulations obtained corresponds to the $(s, k) = (-1, 0)$ case. Indeed the results for $(s, k) = (-1, 0)$ have reproduced the (3+1)D expanding behavior with the Pauli-matrix structure as the previous study [12] had observed. Note that in the Lorentzian type IIB matrix model, we need some regularization because the phase factor $e^{iS_{\mathrm{b}}}$ in the partition function cannot suppress the contribution from the bosonic matrices with arbitrary large elements. Here we have improved the treatment of infrared cutoffs on both the spatial and temporal matrices. This improvement enables us to investigate a much broader range of deformation parameters $(s, k)$, and then approach our target, namely the original model. When we have approached the original model, which corresponds to $(s, k) = (0, 0)$, our results have shown the transition from the Pauli-matrix structure to the smooth space-time structure, where temporal matrices have a continuous eigenvalues distribution. The space-time structure changes around $(s, k) \sim 0$, where the action becomes complex. Our results imply $e^{iS_{\mathrm{b}}}$ plays an vital role in the properties of the smooth space-time structure, where some quantum effect seems to be necessary.

Some future directions for this work are clear. Inevitably, the most important thing to do is to repeat the same analysis with increased matrix size $N$ because we attribute the instability of the CLM to the finite matrix size effects. We expect that the parameter region much closer to the original model $(s, k) = (0, 0)$ becomes accessible at larger-$N$. The departure from the Pauli-matrix structure observed at $(s, k) \sim 0$ supports this possibility. From examining the findings, with $N = 128$ the Complex Langevin simulation becomes unreliable due to growing non-hermiticity when we approach $(s, k) \sim (0, 0)$ too much. It is interesting to investigate how the space-time expands after taking the large-$N$ limit.

While this behavior may not depend much on the effects of the fermionic matrices, one of the goals of this project is to examine this speculation for the Lorentzian IKKT model without any simplifications, and then it would certainly be desirable to include them eventually. Unfortunately, this is not straightforward because the Complex Langevin method may suffer from the singular-drift problem caused by the near-zero eigenvalues of the Dirac operator. The deformation technique [29] used successfully in studying the Euclidean version [30] is worth trying.

In our work, the extent of space $R^2(t)$ have suggested that hermiticity of spatial matrices emerges as the space expands. More specifically, the spatial matrices have been close to hermitian near the peak of the spatial extent $R^2(t)$. This implies that some classical solution dominates at late times. We expect that a classical solution, which is

typically represented by a real configuration, dominates the path integral in the time region near the peak due to the expansion of space.

On the other hand, there are infinitely many classical solutions [18, 19, 20, 34], which have (3+1)D expanding behavior without the Pauli-matrix structure by solving classical equations of motion. There are also related works [35, 36, 37, 38, 39, 40]. In addition, they tried to find classical solutions, which can accommodate Standard Model particles as excitations around them from the intersecting branes in the extra dimensions [41, 42, 43, 44, 20]. It is interesting to investigate whether a classical smooth space-time picture appears in the large-$N$ limit at a sufficiently late time, which can be answered along the line of this research. In particular, we expect to get results related to the inflation hypothesis. It would be interesting to see whether its expansion is exponential, and it turns into a power law. Here we aim at measuring the correlation functions to see whether the expected power spectrum of the density fluctuations can be reproduced.

In reaching these milestones, we hope that this simulation method, as well as the obtained results discussed in this thesis, is useful in investigating the dynamics of the Lorentzian type IIB matrix model further.

# Bibliography


[1] N. Ishibashi, H. Kawai, Y. Kitazawa and A. Tsuchiya, *A large-N reduced model as superstring*, *Nucl. Phys. B* **498** (1996) 467 [9612115].

[2] M. Fukuma, H. Kawai, Y. Kitazawa and A. Tsuchiya, *String Field Theory from IIB Matrix Model*, *Nucl. Phys. B* **510** (1997) 21 [9705128].

[3] P. Austing and J. F. Wheater, *Convergent Yang-Mills matrix theories*, *J. High Energy Phys.* **5** (2001) [0103159].

[4] J. Nishimura and F. Sugino, *Dynamical generation of four-dimensional space-time in the IIB matrix model*, *J. High Energy Phys.* **6** (2002) 1.

[5] J. Nishimura, T. Okubo and F. Sugino, *Systematic study of the SO(10) symmetry breaking vacua in the matrix model for type IIB superstrings*, *J. High Energy Phys.* **2011** (2011) [1108.1293].

[6] S.-W. Kim, J. Nishimura and A. Tsuchiya, *Expanding (3+1)-dimensional universe from a Lorentzian matrix model for superstring theory in (9+1)-dimensions*, *Phys. Rev. Lett.* **108** (2011) 011601 [1108.1540].

[7] K. N. Anagnostopoulos, T. Azuma and J. Nishimura, *Monte Carlo studies of the spontaneous rotational symmetry breaking in dimensionally reduced super Yang-Mills models*, *J. High Energy Phys.* **2013** (2013) [arXiv:1306.6135v2].

[8] Y. Ito, S. W. S.-W. S.-w. Kim, Y. Koizuka, J. Nishimura and A. Tsuchiya, *A renormalization group method for studying the early universe in the Lorentzian IIB matrix model*, *Prog. Theor. Exp. Phys.* **2014** (2014) 83B01 [1312.5415].

[9] Y. Ito, S.-W. W. Kim, J. Nishimura and A. Tsuchiya, *Monte Carlo studies on the expanding behavior of the early universe in the Lorentzian type IIB matrix model*, *Proc. Sci.* **29-July-20** (2013) 7 [1311.5579].

[10] Y. Ito, J. Nishimura and A. Tsuchiya, *Power-law expansion of the Universe from the bosonic Lorentzian type IIB matrix model*, *J. High Energy Phys.* **2015** (2015) 1 [1506.04795].

[11] T. Aoki, M. Hirasawa, Y. Ito, J. Nishimura and A. Tsuchiya, *On the structure of the emergent 3d expanding space in the Lorentzian type IIB matrix model*, *Prog. Theor. Exp. Phys.* **2019** (2019) [1904.05914].

[12] J. Nishimura and A. Tsuchiya, *Complex Langevin analysis of the space-time structure in the Lorentzian type IIB matrix model*, *J. High Energy Phys.* **2019** (2019) [1904.05919].

[13] M. B. Green and J. H. Schwarz, *Covariant description of superstrings*, *Phys. Lett. B* **136** (1984) 367.

[14] A. Schild, *Classical null strings*, *Phys. Rev. D* **16** (1977) 1722.

[15] W. Krauth, H. Nicolai and M. Staudacher, *Monte Carlo approach to M-theory*, *Phys. Lett. Sect. B Nucl. Elem. Part. High-Energy Phys.* **431** (1998) 31.

[16] Y. Ito, J. Nishimura, A. Tsuchiya and A. Studies, *Universality and the dynamical space-time dimensionality in the Lorentzian type IIB matrix model*, *J. High Energy Phys.* **2017** (1952) 1 [arXiv:1701.07783v1].

[17] T. Azuma, Y. Ito, J. Nishimura and A. Tsuchiya, *A new method for probing the late-time dynamics in the Lorentzian type IIB matrix model*, *Prog. Theor. Exp. Phys.* **2017** (2017) [1705.07812].

[18] S.-W. Kim, J. Nishimura and A. Tsuchiya, *Expanding universe as a classical solution in the Lorentzian matrix model for nonperturbative superstring theory*, *Phys. Rev. D - Part. Fields, Gravit. Cosmol.* **86** (2011) [1110.4803].

[19] S.-w. W. Kim, J. Nishimura and A. Tsuchiya, *Late time behaviors of the expanding universe in the IIB matrix model*, *J. High Energy Phys.* **2012** (2012) [arXiv:1208.0711v1].

[20] K. Hatakeyama, A. Matsumoto, J. Nishimura, A. Tsuchiya and A. Yosprakob, *The emergence of expanding space-time and intersecting D-branes from classical solutions in the Lorentzian type IIB matrix model*, 1911.08132.

[21] G. Parisi, *On complex probabilities*, *Phys. Lett. B* **131** (1983) 393.

[22] J. R. Klauder, *Coherent-state Langevin equations for canonical quantum systems with applications to the quantized Hall effect*, *Phys. Rev. A* **29** (1984) 2036.

[23] G. Aarts, F. A. James, E. Seiler and I. O. Stamatescu, *Adaptive stepsize and instabilities in complex Langevin dynamics*, *Phys. Lett. Sect. B Nucl. Elem. Part. High-Energy Phys.* **687** (2010) 154 [0912.0617].

[24] G. Aarts, E. Seiler and I. O. Stamatescu, *Complex Langevin method: When can it be trusted?*, *Phys. Rev. D - Part. Fields, Gravit. Cosmol.* **81** (2010) [0912.3360].

[25] G. Aarts, F. A. James, E. Seiler and I. O. Stamatescu, *Complex Langevin: Etiology and diagnostics of its main problem*, *Eur. Phys. J. C* **71** (2011) 1 [1101.3270].

[26] J. Nishimura and S. Shimasaki, *New insights into the problem with a singular drift term in the complex Langevin method*, *Phys. Rev. D - Part. Fields, Gravit. Cosmol.* **92** (2015) [1504.08359].

[27] K. Nagata, J. Nishimura and S. Shimasaki, *Justification of the complex Langevin method with the gauge cooling procedure*, *Prog. Theor. Exp. Phys.* **2016** (2016) [1508.02377].

[28] K. Nagata, J. Nishimura and S. Shimasaki, *Argument for justification of the complex Langevin method and the condition for correct convergence*, *Phys. Rev. D* **94** (2016) [1606.07627].

[29] Y. Ito and J. Nishimura, *The complex Langevin analysis of spontaneous symmetry breaking induced by complex fermion determinant*, *J. High Energy Phys.* **2016** (2016) 9 [1609.04501].

[30] K. N. Anagnostopoulos, T. Azuma, Y. Ito, J. Nishimura and S. K. Papadoudis, *Complex Langevin analysis of the spontaneous symmetry breaking in dimensionally reduced super Yang-Mills models*, *J. High Energy Phys.* **2018** (2017) [1712.07562].

[31] G. Parisi and Y.-s. Wu, *Perturbation Theory Without Gauge Fixing*, *Sci.Sin.* **24** (1980) 483.

[32] P. H. Damgaard and H. Hüffel, *Stochastic quantization*, 1987. 10.1016/0370-1573(87)90144-X.

[33] G. Aarts, P. Giudice and E. Seiler, *Localised distributions and criteria for correctness in complex Langevin dynamics*, 1306.3075v1.

[34] F. R. Klinkhamer, *On the emergence of an expanding universe from a Lorentzian matrix model*, 1912.12229.

[35] A. Chaney, L. Lu and A. Stern, *Matrix Model Approach to Cosmology*, Tech. Rep. 6, mar, 2015. 10.1103/PhysRevD.93.064074.

[36] A. Chaney, L. Lu and A. Stern, *Lorentzian Fuzzy Spheres*, 1506.03505.

[37] A. Chaney and A. Stern, *Fuzzy $CP^2$ Space-Times*, 1612.01964.

[38] A. Stern and C. Xu, *Signature change in matrix model solutions*, 1808.07963.

[39] H. C. Steinacker, *Cosmological space-times with resolved Big Bang in Yang-Mills matrix models*, *J. High Energy Phys.* **2018** (2017) [1709.10480].

[40] H. C. Steinacker, *Quantized open FRW cosmology from Yang–Mills matrix models*, *Phys. Lett. Sect. B Nucl. Elem. Part. High-Energy Phys.* **782** (2018) 176 [1710.11495].

[41] A. Chatzistavrakidis, H. Steinacker and G. Zoupanos, *Intersecting branes and a standard model realization in matrix models*, 1107.0265.

[42] J. Nishimura and A. Tsuchiya, *Realizing chiral fermions in the type IIB matrix model at finite N*, *J. High Energy Phys.* **2013** (2013) 1 [1305.5547].

[43] H. C. Steinacker and J. Zahn, *An extended standard model and its Higgs geometry from the matrix model*, 1401.2020.

[44] H. Aoki, J. Nishimura and A. Tsuchiya, *Realizing three generations of the Standard Model fermions in the type IIB matrix model*, *J. High Energy Phys.* **2014** (2014) [1401.7848].

# List of figures

# List of tables